ANALYSIS AND DESIGN OF
ULTRA-WIDEBAND TRANSCEIVER AND ARRAY

ADRIAN TAN ENG CHOON

(B. Eng. (Hons.), NUS)

A THESIS SUBMITTED

FOR THE DEGREE OF DOCTOR OF PHILOSOPHY

NUS GRADUATE SCHOOL FOR INTEGRATIVE

SCIENCES AND ENGINEERING

NATIONAL UNIVERSITY OF SINGAPORE

2007

To My Wife

ACKNOWLEDGMENT

I would like to express my deepest gratitude to my supervisor, Adj. A/P Michael Chia Yan Wah, who has given me the invaluable opportunity to study under his guidance. His realistic attitude towards research and engineering has influenced me considerably. I would also like to sincerely thank each of my committee members, Adj. A/P Chen Zhining and A/P Li Le-Wei for their encouragements in times of difficulty.

I would like to thank Dr. Karumudi Rambabu, who has aided me in many ways, and is a role model to me to pursue a career in academic research. I would like to thank all my friends in the Institute for Infocomm Research: Kevin Chan Khee Meng, Leong Siew Weng, Sim Chan Kuen, Seah Kwang Hwee and Terence See Shie Peng. I would also like to thank the staff in the Radio System Department, Information System Department and NUS Graduate School for their kind support.

I would like to thank my friends who have taught me many lessons in life over the years of my hostel life in secondary school, junior college and university. I would also like to express my gratitude to the Ministry of Education, National University of Singapore, and the Agency for Science and Technology Research, who have provided me the opportunity and financial support for my education in Singapore.

Finally and most importantly, I want to thank my family members: my wife for her love and dedication, my father and mother for making the right decisions, for the endless support and patience in seeing me through my life and education, and my brother whom we have shared many life experiences.

ABSTRACT

Ultra wideband (UWB) is a new emerging short-range device technology with potential benefits for wireless communications, radars, localization, tracking and security applications. UWB systems exchange information by transmitting and receiving short electromagnetic pulses. Therefore, it is very essential to understand the pulse transmission, propagation and reception by UWB terminals. Fundamentally, pulse radiation is different from narrowband signals. Hence, understanding the pulse radiation, effect of the antenna on pulse shape, and signal distortion by band-limited channel are the high priority goals of UWB technology developers. This thesis presents the derivation of the impulse response of an antenna in both transmitting and receiving modes to evaluate the effect of the antenna on UWB pulse shape. This thesis also discusses the development of a UWB signal source that generates sub-nanosecond pulses. Lastly, this thesis presents the system designs for UWB angle-of-arrival (AOA) receivers, UWB monopulse receivers, and medical imaging UWB radars.

In Chapter 2, the impulse response of an antenna in transmitting and receiving modes is derived based on the field distribution of the antenna aperture. To validate the proposed theory, the impulse response for a ridged-horn antenna is derived, and the transmitted and received UWB pulses are studied. The UWB pulses are then measured, and are found to be in good agreement with the proposed theory. This study also discusses the effect of band-limited channel and angular dependence of the received UWB pulses. Chapter 3 applies the impulse response of the antenna into the derivation of the received signals of a UWB time-difference-of-arrival (TDOA) receiver. The UWB TDOA receiver is then analyzed to derive its accuracy in estimating the angle-of-arrival (AOA) of a target in the presence of antenna noise. The derived angle accuracy is verified with root-mean-square errors of AOA measurements using a prototype of the UWB TDOA receiver. From the analysis and measurement, it is found that the angle accuracy of the UWB TDOA receiver depends not only on signal-to-noise ratio but also on angle of incidence.

Chapter 4 details the derivation of the impulse response of a UWB monopulse receiver. The monopulse receiver uses a square-feed array of ridged-horn antennas to capture the incident signal. A bank of cross-correlation receivers is proposed to receive the monopulse signals to enable angle discrimination of the UWB monopulse receiver. The output voltages from the cross-correlators are used to find the target angle with an amplitude-comparison monopulse processor. The derivations are verified with measurements of monopulse signals and the output voltages of the cross-correlators. The angle accuracy of the UWB monopulse receiver in the presence of antenna noise is also examined.

Chapter 5 presents the design, fabrication and measurement of a UWB pulse-forming network (PFN) that is amenable to integrated circuits. The designed PFN is suitable for applications in high data rate UWB communication systems and short-range UWB radars. To generate a UWB pulse, a frequency-selective, negative-feedback circuit to perform time derivative on an input step signal is used. Measured output pulses of the proposed PFN show consistency in pulse widths (170 ps to 180 ps) for a large variation of input signal rise-times (45 ps to 300 ps), as intended by the design. The PFN consumes 3.3 V, 20 mA during operation.

In Chapter 6, a method for imaging the human body using UWB radars is proposed. The method uses the scattered signals from the human body to calculate its impulse response. Human phantoms are fabricated. Impulse responses of the human phantoms are measured with a prototype of UWB radar. The measured impulse responses of the human phantoms are verified by comparing them with derived reflection coefficient of an infinitely large two-layered medium. It is found that the UWB radar can achieve limited imaging capability of the internal organs in the human body.

CONTENTS

LIST OF FIGURES

Figure:

LIST OF TABLES

Table:

LIST OF SYMBOLS

A_{ch}	Propagation channel's frequency independent attenuation
A_e	Amplitude of the incident signal
A_s	Amplitude of the source signal
d_1	Antenna dimension at the x' direction
d_2	Antenna dimension at the y' direction
d_e	Delay of the source signal
d_s	Delay of the incident signal
d_{mi}	Thickness of medium i
$D_A(\theta, \varphi)$	Azimuth difference channel cross-correlated voltage value
$D_E(\theta, \varphi)$	Elevation difference channel cross-correlated voltage value
$\hat{D}$	Estimated azimuth difference channel cross-correlated value
c	Speed of light in vacuum
$e(t)$, $E(\omega)$	Incident signal to the receiving antenna
E_b	Energy of the received signal
$E_d(\theta)$	Energy of the received signal in the azimuth difference channel
$E_s(\theta)$	Energy of the received signal in the sum channel
$f_c(t)$, $F_c(\omega)$	Transfer function of signal propagation at path 'C'
$f_e(t)$, $F_e(\omega)$	Transfer function of signal propagation at path 'E'
$f_\sigma(t)$, $F_\sigma(\omega)$	Transfer function of the scattering from the target
$f^w{}_\sigma(t)$, $F^w{}_\sigma(\omega)$	Windowed transfer function of the scattering from the target
$f^{th}{}_\sigma(t)$, $F^{th}{}_\sigma(\omega)$	Theoretical transfer function of the scattering from the target

$f_{ad}\,(t, \theta, \varphi)$, $F_{ad}\,(\omega, \theta, \varphi)$	Impulse response of the azimuth difference array in receiving mode
$f_{ed}\,(t, \theta, \varphi)$, $F_{ed}\,(\omega, \theta, \varphi)$	Impulse response of the elevation difference array in receiving mode
$f_s\,(t, \theta, \varphi)$, $F_s\,(\omega, \theta, \varphi)$	Impulse response of the Sum array in receiving mode
$f_t\,(t, \theta, \varphi)$, $F_t\,(\omega, \theta, \varphi)$	Impulse response of the antenna in transmitting mode
$f_r\,(t, \theta, \varphi)$, $F_r\,(\omega, \theta, \varphi)$	Impulse response of the antenna in receiving mode
$g\,(x', y')$	Field distribution of antenna aperture
$g_1\,(x')$	Field distribution of antenna aperture in the x' axis
$g_2\,(y')$	Field distribution of antenna aperture in the y' axis
$g_{ad}\,(x', y')$	Field distribution of azimuth difference array
$g_{ed}\,(x', y')$	Field distribution of elevation difference array
$g_s\,(x', y')$	Field distribution of sum array
$h_t\,(t)$, $H_t\,(\omega)$	Transfer function of the transmitting antenna
$h_r\,(t)$, $H_r\,(\omega)$	Transfer function of the receiving antenna
$h_{ch}\,(t)$, $H_{ch}\,(\omega)$	Transfer function of the propagation channel
k_0	Propagation constant of free space
k_i	Propagation constant of medium i
k_B	Boltzmann's constant
m	Positive integer value, models the antenna field in the x' axis
n	Positive integer value, models the antenna field in the y' axis
$n_i\,(t)$	Thermal noise signal of the i-th receiver
N_i	Noise power per unit bandwidth of the i-th receiver
$p_{da}\,(t)$	Azimuth difference channel reference cross-correlation signal
$p_{de}\,(t)$	Elevation difference channel reference cross-correlation signal
$p_s\,(t)$	Sum channel reference cross-correlation signal
$r\,(t)$, $R\,(\omega)$	Output signal of the receiving antenna
$r_{ad}\,(t)$, $R_{ad}\,(\omega)$	Azimuth difference signal of the Monopulse receiver

$r_{ed}\ (t)$, $R_{ed}\ (\omega)$	Elevation difference signal of the Monopulse receiver
$r_s\ (t)$, $R_s\ (\omega)$	Sum signal of the Monopulse receiver
$r_n\ (t)$	Noise corrupted output signal of the receiving antenna
$r_{sn}\ (t)$	Noise corrupted output signal of the sum channel
$r_{dan}\ (t)$	Noise corrupted output signal of the azimuth difference channel
$r_0\ (t)$, $R_0\ (\omega)$	Reference correlating signal of the TDOA receiver
$\hat{R}$	Estimated Monopulse ratio
$s\ (t)$, $S\ (\omega)$	Input signal to the transmitting antenna
s_1	Separation between antennas at the x' direction
s_2	Separation between antennas at the y' direction
$S\ (\theta, \varphi)$	Sum channel cross-correlated voltage value
$\hat{S}$	Estimated sum channel cross-correlated value
$v\ (\tau, \theta)$	Signal function of the posterior probability of the estimated TOA
v_d	Signal function of the azimuth difference channel value
v_{s}	Signal function of the sum channel value
$w\ (\tau, \theta)$	Noise function of the posterior probability of the estimated TOA
w_d	Noise function of the azimuth difference channel value
w_{s}	Noise function of the sum channel value
$W_{\mathrm{g}}\ (\omega)$	Frequency windowing function
τ_e	Pulse width of the incident signal
τ_s	Pulse width of the source signal
T	Pulse repetition interval
T_{ant}	Antenna temperature
α	Length of the ridged-horn antenna
β	Height of the ridged-horn antenna

$\beta_s\,(\theta)$	Signal's second moment
ε_0	Free space permittivity constant
$\hat{\theta}$	Estimated angle of arrival of receiver
η_0	Intrinsic impedance of free space
η_i	Intrinsic impedance of medium i
μ_0	Free space permeability constant
ω_{ch}	Propagation channel's frequency dependent attenuation
τ_0	True time of arrival of received signal
$\hat{\tau}_0$	Estimated time of arrival of received signal
τ	Sweeping delay of the reference signal, to estimate τ_0
$\sigma_{\tau i}\,(\theta)$	Standard deviation of the estimated TOA at the i-th channel

LIST OF CONTRIBUTIONS

[1] A. E.-C. Tan, and M. Y.-W. Chia, "UWB Radar Transceiver and Measurement for Medical Imaging", *IEEE BioCAS*, Singapore, Dec. 2004.

[2] A. E.-C. Tan, and M. Y.-W. Chia, "Method of Generating UWB Pulses", *World Intellectual Property Organization*, Pub. No. WO 2005/067160 A1, Jul. 2005.

[3] A. E.-C. Tan and M. Y.-W. Chia, "Measuring Human Body Impulse Response Using UWB Radar", *IEE Electron. Lett.*, vol. 41, no. 21, Oct. 2005, pp. 1193-1194.

[4] A. E.-C. Tan and M. Y.-W. Chia, "Measuring Human Body's Impulse Response", *UK-Singapore Bioelectronics Workshop*, Jan 2006.

[5] A. E.-C. Tan, M. Y.-W. Chia and S.-W. Leong, "Sub-nanosecond Pulse-Forming Network on SiGe BiCMOS for UWB Communications", *IEEE Trans. MTT*, vol. 54, no. 3, Mar. 2006, pp. 1019-1024.

[6] K. Rambabu, A. E.-C. Tan, K. K.-M. Chan and M. Y.-W. Chia and S.-W. Leong, "Study of Antenna Effect on UWB Pulse Shape in Transmission and Reception", *ISAP 2006*, Singapore, Nov. 2006.

[7] A. E.-C. Tan, M. Y.-W. Chia and K. Rambabu, "Design of Ultra-Wideband Monopulse Receiver", *IEEE Trans. MTT*, vol. 54, no. 11, Nov. 2006, pp. 3821-3827.

[8] K. Rambabu, A. E.-C. Tan, K. K.-M. Chan and M. Y.-W. Chia, "Estimation of Antenna Effect on UWB Pulse Shape in Transmission and Reception", submitted to *IEEE Trans. MTT*, Nov. 2006.

[9] A. E.-C. Tan, M. Y.-W. Chia and K. Rambabu, "Effect of Antenna Noise on Angle Estimation in Ultra-Wideband Receivers", submitted to *IEEE Trans. AP*, Dec. 2006.

[10] A. E.-C. Tan, M. Y.-W. Chia and K. Rambabu, "Angle Accuracy of Antenna Noise Corrupted Ultra-Wideband Monopulse Receiver", *ICUWB 2007*, Sep. 2007.

CHAPTER 1

INTRODUCTION

1.1 Research Background

This thesis presents the analysis and design of ultra-wideband (UWB) radio transceivers and arrays. UWB radio transceivers can be contrasted from their narrowband radio counterparts by the signals that they transmit and receive, which tend to be large in fractional bandwidth [1]. UWB has been defined by the Federal Communications Commission (FCC) as radio systems that transmit signal with fractional bandwidth larger than 0.2, or a bandwidth that is at least 500 MHz [2]. For UWB radio systems, the fractional bandwidth is defined as 2 $(f_H - f_L) / (f_H + f_L)$, where f_H is the upper −10 dB edge frequency and f_L is the lower −10 dB edge frequency. According to the current FCC's frequency allocations [2], there are, in total, three frequency bands that are allowed for UWB operations, with each band catering for different types of applications. The allotted frequency bands are: below 960 MHz, 3.1 − 10.6 GHz and 22 − 29 GHz. For all three bands, the effective isotropic radiated power (EIRP) is limited to −41.3 dBm / MHz.

The 3.1 − 10.6 GHz band UWB radio finds many applications in short range, high data rate communication systems [3], [4] and in radar systems [1], [5]. Currently, there are two competing methods to provide UWB radio communications in the 3.1 – 10.6 GHz band. They can be classified as the impulse and non-impulse UWB radio systems. The impulse and non-impulse UWB radio systems came about in the IEEE 802.15 Task Group 3a, where two competing technical proposals – the multi-band orthogonal frequency division multiplexing (MB-OFDM) and direct-sequence ultra-wideband (DS-UWB), fail to reconcile their differences. The MB-OFDM is commonly referred to the non-impulse UWB, and the DS-UWB is commonly known as the impulse UWB radio systems.

The MB-OFDM system (non-impulse UWB) is a combination of frequency hopping and OFDM technologies [6] [7]. A block of information forms one OFDM symbol. The OFDM symbol bandwidth is 500 MHz, and consists of a frequency multiplex of 128 sub-carriers. The OFDM symbol interval is 312.5 ns, after which, the subsequent symbol will be transmitted over different sub-bands determined by pre-defined frequency hopping patterns.

The DS-UWB system (impulse UWB) is based on direct-sequence spread spectrum technology [8] [9]. Each data symbol is spread by a specific spreading code to form a transmit sequence of pulses. Each of the pulses has 200-300 ps pulse-width, with a subsequent quiet period that depends on the pulse repetition frequency (PRF) of the radio system.

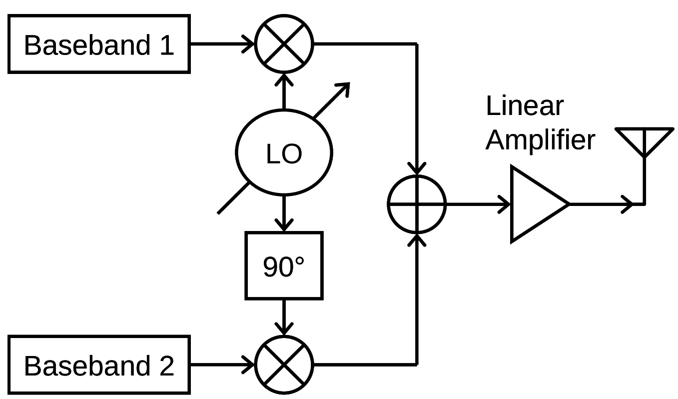

Figure 1.1: Transmitter schematics of a non-impulse based UWB radio system.

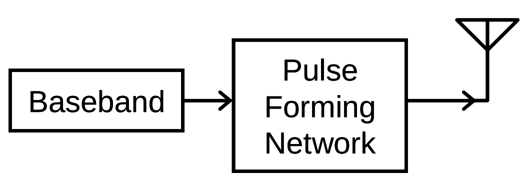

Figure 1.2: Transmitter schematics of an impulse based UWB radio system.

To the RF transceiver, there are two critical differences between the impulse and non-impulse based UWB radio systems – different signal generation method and vastly different signal time-widths. The non-impulse based UWB radio system generates the UWB signal in a similar manner as narrowband systems, except with a few differences, as shown in Fig. 1.1. On the other hand, the impulse based UWB radio system generates the UWB signal by either first generating short, sub-nanosecond pulses with non-linear circuits, and then modulates them, as shown in Fig. 1.2, or combines the two steps into an integrated UWB signal generator.

It can be seen from Figs 1.1 and 1.2 that the transmitter architecture for impulse based UWB radio system is much simpler than that of the non-impulse based UWB system. The time-widths of the impulse based UWB system is 200-300 ps, compared to a much longer 312.5 ns pulse width of the non-impulse based UWB system. Hence, the design requirement of antenna, which is of particular interest in this research, is different. Impulse based UWB system radiates and receives signals that are electrically short compared to size of the antennas, whereas non-impulse based UWB systems do not.

The main advantage of UWB in radio communications over its narrowband counterparts can be understood from Shannon's link capacity formula, where it is shown that with a large bandwidth, only a very small radiation power is needed to achieve high data rate in short ranges [1]. Furthermore, UWB radio systems suffer much less from channel fading as compared to narrowband radio systems, because short pulses propagating over different paths can be better distinguished by the UWB radio receiver. On the other hand, the UWB radar has many advantages over conventional narrowband radars. The UWB radar has better range resolution because the short pulse enables target differentiation at smaller dimensions in the range axis [1]. Besides that, UWB radar has more detectable materials penetration because there is a large aggregate of frequency components in the radiated pulse. Even if a material attenuates some frequency components of the radiated pulse, other frequency components may not be attenuated as severely. Furthermore, it is easier to recover information of the target from reflected signal because the signal is large in bandwidth, and thus, provides more information on the target. Lastly, if the radar signal is coded with pseudo-random bit sequence (PRBS), the transmitted signal appears noise-like to the target, thus it has a low likelihood of being detected.

This thesis only considers the analysis and design of UWB radio transceivers in the 3.1 − 10.6 GHz band. The 3.1 − 10.6 GHz band is chosen because, firstly, it has a large fractional bandwidth of 1.09, and secondly, it has a centre frequency of 6.85 GHz. Having a large fractional bandwidth allows the UWB radio transceiver to transmit and receive short pulses that can be easily modeled as second or third derivative Gaussian functions. Having a centre frequency of 6.85 GHz allows the UWB radio transceiver to transmit and receive short pulses that have sub-nanosecond pulse widths. Both properties of the transmitted pulse (simple and short) are important for the applications considered in this thesis – human body surveillance and tracking (Chapters 3 and 4); high pulse rate radio communication and radar systems (Chapter 5); and human body imaging for medical purposes (Chapter 6).

To perform surveillance and tracking using the UWB radio transceiver, short pulse widths are needed to provide a good location tracking accuracy. Two types of transceiver architectures will be described in this thesis. In Chapter 3, the time-difference-of-arrival (TDOA) method of target tracking will be described, while in Chapter 4, the monopulse method of target tracking will be described. The excellent range accuracy of the 3.1 – 10.6 GHz UWB radio system can be best illustrated with the following example: Let a transmitted UWB signal with 0.2 ns pulse width and a 3 dB signal-to-noise ratio (SNR) be captured by a receiver. The said receiver can achieve a range accuracy (root-mean-square error) of less than one centimeter [10]. The accuracy calculation in the above example will be further elaborated in Chapter 3. To achieve an accurate imaging capability of the human body, as shown in Chapter 6, the UWB radio transceiver will require a higher signal-to-noise ratio (SNR), which can be achieved by signal averaging.

The thesis addresses both general and specific problems in the design of UWB radio systems. Chapters 2, 3 and 4 of the thesis address general problems like the modeling of signal distortion by the UWB antenna, the application of a UWB antenna array to estimate target locations and the estimation of the accuracy of such UWB radio systems. Chapters 5 and 6 address problems that are relevant to the understanding of specific UWB radio systems, like the problem of high data rate pulse generation and the application of UWB radar in medical imaging.

Despite the many advantages of UWB over conventional narrowband radio transceivers, many aspects of the UWB are still insufficiently modeled. For instance, it is observed that the transmission and reception of UWB signals suffer from varying degrees of pulse distortions at different angles [11]−[13]. Conventional antenna parameters like antenna gain and radiation pattern [14], while successful in explaining the transmission and reception of narrowband signals, fail to account for the angle dependent pulse distortions in UWB signals. Because of the differences in signal transmission and reception compared to narrowband, the UWB antenna has been modeled as an impulse response in many existing literature [12], [15]−[19]. Schantz [20] attributed the UWB antenna's dispersion to the current radiation at different parts of the antenna. A more severe form of dispersion in UWB antenna is evident in frequency independent antennas. The dispersion in these antennas are caused by their reliance on different radiating, narrowband elements, located at different locations, to achieve the broadband. Because of the electrically short UWB signal compared with the antenna dimension, whenever the antenna radiates the signal at different antenna locations, signal dispersion occurs, and needed to be accounted for. In the thesis, signal dispersion for directional antennas at different angles will be modelled and accounted for. Furthermore, it has been shown [21]−[23] that the transmitting transient response of an antenna is proportional to the time derivative of the receiving transient response of the same antenna. To better model the transmission and reception of UWB signals by the antenna, an impulse response model that relates the signal distortions by the antenna with the antenna's aperture field distribution is described in Chapter 2 of the thesis.

One of the ways to perform surveillance and tracking using UWB radio transceivers is with the time-difference-of-arrival (TDOA) method [24]−[28]. The TDOA method, as described in Chapter 3 of this thesis, finds the location of the target by estimating the range and angle-of-arrival of the target. Using the TDOA method for UWB radio systems is ideal, because the TDOA method can leverage on the inherently short electrical lengths of UWB signals in free-space (*e.g.* 6 to 15 cm for a UWB pulse of typical pulse width 0.2 to 0.5 ns) to locate the radar target or transponder with better accuracy. However, in the existing literature, analyses of UWB TDOA receivers fail to consider the antenna impulse response effect on the receiver, which may compromise accuracy of the estimated target location. In Chapter 3, the antenna impulse response is incorporated in the analysis of the UWB TDOA receiver in estimating the angle-of-arrival accuracy. With the knowledge of the UWB TDOA receiver's accuracy, location accuracy of a target can now be a design parameter of the UWB radio system.

In Chapter 4, we present another UWB transceiver array design that performs surveillance and tracking. The proposed transceiver is the UWB monopulse radar. Unlike TDOA, monopulse is a radar technique to locate the angular direction of a target by receiving the incident signal simultaneously with two or more antennas [29]. It is used in existing pulsed and continuous-wave radars to track targets, providing guidance information and steering commands for missiles in missile-range instrumentations [30], [31]. Monopulse technique has been proposed for ultra-wideband (UWB) radars [32] by Harmuth *et. al.* The monopulse sum and difference patterns have been derived for the case of equally spaced dipoles receiving short, rectangular pulses [32]−[35], and for the case of equally-spaced point antennas receiving Generalised Gaussian Pulses [36]. Furthermore, two methods for finding the target direction were proposed in [35] – the slope processor and the linear-regression processor. Both processors' performances were studied in [35] when the sum and difference signals are corrupted by additive thermal noise.

In UWB radio systems, the transmitter needs to generate sub-nanosecond pulses that are used as carriers to be transmitted through the wireless channel. The circuit that generates these pulses is generally called the pulse forming network (PFN). In the open literature, there are many PFNs that are designed for long range UWB radars [37]−[42]. However, most PFNs are unsuitable for high data rate UWB radio systems because of different requirements of the latter systems. In long range UWB radars, pulses are generated at medium to high power levels, *i.e.* watts to kilowatts, and at relatively low PRF, *i.e.* few kHz to tens of MHz [1]. In UWB radios [6], [42], and some high pulse rate UWB radar systems, however, pulses are generated at lower power levels and at higher PRF. UWB radios may require PRF to be in the order of several hundred MHz to GHz, for high data rate transmission in hundreds of Mbps to Gbps. UWB radars may require PRF to be in the order of several MHz to several hundred of MHz. Furthermore, a UWB radio system needs to be implemented in silicon integrated circuit to be economical in volume production. Pulse forming methods for long range UWB radars require specialized components like Step-Recovery Diodes [39], [40], avalanche transistors, non-linear transmission lines [37] *etc*. which are not amenable to implementation in silicon integrated circuit. Hence, a high data rate pulse forming network that is amenable to silicon integrated circuit will be presented in Chapter 5 of the thesis.

There are also a few designs in the open literature that designs UWB pulse forming networks in the integrated circuit. One of the methods for generating pulses for high data rate UWB communication is found in [43]. In this method, a differential clock signal is used as source signal. One of the differential signal pair is fed into more delay buffers than the other, creating two single ended clock signals of different delays. The two single ended signals are then combined using an exclusive OR gate to form a sub-nanosecond pulse. Another pulse forming network design [44] uses a tanh (hyper tangent) mixer to pulse shape a triangle generator, and mixes the pulse with a local oscillator. The output of the mixed signal is then bandpass filtered and amplified, before transmitted by an antenna. This circuit is implemented in 0.18-μm SiGe BiCMOS process and generates pulses that are 0.22V V_{pp} with a pulse-width of 3 ns. Besides that, another method of generating UWB pulses is with implementing a cascade of complex first-order filters [45]. These filters pulse-shape a triangular pulse to more Gaussian like in shape. The design of this pulse forming network is cascaded with a custom made, differentially fed ‘Butterfly’ antenna to be transmitted. This method is also implemented in 0.18-μm SiGe BiCMOS process, and generates pulses that are 0.21V V_{pp} with a pulse-width of 3 ns.

Chapter 6 presents a method of UWB radar in imaging the human body. The UWB radar detects a target by transmitting discrete electromagnetic pulses, and then receiving the scattered signals from the target [46]. The transmitted pulses has a short (sub-nanosecond) time interval, enabling the received scattered signals to provide accurate location information of the target [1]. Furthermore, because the transmitted pulses are also inherently wideband, the UWB radar receiver is able to collect much more information of the target from the scattered signals compared to narrowband radars [1]. It is reported in [47] that, because of its beneficial characteristics, the UWB radar is a potential candidate for non-invasive medical monitoring and imaging tool. In reference [47], however, the research effort is focused on UWB radars that work at frequencies below 1 GHz. Many research papers in the existing literature focus on imaging techniques employing (ultra-wideband) frequency scanning radars [48]−[50] rather than transmitting discrete electromagnetic pulses. On the other hand, some UWB radars have been developed [51], [52] to detect human breathing and heartbeat remotely.

Besides UWB radar, one emerging technology that can be used in imaging the human body is the Terahertz (THz) imaging technique. THz promises good cross-range resolution and a detection range of up to 25 m [53]. THz imaging may be a better candidate for breast cancer imaging [54] by virtue of its smaller sensor size, better range and cross-range resolution. However, there are still issues in generating the THz source, radiating and focusing the signal. THz imaging also require high end (and expensive) equipment.

1.2 Contributions

The first contribution of this thesis is in deriving a model to predict the UWB antenna characteristics during transmission and reception of pulses [55], [56]. UWB antenna introduces different signal distortions at different angles while transmitting and receiving UWB signals. To predict the extent of these angle-dependent signal distortions, the antennas have been modeled as impulse responses. The thesis has contributed in the derivation of the impulse response of the antenna from the field distribution of the antenna aperture, and in the verification of the theory with a ridged-horn antenna. The derivation enables us to predict the signal distortions of the UWB antennas in different angles analytically. It also helps in providing a better design method for UWB transceivers by taking into account of the antenna effect on UWB signals.

The second contribution of this thesis is in applying the impulse response of the antenna into resolving the received signals of a UWB array. Having the knowledge of signal distortion of the UWB array, we can then examine the effect of the signal distortion on the accuracy of UWB receivers in localizing a target, which has not been considered before. In one study, the impulse response of a time-difference-of-arrival (TDOA) array is derived, and applied in finding the range and angle accuracy of the TDOA receiver in the presence of antenna noise [57]. It is found that at high signal-to-noise ratios, the accuracy of the TDOA receiver can be adequately predicted. It is also found that the accuracy of the TDOA receiver deteriorates at larger off-boresight angles, primarily due to the pulse distortions of the antenna while receiving UWB signals at these angles.

In another study, the impulse response of a monopulse square-feed array consisting of four ridged-horns is derived [58]. The monopulse receiver performs angle discrimination by using the differences in the received signals' energy ratio and phase, rather than the time-of-arrivals, as being used in the TDOA receiver. The three received signals of the monopulse receiver – sum signal, azimuth difference signal and elevation difference signal are derived in consideration of the signal distortions by the monopulse array. The theoretical signals are shown to be accurate by measurements. A UWB monopulse receiver, consisting of a bank of cross-correlation circuits and an amplitude-comparison monopulse processor is proposed to estimate the angle-of-arrival of the incident signal. Then, the range and angle accuracy the UWB monopulse receiver in the presence of antenna noise is derived, and verified with measurements.

The third contribution of this thesis is in the design and fabrication of a UWB signal source that can be applied in high data rate UWB communication system or short range UWB radars [59], [60]. The signal source is a pulse forming network that is designed and fabricated in a BiCMOS integrated circuit. The pulse forming network is capable of generating pulses at a pulse repetition frequency of about 500 MHz, while consuming a DC power supply of 3.3 V and 20 mV during operation. The pulse forming network occupies 0.25 mm^2 of the IC chip. At the time of publication, the developed circuit was one of the earliest PFNs that is IC compatible, can generate pulses at greater than 500 MHz, and does not require an additional broadband amplifier.

The last contribution of this thesis is in proposing a UWB radar method to sense and image the human body for medical purposes [61]−[63]. The proposed method uses a single transmit / receive UWB radar to probe the human body, and then calculates the human body impulse response from the scattered signals. The proposed method is a new development from existing UWB radars in medical imaging since it probes the human body with time-domain UWB pulses, rather than (ultra-wideband) frequency scanning radars in [48]−[50]. Physical and dielectric characteristics of the human body can be interpreted from the impulse responses. In the process of verifying the UWB radar method, we have also proposed some human tissue phantoms that are simple, easily managed, and based on readily available liquids.

The contributions in the thesis has been submitted or published in the following journal and conference papers:

[1] A. E.-C. Tan, and M. Y.-W. Chia, “UWB Radar Transceiver and Measurement for Medical Imaging”, *IEEE BioCAS*, Singapore, Dec. 2004.

[2] A. E.-C. Tan, and M. Y.-W. Chia, “Method of Generating UWB Pulses”, *World Intellectual Property Organization*, Pub. No. WO 2005/067160 A1, Jul. 2005.

[3] A. E.-C. Tan and M. Y.-W. Chia, “Measuring Human Body Impulse Response Using UWB Radar”, *IEE Electron. Lett.*, vol. 41, no. 21, Oct. 2005, pp. 1193-1194.

[4] A. E.-C. Tan and M. Y.-W. Chia, “Measuring Human Body’s Impulse Response”, *UK-Singapore Bioelectronics Workshop*, Jan 2006.

[5] A. E.-C. Tan, M. Y.-W. Chia and S.-W. Leong, “Sub-nanosecond Pulse-Forming Network on SiGe BiCMOS for UWB Communications”, *IEEE Trans. MTT*, vol. 54, no. 3, Mar. 2006, pp. 1019-1024.

[6] K. Rambabu, A. E.-C. Tan, K. K.-M. Chan and M. Y.-W. Chia and S.-W. Leong, “Study of Antenna Effect on UWB Pulse Shape in Transmission and Reception”, *ISAP 2006*, Singapore, Nov. 2006.

[7] A. E.-C. Tan, M. Y.-W. Chia and K. Rambabu, “Design of Ultra-Wideband Monopulse Receiver”, *IEEE Trans. MTT*, vol. 54, no. 11, Nov. 2006, pp. 3821-3827.

[8] K. Rambabu, A. E.-C. Tan, K. K.-M. Chan and M. Y.-W. Chia, “Estimation of Antenna Effect on UWB Pulse Shape in Transmission and Reception”, submitted to *IEEE Trans. MTT*, Nov. 2006.

[9] A. E.-C. Tan, M. Y.-W. Chia and K. Rambabu, “Effect of Antenna Noise on Angle Estimation in Ultra-Wideband Receivers”, submitted to *IEEE Trans. AP*, Dec. 2006.

[10] A. E.-C. Tan, M. Y.-W. Chia and K. Rambabu, “Angle Accuracy of Antenna Noise Corrupted Ultra-Wideband Monopulse Receiver”, accepted for publication in *ICUWB 2007*, Sep. 2007.

1.3 Thesis Organization

In Chapter 2, an analytical model is proposed to describe the pulse distortions during the transmission and reception of UWB signals. It is expected that the pulse distortion is caused by the interaction between the UWB signals and the transmitting / receiving field distribution of the antenna apertures. Thus, the derivation involves providing a link between the antenna aperture’s field distribution function and the antenna’s impulse response.

In Chapter 3, a theoretical model predicting the AOA accuracy of the time-difference-of-arrival (TDOA) receiver array is proposed. This model considers several factors such as the incident signal, the antenna noise and the impulse response of the receiving antennas to derive the angle accuracy of the TDOA receiver. The proposed model predicts the TDOA accuracy as a probability density function. To verify the model, firstly, the root mean square error of the probability density function is calculated based on given parameters that describe certain conditions. Secondly, TDOA angle estimation experiments are performed under the described conditions, and the errors of the experiments are quantified in terms of root mean square error values, to be compared with the derived values.

In Chapter 4, a UWB monopulse square-feed array of four ridged-horns is used to estimate the angle-of-arrival of the incident signal instead. The array impulse response is derived so that pulse distortion caused by the monopulse array can be considered. A UWB monopulse receiver that is based on a bank of cross-correlation circuits and an amplitude-comparison monopulse processor is proposed. The range and angle accuracy of the UWB monopulse is derived and verified by measurements.

In Chapter 5, a design of UWB pulse forming network (PFN) is described. In the design, electrical pulses in the sub-nanosecond regime are generated specifically for high data rate UWB radio systems. The PFN is designed in SiGe BiCMOS, with small and readily available components like transistors, resistors and capacitors, for the ease of circuit integration. The PFN circuit occupies a small area 0.25 mm^2, making it suitable to be incorporated into portable high data rate transmitters like wireless video streaming and wireless personal area network (WPAN), or short range (< 0.3 m) UWB radars.

In Chapter 6, a UWB radar measurement method that measures the human body impulse response is proposed. In the method, the UWB radar transmits discrete second derivative Gaussian pulses onto the human body target, and receives the scattered signals from the target with an oscilloscope. The received signal is then processed to obtain the impulse response of the human body. A person’s body impulse response can be used to describe the electrical and physical properties of the person’s body.

Lastly, in Chapter 7, the conclusion of the thesis and a proposition of future work are presented.

CHAPTER 2

TRANSMISSION AND RECEPTION OF UWB PULSES

2.1 Introduction

Unlike narrowband radio systems, ultra-wideband (UWB) systems transmit and receive short (<1 ns) electromagnetic pulses. However, transmitting and receiving short electromagnetic pulses with inherently band limited antennas has resulted in unexpected shape distortions of the received pulses. Thus, predicting the pulse distortions is a real research challenge in UWB transceiver design and modeling. Experiments conducted to transmit and receive UWB signals [11], [12] have shown that the transmitted and received UWB signals suffer from different degrees of pulse distortion at different angles. Conventional antenna parameters like antenna gain and radiation pattern [14], while successful in explaining the transmission and reception of narrowband signals, fail to account for the pulse distortions in UWB signals.

In this chapter, we propose an analytical model to account for the pulse distortions at different angles during transmission and reception. It is expected that the pulse distortion is due to the interaction between the UWB signals and the radiating aperture of the antenna. Thus, the relationship between the antenna's aperture field distribution function and the antenna's pulse shaping effect on the UWB signals will be derived. From the derived relationship, we can predict the UWB signal shape in various angular positions during transmission and reception. Having the knowledge of this relationship will also help us to better understand the transmission and reception of UWB signals.

In relation to this Chapter, references [15] and [16] have proposed analytical models to describe the pulse shape variations in transmission and reception of UWB signals in simple antennas like monopoles, dipoles and loops. Furthermore, in references [17]−[19], by studying the antenna's sidelobe reception of electrically short pulses, Griffiths *et. al.* have defined the antenna impulse response to describe the pulse shaping effect of aperture antennas. In this chapter, we will adopt the definition of impulse response of an antenna to model the pulse shaping effect of aperture antennas in transmission and reception of UWB signals. In Section 2.2, we will establish the relationship between the antenna field distribution and the impulse response of the antenna. In Section 2.3, we will derive the field distribution function of a ridged-horn [64] aperture. Then, by applying the methods described in Section 2.2, we will derive the ridged-horn's transmission and reception effect on the pulse shapes of UWB signals at all angles. In Sections 2.4 and 2.5, the impulse responses of the ridged-horn in transmitting and receiving modes derived in Section 2.3 are verified with time-domain measurements at different angles.

2.2 Transmitting and Receiving Characteristics of an Aperture Antenna

In this section, we will derive the relationship between the impulse response of the antenna in transmitting and receiving mode and the field distribution of the antenna aperture. The derivation assumes that the radiated signal is measured at far-field distance [14], which is defined as $2D^2 / \lambda$, where D as the largest physical dimension of the radiating or receiving antenna. Because UWB signals occupy a large frequency spectrum, λ is defined as the wavelength associated to the upper −10 dB corner frequency, f_H, in accordance to FCC's definition [2]. Figure 2.1 shows the position of an antenna aperture (grey rectangle) and the position of a point at a far-field distance relative from the antenna aperture. Let S (x', y', 0) in Figure 2.1 be a point on the antenna aperture, and P (r, θ, φ) in Figure 2.1 be the other point at far-field distance.

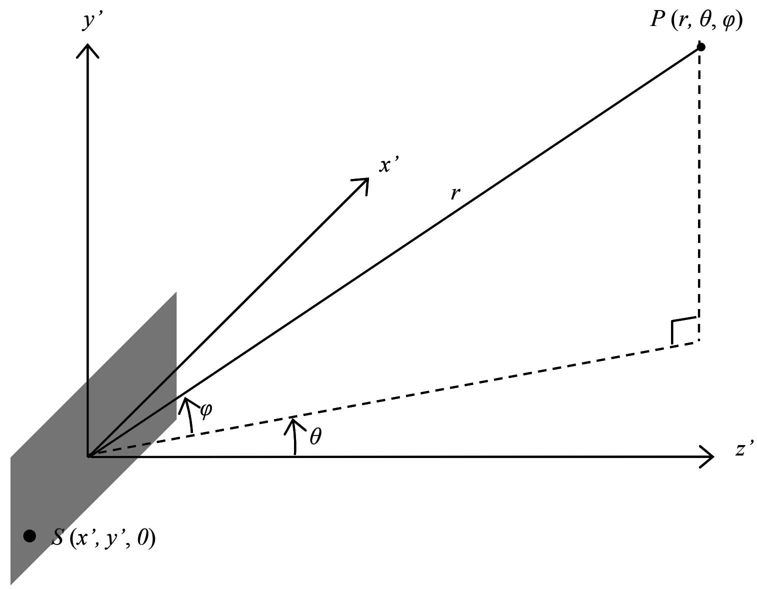

Figure 2.1: Antenna aperture (grey rectangle) and a point, *P*, in the far field distance.

Let the impulse response of the antenna in transmitting mode be f_t (t, θ, φ), and the impulse response of the antenna in receiving mode be f_r (t, θ, φ). To model the signal distortion on a source signal by the transmitting antenna, the source signal, s (t), is convolved with f_t (t, θ, φ) to form the transmitted UWB signal, e (t). To model the signal distortion of a transmitted signal by the receiving antenna, the transmitted signal, e (t), is convolved with f_r (t, θ, φ) to form the received UWB signal, r (t). Hence, the following relationship can be derived.

$$e(t) = f_t(t,\theta,\phi) \otimes s(t) \tag{2.1}$$

$$r(t) = f_r(t,\theta,\phi) \otimes e(t) = f_t(t,\theta,\phi) \otimes f_r(t,\theta,\phi) \otimes s(t) \tag{2.2}$$

Equation (2.1) shows the relationship between the source signal, s (t), and the radiated signal at far-field, e (t). If e (t) is received by an antenna placed at far-field distance, (2.2) shows the relationship between the source signal, s (t), and the received signal r (t). e (t) is the electrical field density (V m^{-1}) of the transmitted signal in far field, while s (t) and r (t) are electrical signal (V) at the output ports of the antenna. Hence, to maintain dimensional consistency, f_t (t, θ, φ) has a dimension of m^{-1} and f_r (t, θ, φ) has a dimension of m. The impulse response of the antenna in transmitting mode, f_t (t, θ, φ), is related to the impulse response of the antenna in receiving mode, f_r (t, θ, φ), as a time derivative [21].

$$f_t\left(t,\theta,\phi\right) = k_{(2.3)}\frac{d}{dt}f_r\left(t,\theta,\phi\right) \tag{2.3}$$

where $k_{(2.3)}$ is a proportionality constant that has a dimension of s m^{-2}. Substituting (2.3) into (2.2), the relationship between the source signal, s (t), and the received signal, r (t), can be rewritten as

$$r\left(t\right) = k_{(2.3)}f_r\left(t,\theta,\phi\right)\otimes f_r\left(t,\theta,\phi\right)\otimes\frac{d}{dt}s\left(t\right) \tag{2.4}$$

With reference to (2.4), when both the transmitter and receiver antennas are at boresight, f_r (t, θ = 0°, φ = 0°) = δ (t), and the received signal is proportional to the time derivative of the source signal. At off-boresight angles, however, the received signal can be found by time derivative of the source signal and two repeated convolutions with f_r (t, θ, φ). When expressed in frequency domain, the relationship between the source signal, S (ω), transmitted signal, E (ω), and received signal, R (ω), has the following relationship:

$$E\left(\omega\right) = F_t\left(\omega,\theta,\phi\right)\cdot S\left(\omega\right) \tag{2.5}$$

$$R\left(\omega\right) = F_r\left(\omega,\theta,\phi\right)\cdot E\left(\omega\right) = F_t\left(\omega,\theta,\phi\right)\cdot F_r\left(\omega,\theta,\phi\right)\cdot S\left(\omega\right) \tag{2.6}$$

where E (ω), R (ω), S (ω), F_r (ω, θ, φ) and F_t (ω, θ, φ) are the Fourier transform of e (t), r (t), s (t), f_r (t, θ, φ) and f_t (t, θ, φ) respectively. In frequency domain, the transfer function of the antenna in transmitting mode, F_t (ω, θ, φ), is related to the transfer function of the antenna in receiving mode, F_r (ω, θ, φ), as a multiplication of $j\omega$.

$$F_t\left(\omega,\theta,\phi\right) = j\omega k_{(2.3)} F_r\left(\omega,\theta,\phi\right) \tag{2.7}$$

Substituting (2.7) into (2.6), the transfer function relationship between the source signal, S (ω), and the received signal, R (ω), can be rewritten as

$$R\left(\omega\right) = j\omega k_{(2.3)} \left|F_r\left(\omega,\theta,\phi\right)\right|^2 S\left(\omega\right) \tag{2.8}$$

F_r (ω, θ, φ) is the frequency dependent normalized field pattern of the antenna. It has to be noted here that F_r (ω, θ, φ) provides no indication of the antenna's absolute gain [14]. This is because the antenna's absolute gain is also affected by other factors like insertion loss and radiation efficiency. In the far-field, the normalized field pattern of the antenna, F_r (ω, θ, φ), is related to the field distribution of the antenna aperture g (x', y') [30] as

$$F_r\left(\omega,\theta,\phi\right) = k_{(2.9)} \iint_{area} g\left(x',y'\right) \exp\left[\frac{j\omega}{c}\sin\theta\left(x'\cos\phi + y'\sin\phi\right)\right] dx'dy' \tag{2.9}$$

where c is the speed of light in free space, $k_{(2.9)}$ is a constant of proportionality, and (x', y') are the coordinates of the aperture field distribution function g (x', y'). The geometrical relationship between (x', y', z') and (r, θ, φ) in (2.9) are shown in Figure 2.1. The aperture field distribution function, g (x', y'), has non-zero values within the area of integration in (2.9), which corresponds to the area of aperture's physical boundary (the grey rectangle in Figure 2.1) of x' = [$-\alpha$ / 2, α / 2] and y' = [$-\beta$ / 2,

β / 2]. Assuming aperture field orthogonality along the x' and y' axes, i.e. $g(x', y') = g_1(x').g_2(y')$, $F_r(\omega, \theta, \varphi)$ of (2.9) can be rewritten as

$$F_r(\omega,\theta,\phi) = \int_{-\alpha/2}^{\alpha/2} g_1(x')\exp\left(\frac{j\omega}{c}x'\sin\theta\cos\phi\right)dx' \int_{-\beta/2}^{\beta/2} g_2(y')\exp\left(\frac{j\omega}{c}y'\sin\theta\sin\phi\right)dy' \quad (2.10)$$

Equation (2.10) relates the antenna's normalized field pattern, $F_r(\omega, \theta, \varphi)$, with the aperture field distribution, $g(x', y')$, as a spatial Fourier transform pair. Rewriting (2.10) by applying a change in variable of $x' = -ct / \sin\theta\cos\varphi$ and $y' = -ct / \sin\theta\sin\varphi$, $F_r(\omega, \theta, \varphi)$ can be expressed as

$$F_r(\omega,\theta,\phi) = \frac{c^2}{\sin^2\theta\sin\phi\cos\phi}\int_{-\tau_\alpha/2}^{\tau_\alpha/2} g_1\left(\frac{ct}{\sin\theta\cos\phi}\right)e^{j\omega t}dt \cdot \int_{-\tau_\beta/2}^{\tau_\beta/2} g_2\left(\frac{ct}{\sin\theta\sin\phi}\right)e^{j\omega t}dt \quad (2.11)$$

where $\tau_\alpha = \alpha\sin\theta\cos\varphi / c$ and $\tau_\beta = \beta\sin\theta\sin\varphi / c$. The normalized field pattern, $F_r(\omega, \theta, \varphi)$ in (2.11), is the Fourier transform of the impulse response of the antenna in receiving mode, $f_r(t, \theta, \varphi)$. Thus, by taking inverse Fourier transform of $F_r(\omega, \theta, \varphi)$ in (2.11), $f_r(t, \theta, \varphi)$ can be derived as

$$f_r(t,\theta,\phi) \propto \begin{cases} \dfrac{1}{\sin\theta\cos\phi}g_1\left(\dfrac{ct}{\sin\theta\cos\phi}\right)\left[u\left(t+\dfrac{\tau_\alpha}{2}\right)-u\left(t-\dfrac{\tau_\alpha}{2}\right)\right]\otimes \\ \dfrac{1}{\sin\theta\sin\phi}g_2\left(\dfrac{ct}{\sin\theta\sin\phi}\right)\left[u\left(t+\dfrac{\tau_\beta}{2}\right)-u\left(t-\dfrac{\tau_\beta}{2}\right)\right] \end{cases} \quad (2.12)$$

where $u(t)$ is a unit step function, as defined in [66]. Lastly, the impulse response of the antenna in transmitting mode, $f_t(t, \theta, \varphi)$, can be derived by performing time derivative on (2.12).

2.3 Transmitting and Receiving Characteristics of Ridged-Horns

In this section, the impulse response of a ridge horn antenna is derived for both the transmitting and the receiving mode. Ridged-horns can achieve an operating bandwidth that is more than a decade wide, as reported in [64]. This is because the ridged-horn's $TE_{1,0}$ mode cut-off frequency has been significantly extended by the ridges [65]. Furthermore, if we neglect the effect of phase difference due to wave propagation from the ridged-horn's apex to the aperture, the field distribution of the ridged-horn aperture does not change with respect to frequency. The ridges, however, concentrate the field intensity there [65]. This reduces the absolute gain of ridged-horn antennas, if compared to a pyramidal-horn antenna of the same aperture size [64].

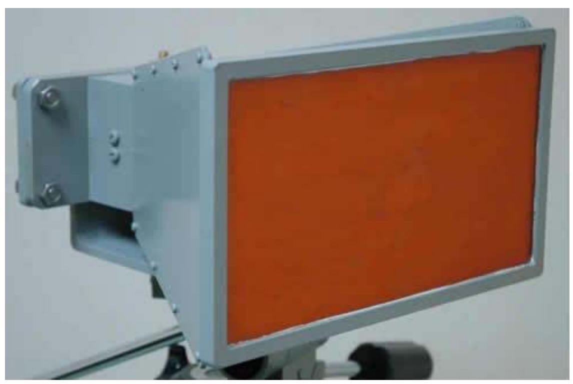

Figure 2.2: Picture of the double-ridged horn by RCM Ltd. (model MDRH-1018).

Figure 2.2 shows a picture of the ridged-horn antenna modeled in this section, and Figure 2.3 shows a structural representation of the ridged-horn's aperture and the typical field distribution (dashed line) of the ridged-horn aperture. To model the increased field intensity around the ridges, as shown in Figure 2.3, the field distribution of the ridged-horn aperture is expressed as a pyramidal horn aperture function [14], but with the addition of a power term.

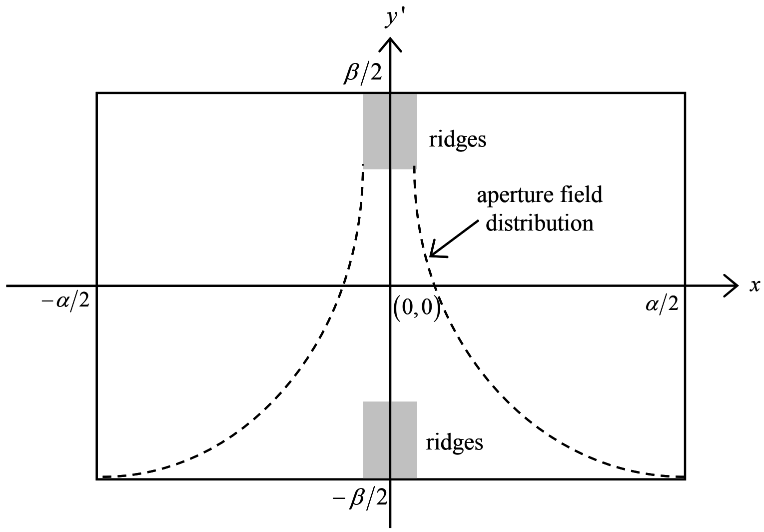

Figure 2.3: The ridged-horn's aperture dimensions and a typical field distribution (dashed line) of the ridged-horn aperture.

The expression of the ridged-horn aperture field distribution function is

$$g(x',y') = \cos^m\left(\frac{\pi x'}{\alpha}\right)\cdot\left[u\left(x'+\frac{\alpha}{2}\right)-u\left(x'-\frac{\alpha}{2}\right)\right]\cdot\cos^n\left(\frac{\pi y'}{\beta}\right)\cdot\left[u\left(y'+\frac{\beta}{2}\right)-u\left(y'-\frac{\beta}{2}\right)\right] \quad (2.13)$$

where α and β are dimensions of the ridged-horn aperture, as defined in Figure 2.3. The terms $\cos^m$ (…) and $\cos^n$ (…) models the aperture field concentration of the ridged-horn aperture along the broad wall (*x'* direction) and narrow wall (*y'* direction) respectively. *m* and *n* are positive integers, and their values are dependent on the ridge dimensions. The impulse response of the ridged-horn antenna in the receiving mode can be derived from (2.13), by applying (2.12) of Section 2.2,

$$f_r(t,\theta,\phi) \propto \left\{ \begin{array}{l} \dfrac{1}{\sin\theta\cos\phi}\cos^m\left(\dfrac{\pi ct}{\alpha\sin\theta\cos\phi}\right)\cdot\left[u\left(t+\dfrac{\tau_\alpha}{2}\right)-u\left(t-\dfrac{\tau_\alpha}{2}\right)\right]\otimes \\ \dfrac{1}{\sin\theta\sin\phi}\cos^n\left(\dfrac{\pi ct}{\alpha\sin\theta\sin\phi}\right)\cdot\left[u\left(t+\dfrac{\tau_\beta}{2}\right)-u\left(t-\dfrac{\tau_\beta}{2}\right)\right] \end{array} \right. \quad (2.14)$$

The impulse response of the ridged-horn in transmitting mode can be derived by performing time derivative on (2.14). In the next section, the integers *m* and *n* in (2.14) will be experimentally determined for the double ridged-horn shown in Figure 2.2; and equation (2.14) will be verified by comparison with time-domain measurements of the same ridged-horn.

2.4 Experimental Verification: Impulse Response of the Antenna in Receiving Mode

In this section, we present the time-domain measurements of received UWB signal through the double ridged-horn antenna shown in Figure 2.2.

Because time domain measurements are conducted in all chapters of the thesis, we will elaborate more on the measurement techniques and related issues in this section. In time domain measurements, the source is generated by a fast rise-time generator (*e.g*. Picosecond model 4050B pulse generator, Anritsu Pulse Pattern Generator MP1763C), which outputs a constant train of fast steps to be pulse-shaped by a pulse forming network (*e.g*. Picosecond model 5216 impulse forming network, the pulse forming network designed in Chapter 5). A few pulse forming networks are cascaded to generate higher order differentiations of the Gaussian pulse. Besides generating the step function, the fast rise-time generator also outputs a synchronizing signal so that a sampling oscilloscope can be triggered to measure the received signal. The sampling oscilloscope used in all the measurements is the Agilent Infiniium DCA model 86100B wide-bandwidth oscilloscope, which is able to sample the signal at speeds up to 50 GS/s. The sampling oscilloscope, triggered by the synchronizing signal, measures the received signal. The absolute delay of the measured signal can be calculated from the measured delay of the sampling oscilloscope and the delay of the coaxial like that connects the source trigger and the synchronizing port of the oscilloscope. The RMS time jitter of the measurement is equal to the sum of RMS jitter specifications of the source and the oscilloscope.

One of the problems of UWB measurement is the thermal noise power is proportional to the receiver bandwidth, and the receiver bandwidth has to be higher than the signal bandwidth. Hence, thermal noise contribution to the total signal is substantial in our measurement system. To obtain a clean signal for analysis, thermal noise contribution has to be reduced by performing signal averaging at the sampling oscilloscope. By averaging a large number of received waveforms, the thermal noise, being statistically independent at all times, is being averaged out; the desired received signal however, being a consistent value at all times in the measurement, remains constant. However, signal averaging takes a long time. For example, 1024 averaging takes 1+ minute, while 4096 averaging takes 5 minutes to complete one measurement. Hence, in most measurements done in this research, 1024 averages are used. Only in Chapter 4, where the received signal is very small in value, and 1024 averaging is insufficient to average out the noise contribution, 4096 averaging is used.

In UWB antenna measurement, the far-field region can be defined as $2D^2 / \lambda$, where λ corresponds to the wavelength of the upper −10 dB edge frequency. For the ridged horn, because the field distribution is concentrated at the centre of the aperture, the antenna largest dimension, D, is measured from the region where the aperture field strength is higher than 1 % (−20 dB) of the maximum field strength. For the case of the double-ridged horn by RCM Ltd. (model MDRH-1018) radiating a UWB signal with an upper −10 dB edge frequency of 10 GHz, the far-field distance is 1.8 meters. The measurement is done at a distance of 4.0 meters, which is well beyond the far-field distance.

There are many possible sources of measurement errors that need to be considered during the measurement. One source of measurement error may be caused by the signal distortion contributed by the coaxial cable that connects the receiving antenna and sampling oscilloscope. To minimize this source of error, a good quality semi-rigid coaxial cable is used. Before using it, the dispersion of the coaxial cable on the UWB signal need to be evaluated, and could only be used if the dispersion contribution to the pulse lengthening is less than 1% of the signal pulse width. Another possible source of measurement error is the jitter between the source and synchronizing signals may cause some errors in the measurement. This source of error can be reduced in two manners – ensuring the source and oscilloscope RMS jitter is much less than the pulse width of the measured signal, and by performing signal averaging. The next source of error is that the measurement environment may not be constant within the measurement period. Non-constant measurement environment are contributed by antenna positional change, undesired signal interferers and component time-shifts. These sources of errors can be severe when signal averaging is used, and the time taken to measure an averaged signal may take several minutes. So, to minimize these errors, firstly, we have to ensure that the measurement environment remains constant within the time of measurement. Secondly, if we use amplifiers in the measurement, we need to turn on the amplifiers for a while, until the time-shifts caused by temperature change of the circuit become constant.

The measured received signal is compared with the derived received signal using (2.14). The ridged-horn has a return loss of < −10 dB and gain of 5-16 dBi in the frequency range of 1-18 GHz. The aperture dimensions of the ridged-horn are α = 0.236 m and β = 0.129 m.

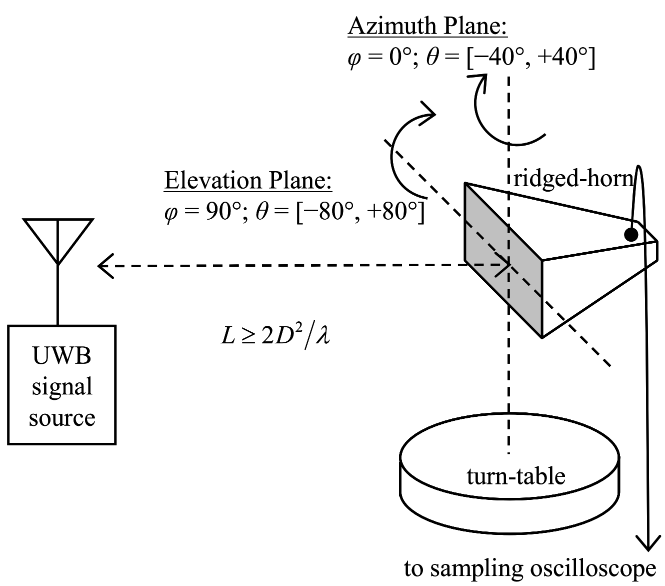

Figure 2.4: Experimental setup for time-domain measurement of received signal at different angles.

The ridged-horn is placed on a turn-table, which rotates at 2° intervals from −40° to +40° in the azimuth plane, and from −80° to +80° in the elevation plane. Azimuth plane is defined as rotation at φ = 0°, as shown in Figure 2.4; While elevation plane is defined as rotation at φ = 90°, as shown in Figure 2.4. In the measurement, the transmitted UWB signal received by the ridged-horn antenna is captured with a 40 GS/s sampling oscilloscope at the specified angles. The captured received signal is averaged 1024 times to increase the signal-to-noise ratio (SNR).

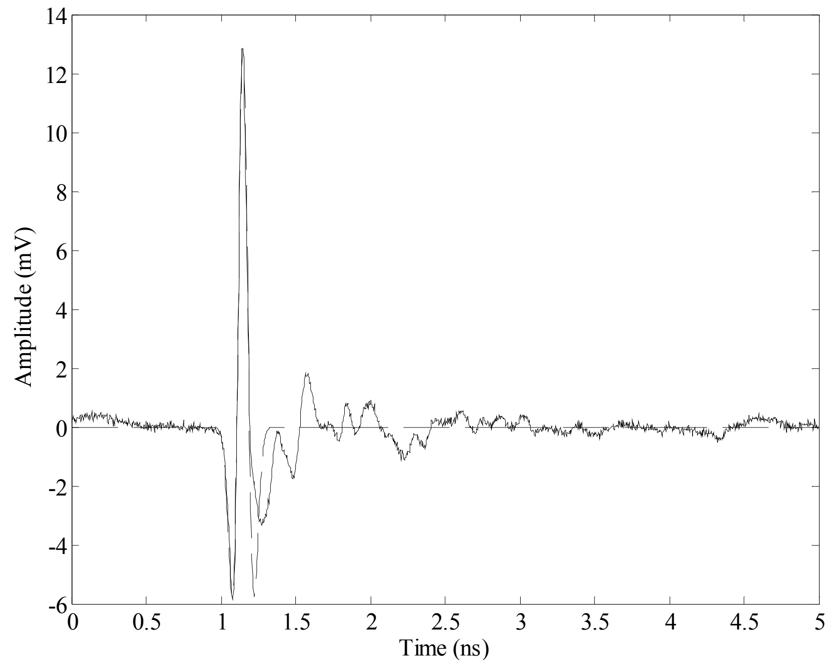

Figure 2.5: Measured (line) and modeled (dashed line) transmitted UWB signal.

The UWB signal source generates a Gaussian first derivative pulse, and is transmitted by a ridged-horn antenna. The transmitted UWB signal, shown in Figure 2.5 (line) has been measured by a ridged-horn antenna at boresight direction. The transmitted UWB signal is then modeled as e (t), a 250 ps (10% pulsewidth) Gaussian second derivative pulse (Figure 2.5, dashed line)

$$e(t) = A_e\left[\frac{2}{{\tau_e}^2}(t-d_e)^2 - 1\right]\exp\left[\frac{(t-d_e)^2}{{\tau_e}^2}\right] \tag{2.15}$$

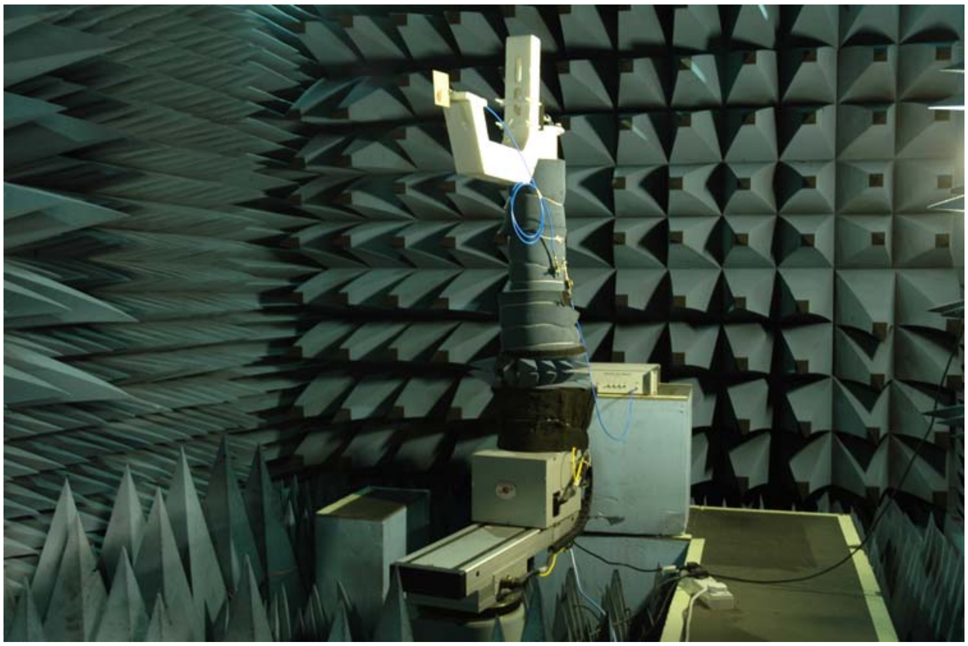

Figure 2.6: A picture of the transmitter setup in the measurement.

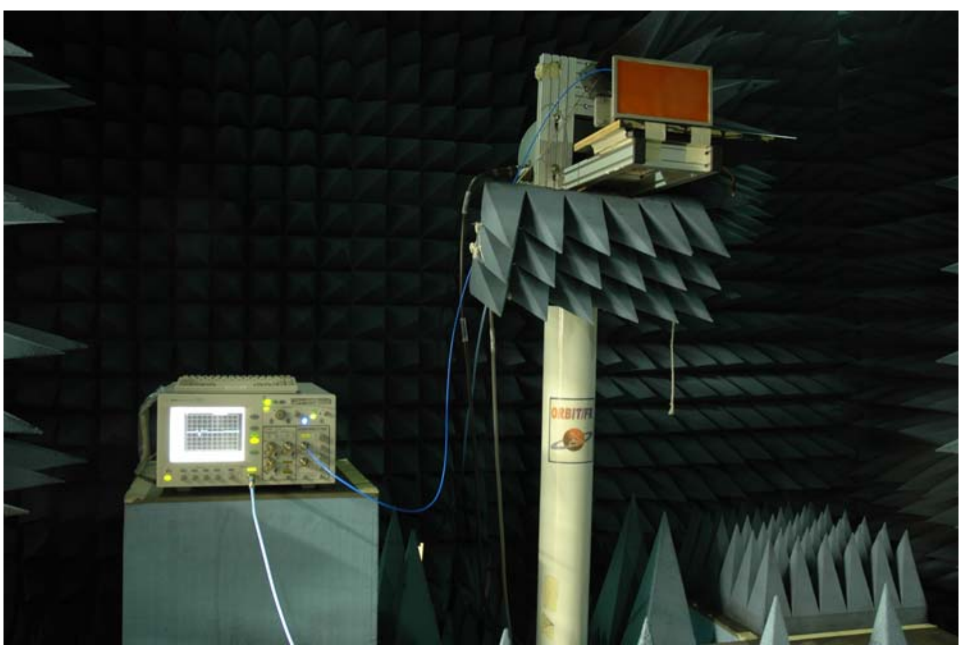

Figure 2.7: A picture of the receiver setup in the measurement.

with A_e = 12.9 mV, d_e = 1.2 ns and τ_e = 60 ps. A_e, d_e and τ_e are parameters that determines the amplitude, delay and pulsewidth of the radiated UWB signal. Fig. 2.6 shows a picture of the transmitter setup in the measurement, while Fig. 2.7 shows a picture of the receiver setup in the measurement. The shape of the UWB signal received by the ridged-horn is measured and then compared with the theoretical received signal. To find the theoretical received signal, we require the knowledge of the impulse response of the antenna in receiving mode, f_r (t, θ, φ). In the azimuth plane, f_r (t, θ, φ) can be derived from (2.14) by a substitution of $\varphi = 0°$,

$$f_r\left(t,\theta,\phi=0°\right) \propto \frac{1}{\sin\theta}\cos^m\left(\frac{\pi ct}{\alpha\sin\theta}\right)\cdot\left[u\left(t+\frac{\tau_\alpha}{2}\right)-u\left(t-\frac{\tau_\alpha}{2}\right)\right] \tag{2.16}$$

where $\tau_\alpha = \alpha \sin \theta / c$. The theoretical received signal in azimuth plane can be calculated by convolving the incident signal of (2.15) with (2.16). The impulse response of the antenna in receiving mode in the elevation plane can be derived from (2.14) by a substitution of $\varphi = 90°$,

$$f_r\left(t,\theta,\phi=90°\right) \propto \frac{1}{\sin\theta}\cos^n\left(\frac{\pi ct}{\alpha\sin\theta}\right)\cdot\left[u\left(t+\frac{\tau_\beta}{2}\right)-u\left(t-\frac{\tau_\beta}{2}\right)\right] \tag{2.17}$$

where $\tau_\beta = \beta \sin \theta / c$. The theoretical received signal in elevation plane can be calculated by convolving the incident signal of (2.15) with (2.17). By comparing the off-boresight signal amplitudes of the measured signals with (2.16) and (2.17), it is found that m = 12 and n = 4 result in a good agreement between theoretical and measured received signal. The details of measurement and comparison will be presented in page 79 of Chapter 4.

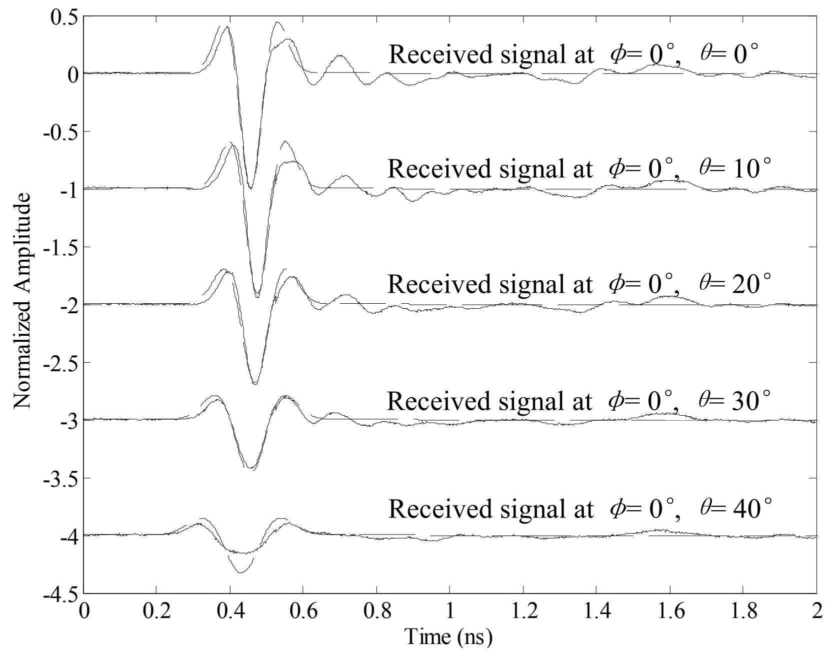

Figure 2.8: Measured (line) and modeled (dashed line) received signal in the azimuth plane.

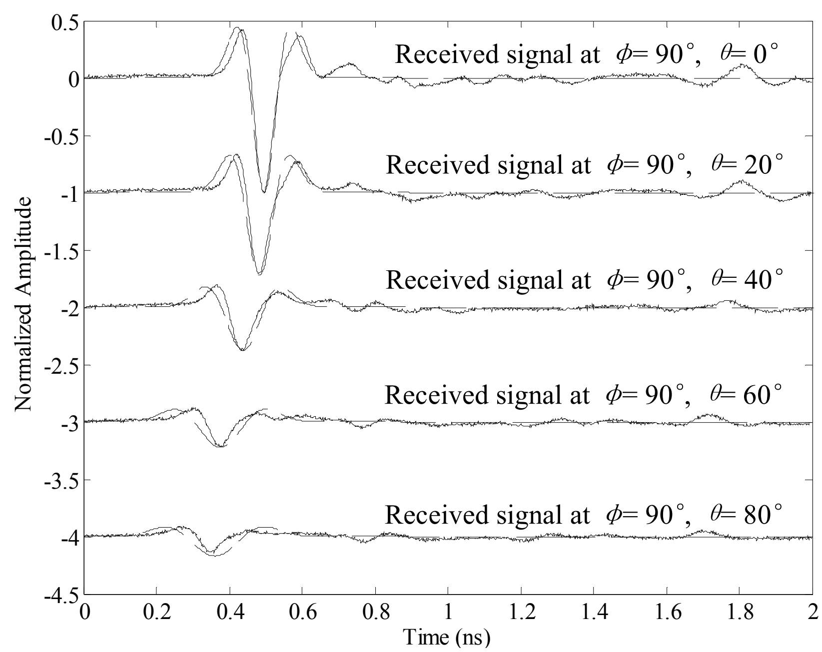

Figure 2.9: Measured (line) and modeled (dashed line) received signal in the elevation plane.

Figure 2.8 shows the signal shape comparison between the theoretical (dashed line) and the measured received signal (line) in the azimuth plane. Figure 2.9 shows the signal shape comparison between the theoretical (dashed line) and the measured received signal (line) in the elevation plane. The comparisons in Figures 2.8 and 2.9 show good agreements between the theoretical and measured received signals. The antenna energy gain is defined as the energy of the received UWB signal at an angle normalized with the energy of the received UWB signal at boresight. The received UWB signal is calculated from convolving (2.16) and (2.17) with the incident signal (2.15). The theoretical antenna energy gain is compared with measured result for both elevation and azimuth planes. Figures 2.10 and 2.11 shows the comparisons between measured (line) and theoretical (crosses) antenna energy gain for both azimuth and elevation planes respectively. The comparisons show good agreements between the theoretical and measured antenna energy gain. Both measurements of received UWB signal and antenna energy gains verify the accuracy of the impulse response of the ridged-horn antenna in reception mode formulations in Sections 2.2 and 2.3.

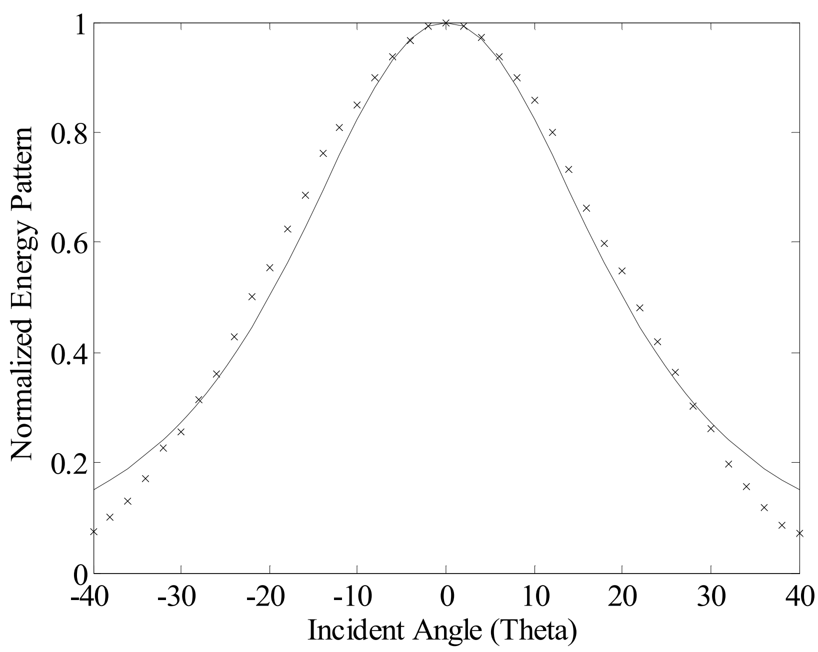

Figure 2.10: Measured (crosses) and modeled (line) antenna energy pattern in the azimuth plane.

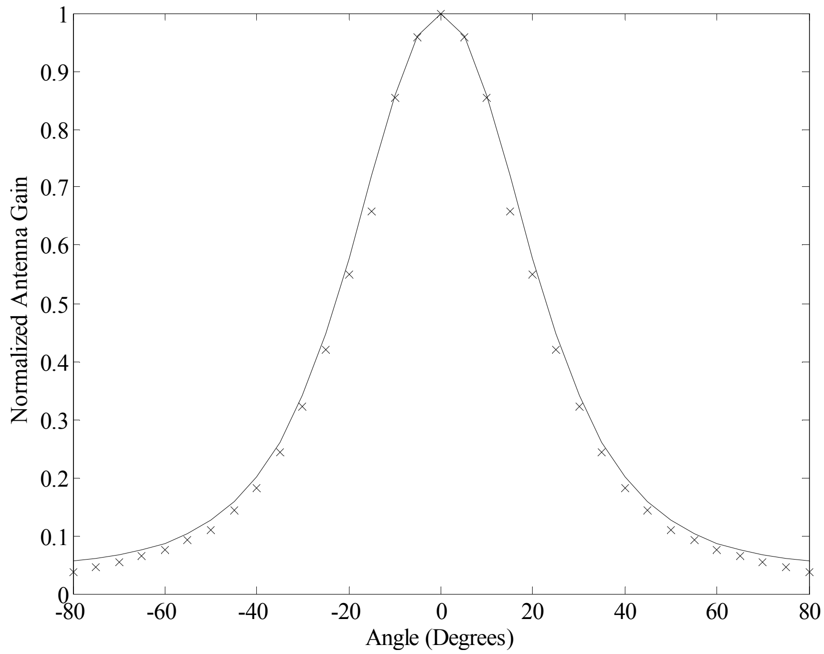

Figure 2.11: Measured (crosses) and modeled (line) antenna energy gain in the elevation plane.

2.5 Experimental Verification: Impulse Response of the Antenna in Transmitting Mode

In this section, we will experimentally verify the impulse response of the antenna in transmitting mode. As shown in (2.3), the impulse response of the antenna in transmitting mode, $f_t\ (t, \theta, \varphi)$, is defined as the time derivative of the impulse response of the antenna in receiving mode. Direct verification of $f_t\ (t, \theta, \varphi)$ by measurement is not possible because we have no means of measuring the transmitted signal without further distorting it. To measure the transmitted signal, we have to receive it with another antenna at far-field distance. So, besides being distorted by the impulse response of the antenna in transmitting mode, the source signal is distorted by the frequency-limited gain of the transmitting antenna, attenuation in free-space, frequency-limited gain of the receiving antenna and the impulse response of the receiving antenna. So, in order to verify the impulse response of the antenna in transmitting mode, we have to model all of the above-mentioned distortions of the UWB signal. The modeled signal is verified by the received signal that is transmitted and received by the specific antennas.

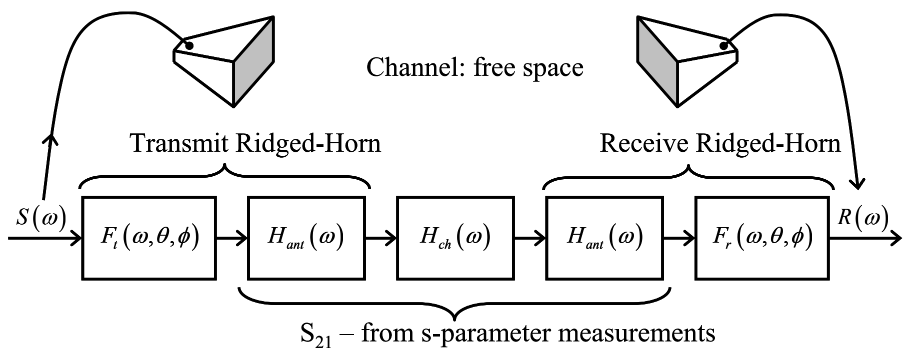

Figure 2.12: Transfer functions used to model the transmission and reception of UWB pulses.

Figure 2.12 shows the model we propose to account for the distortions of the UWB signal during transmission, propagation and reception. In Figure 2.10, to arrive at the received signal R (ω), the source signal S (ω) is filtered by F_t (ω, θ_t, φ_t), H_t (ω), H_{ch} (ω), H_r (ω) and F_r (ω, θ_r, φ_r). In the proposed mode, the transmitting antenna is represented by F_t (ω, θ_t, φ_t) and H_t (ω). F_t (ω, θ_t, φ_t) models the impulse response of the antenna in transmitting mode, and H_{ant} (ω) models the frequency-limited antenna gain. θ_t and φ_t are the angles of the transmitting antenna relative to the transmitting antenna's boresight. The radiated UWB signal propagates in free space, reaching the receiving antenna in a far-field distance.

The attenuation due to free-space propagation is modeled as the transfer function H_{ch} (ω). The receiving antenna is represented by a cascade of F_r (ω, θ_r, φ_r) and H_r (ω). F_r (ω, θ_r, φ_r) models the impulse response of the antenna in receiving mode, and H_r (ω), models the frequency-limited antenna gain. θ_t and φ_t are the angles of the transmitting antenna relative to the transmitting antenna's boresight. Since a matched pair of antennas will be used in the experiment, the frequency limited antenna gain is the same for both the transmitting and receiving antennas, *i.e.*, H_t (ω) = H_r (ω). The combined effect of the transmitting antenna's frequency-limited gain, H_t (ω), attenuation due to propagation in free-space, $H_{ch}(\omega)$, and the receiving antenna's frequency-limited gain, $H_r(\omega)$, can be found from s-parameter measurement, which will be discussed later in this section.

From Figure 2.12, the relationship between the received and source UWB signal can be expressed, in frequency and time domain, as

$$R(\omega) = F_t(\omega, \theta_t, \phi_t) \cdot H_t(\omega) \cdot H_{ch}(\omega) \cdot H_r(\omega) \cdot F_r(\omega, \theta_r, \phi_r) \cdot S(\omega) \tag{2.18}$$

$$r(t) = f_t(t, \theta_t, \phi_t) \otimes h_t(t) \otimes h_{ch}(t) \otimes h_r(t) \otimes f_r(t, \theta_r, \phi_r) \otimes s(t) \tag{2.19}$$

Let the source signal shown in Figure 2.12 be a Gaussian first derivative pulse. In time domain,

$$s(t) = A_s(t - d_s)\exp\left[-\frac{(t-d_s)^2}{\tau_s^{\,2}}\right] \tag{2.20}$$

where A_s, d_s and τ_s model the amplitude, absolute delay and pulse width of the source pulse respectively. In frequency domain,

$$S(\omega) = j\omega\sqrt{\pi}\tau_s^{\,3}\frac{A_s}{2}\exp\left(\frac{\tau_s^{\,2}\omega^2}{4}\right)\exp(-j\omega d_s) \tag{2.21}$$

Figure 2.13 shows the comparison between the measured source signal (line) and the modeled source signal, in time-domain, with τ_s = 35 ps (dashed line).

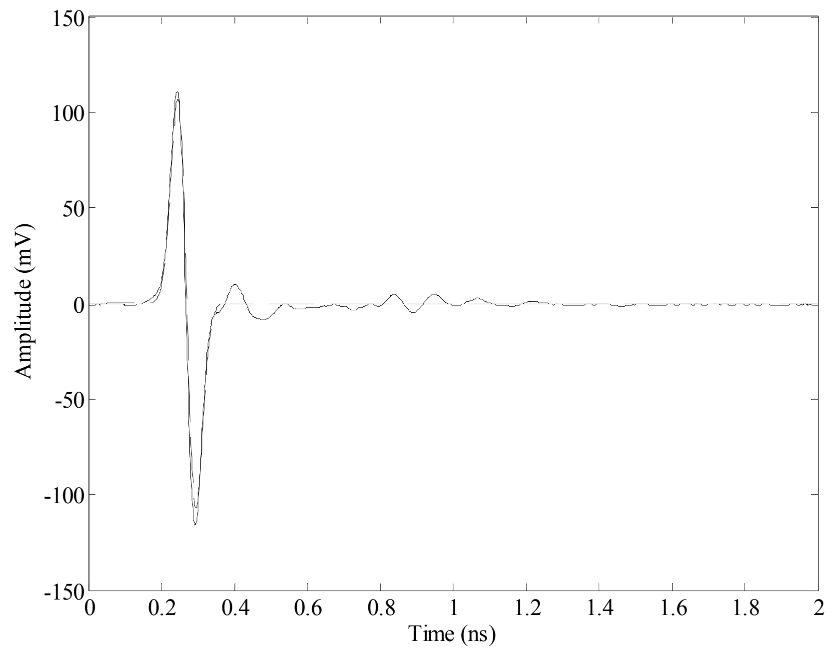

Figure 2.13: Measured (line) and theoretical (dashed line) UWB source signal.

As mentioned earlier, the UWB signal distortion due to the transmitting antenna's frequency-limited gain H_t (ω), propagation in free-space H_{ch} (ω) and the receiving antenna's frequency-limited gain H_r (ω) can be determined from s-parameter measurement. The s-parameter measurement is conducted in an anechoic chamber. In the measurement, two similar double-ridged horns by RCM Ltd (model MDRH-1018) are placed apart in far-field distance at boresight direction. Ports 1 and 2 of the vector network analyzer (VNA) are first calibrated with SOTL (short / open / through / load) standards before starting the measurements. During the calibration, the plane of reference is set at the input ports of the transmitting and receiving antennas, so that cable losses is calibrated out from the measurement.

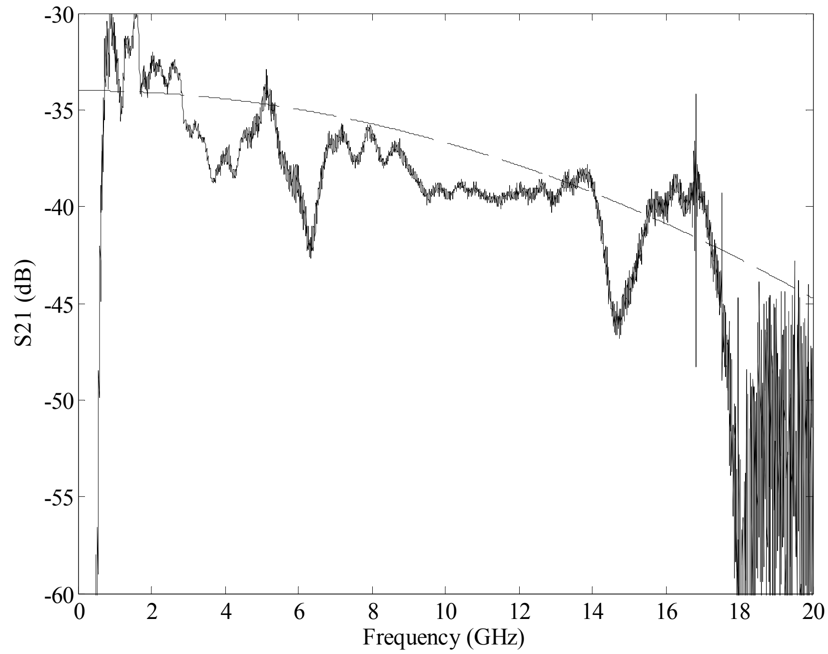

Figure 2.14: Measured (line) and theoretical (dashed line) transfer functions used to model the transmitting antenna's frequency-limited gain, $H_t(\omega)$, attenuation due to propagation in free-space, $H_{ch}(\omega)$ and the receiving antenna's frequency-limited gain, $H_r(\omega)$.

Figure 2.14 shows the measured S_{21} (dB) trace (line). The measured S_{21} exhibits severe attenuation at frequencies from DC to 1 GHz, since these frequencies are not within the operating frequency of the ridged-horn. From 1 GHz to 17 GHz, the S_{21} is gently sloping downward from −33 dB to −43 dB. S_{21} readings at frequencies beyond 17 GHz are discarded because the signal power is too low, and the readings are corrupted by high noise levels. The measured $|S_{21}|$ data can be modeled as a gently sloping Gaussian curve

$$H_t(\omega)\cdot H_{ch}(\omega)\cdot H_r(\omega) \cong A_{ch}\exp\left(-\frac{\omega^2}{4\omega_{ch}^{\ 2}}\right) \tag{2.22}$$

where A_{ch} models the overall (frequency independent) attenuation, while ω_{ch} models the slope of the frequency dependent attenuations. The measured S_{21} trace in Figure 2.14 is modeled (dashed line) with a gently sloping Gaussian curve of A_{ch} = 4.0e-4 and $\omega_{ch} = 2\pi$ (9.0 GHz).

Substituting (2.22) into the cascade of transfer functions in Figure 2.12, the theoretical relationship between the source and received signal can be expressed as

$$R(\omega) = F_t(\omega,\theta_t,\phi_t)\cdot A_{ch}\exp\left(-\frac{\omega^2}{4{\omega_{ch}}^2}\right)\cdot F_r(\omega,\theta_r,\phi_r)\cdot S(\omega) \tag{2.23}$$

By performing inverse Fourier transform on (2.23), and substituting the source signal (2.20), the time-domain expression of the received signal can be derived as

$$r(t) \propto f_t(t,\theta_t,\phi_t)\otimes f_r(t,\theta_r,\phi_r)\otimes(t-d_s)\exp\left[-\left(\frac{t-d_s}{\tau_s+\sqrt{2}/\omega_{ch}}\right)^2\right] \tag{2.24}$$

Equation (2.24) shows the effect of propagation, transmitting and receiving ridged-horn antennas on the UWB source signal, which is pulse lengthening of $\sqrt{2}/\omega_{ch} = 25$ ps, convolution with f_t (t, θ_t, φ_t) and convolution with f_r (t, θ_r, φ_r), depending on the angle of interest. Equation (2.24) is then verified by time-domain measurements of received UWB signal. Because f_t (t, θ_t, φ_t) is a time-derivative of f_r (t, θ_r, φ_r), and differentiation is associative with respect to convolution, equation (2.24) can be re-written as

$$r(t) \propto f_r(t,\theta_t,\phi_t)\otimes f_r(t,\theta_r,\phi_r)\otimes\frac{d}{dt}\left\{(t-d_s)\exp\left[-\left(\frac{t-d_s}{\tau_s+\sqrt{2}/\omega_{ch}}\right)^2\right]\right\} \tag{2.25}$$

To further simplify (2.25), the reference plane of the transmitting and receiving antennas are changed, from their respective boresight, to (θ_t, φ_t). The change causes the angle of the transmitting antenna, relative to itself, become (θ_t = 0, φ_t = 0); and the angle of the receiving antenna, relative to the transmitting antenna, become ($\theta = \theta_r - \theta_t$, $\varphi = \varphi_r - \varphi_t$). Thus, equation (2.25) can be simplified to

$$r(t) \propto f_r(t,\theta,\phi) \otimes \frac{d}{dt}\left\{(t-d_s)\exp\left[-\left(\frac{t-d_s}{\tau_s + \sqrt{2}/\omega_{ch}}\right)^2\right]\right\} \tag{2.26}$$

where θ and φ are defined as the angle of the receiving antenna relative to the transmitting antenna.

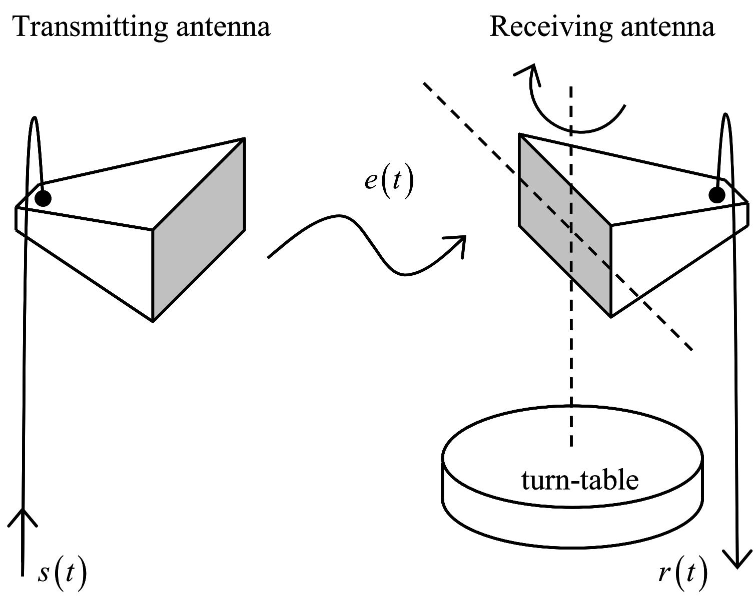

Figure 2.15: Experimental setup used to measure the received UWB signal.

Figure 2.15 shows the experimental setup to measure the received UWB signal. In the setup, two similar double-ridged horns by RCM Ltd (model MDRH-1018) are placed apart in far-field distance. The direction of the transmitting ridged-horn is fixed at boresight while the receiving ridged-horn is able to rotate along the azimuth plane. The received signals at various angles are recorded with a 40 GS/s sampling oscilloscope, with averaging of 1024 times.

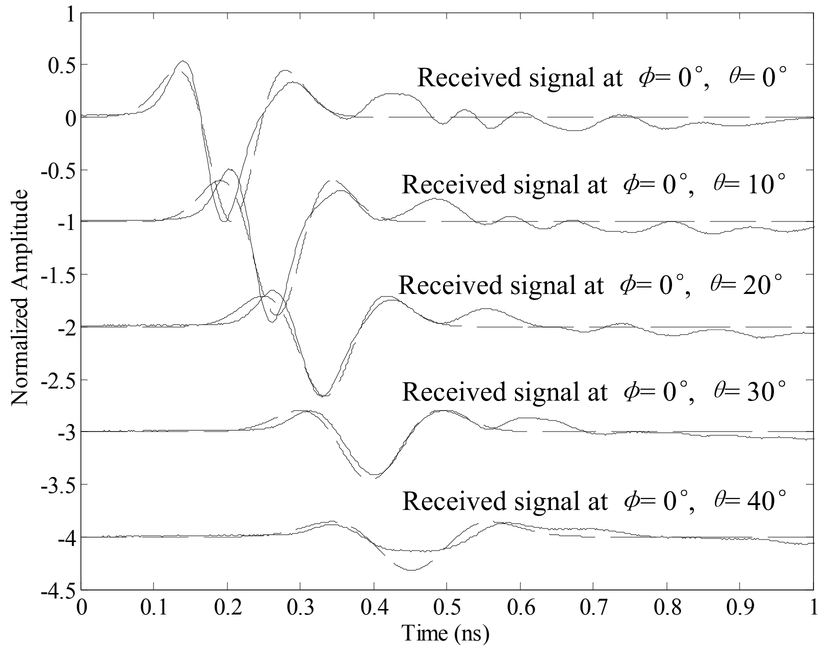

Figure 2.16: Measured (line) and modeled (dashed line) received signal in the azimuth plane.

The theoretical received signals (dashed line) calculated from (2.24) at various angles in the azimuth plane are compared with measured received signal (line) in Figure 2.16. Comparisons show good agreements in terms of pulse width and amplitudes between the calculated and measured signals, verifying the accuracy of the impulse response of the antenna in transmitting mode in predicting the pulse shape changes at different angles.

2.6 Chapter Summary

In this chapter we derived impulse response of the transmitting and receiving antennas and then modeled the angle dependent pulse distortion due to the antennas. Using the proposed models, we have formulated a relationship between the antenna's aperture field distribution and the antenna's impulse responses. We have also formulated a relationship between UWB source signal, transmitted signal and received signal. This formulation then is applied to a ridged-horn antenna and is being verified by measurements. In the first measurement, the impulse response of the ridged-horn in receiving mode is compared with direct measurement of received signals. In the second measurement, the impulse response of the ridged-horn in transmitting mode is verified by transmission and reception of a UWB signal.

CHAPTER 3

ANTENNA NOISE EFFECT ON UWB ANGLE ESTIMATION

3.1 Introduction

In ultra-wideband (UWB) radio systems, the time-difference-of-arrival (TDOA) method [24]−[27] can be used to find the location of a radar target or a transponder. To do so, we need to estimate the range and the angle-of-arrival of the incident signal that is either reflected from the radar target, or transmitted from the transponder. In the TDOA method, the range information is estimated from the received signal's time-of-arrival, while the angle-of-arrival information is estimated from the difference in time-of-arrivals recorded by the receivers of the TDOA array. The TDOA method is more suitable for UWB than conventional narrowband radio systems. This is because, unlike narrowband radio systems, UWB transmits and receives signals of short electrical lengths. The TDOA method can leverage on the inherently short electrical lengths of UWB signals in free-space (6 to 15 cm for a UWB pulse of typical pulse width 0.2 to 0.5 ns) to locate the radar target or transponder with better accuracy.

The TDOA receiver array, as its name suggests, consists of an array of receivers that estimate the time-of-arrivals of the received signal, and then feed the time-of-arrival information to the TDOA processor. To find the range, the TDOA processor calculates the average time-of-arrival from the receivers, and then calculates the range by considering the absolute delay of the signal (from a reference time) and the speed of light. To estimate the angle-of-arrival, the TDOA processor finds the relative difference in the time-of-arrivals and calculates the angle by considering these differences and the locations of the receivers. However, in our initial measurements, the TDOA receiver can only achieve limited accuracy. The limitation in accuracy is attributed to low signal-to-noise ratios (SNR) of the received signal. Low SNR compromises the accuracy of the time-of-arrival, which leads to inaccuracies in estimating the angle-of-arrival, since the angle is calculated from the time-of-arrival.

In this chapter, we propose a model that predicts the TDOA accuracy. The proposed model considers several factors such as the incident signal, the antenna noise [10] and signal distortions due to the receiving antennas. It models the TDOA accuracy as a probability density function. The root mean square of the probability density functions are then verified by experiments. In Sections 3.2 and 3.3, we derive the time-of-arrival accuracy of the received signal and express it as probability density function. In Section 3.4, we derive the angle-of-arrival accuracy based on the result in Section 3.3. In Section 3.5, we experimentally verify the time-of-arrival derivations in Sections 3.2 and 3.3. Lastly, in Sections 3.6 and 3.7, we verify the angle-of-arrival derivations in Section 3.4 by numerical simulation and experiments.

3.2 Time-of-Arrival Estimation of UWB Signals at Boresight

In this section, we will derive the probability density function for the estimated time-of-arrival of UWB signals in boresight. Here, we will first describe the UWB cross-correlation receiver and show how it is used in estimating the time-of-arrival of a received signal. Then, after stating the assumptions we make on the received signal, we will derive the probability density function.

Figure 3.1 shows the stored reference (SR) cross-correlation receiver [67] that is used to estimate the UWB signal's time-of-arrival. Let a UWB signal, $e(t)$, be incident on the receiving antenna from boresight. Because the receiving antenna does not distort the signal that arrives in boresight direction, the received signal appears as $r(t - \tau_0)$, which has the same shape as the incident signal, $e(t)$. However, the received signal is corrupted by antenna noise $n(t)$ [14]. The antenna noise corrupted signal, $r(t - \tau_0) + n(t)$, is cross-correlated with a reference signal, $r_0(t - \tau)$, which is generated by the receiver. In this section, we assume that the shape of $r\ (t - \tau_0)$ is known and it is used as the reference signal of the cross-correlator circuit. The received signal's time-of-arrival, however, is still unknown, and will be estimated by the receiver.

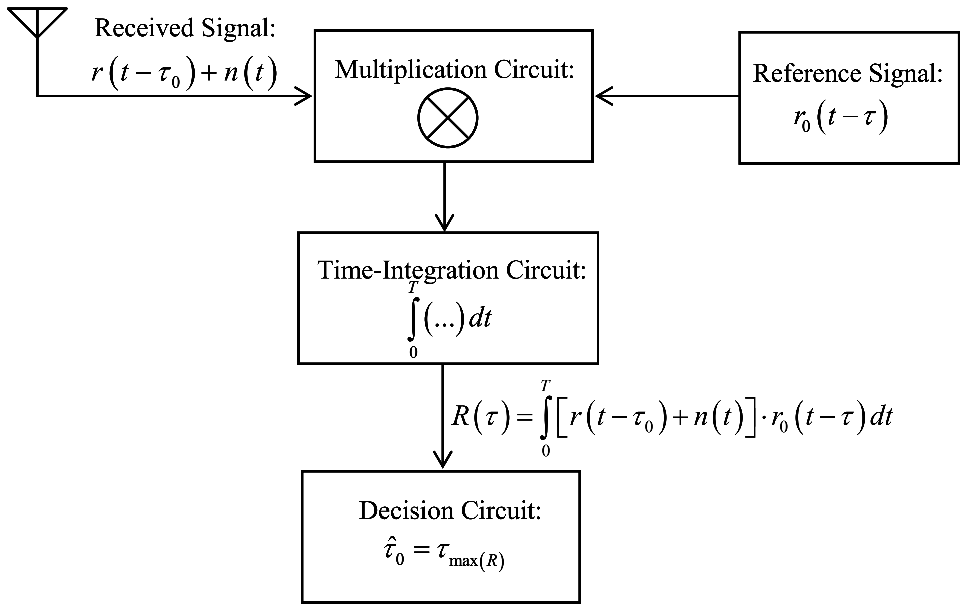

Figure 3.1: Schematic of a stored reference cross-correlation receiver estimating the time-of-arrival of a received signal.

As shown in Figure 3.1, the cross-correlation receiver consists of a multiplication circuit, a time integration circuit, a reference signal generator circuit and a decision circuit. The multiplication circuit can be implemented with a diode mixer or a Gilbert cell multiplier. The time integration circuit can be implemented by low-pass filters. The reference signal generator circuit can be implemented by a pulse-forming network [59]. The pulse forming network is triggered by a step or clock signal whose delay, τ, can be controlled. The decision circuit is used to estimate the time-of-arrival of the received signal. To do so, it collects the cross-correlated values, $R\ (\tau = \tau_i)$, of the received and reference signals once every pulse repetition interval (PRI) and stores them. τ_i refers to the reference signal's delay, τ, at the i-th interval. At every PRI, τ_i is increased with a time resolution of Δt s from 0 s to T s. Because of the gradual increment of τ_i, after $T\ /\ \Delta t$ number of PRIs, a cross-correlation signal $R\ (\tau)$ will be formed. Once a complete set of R (τ) is known, the decision circuit makes a decision that the estimated time-of-arrival lies at the instance of maximum cross-correlation. This process is then repeated to find the next time-or-arrival.

As mentioned earlier, the signal present at the cross-correlator input is an antenna noise corrupted signal. In the following analysis, it is assumed that the antenna noise behaves as an additive white Gaussian noise (AWGN), with mean noise power per unit bandwidth of N_0. N_0 is related to the antenna temperature, T_{ant} [14], as $N_0 = k_B\, T_{ant}$, where k_B is the Boltzmann's constant. The value of N_0 can be obtained from n (t) [10], [14] as

$$N_0 = \frac{\Delta t}{T}\int_0^T \left|n\left(t\right)\right|^2 dt \cong \frac{\Delta t}{T}\cdot \Delta t \sum_{i=1}^{T/\Delta t} n_i^{\,2} \tag{3.1}$$

where n (t) is the measured antenna noise signal, Δt is the time resolution and T is the time-interval of measured antenna noise signal, n (t). In the following analysis, it is assumed that the signal-to-noise ratio is large, *i.e.* E_b / N_0 >> 1 [10], where E_b is defined as the energy of the received UWB signal in one PRI,

$$E_b = \int_0^T \left|r\left(t-\tau_0\right)\right|^2 dt \cong \Delta t \sum_{i=1}^{T/\Delta t} r_i^2 \tag{3.2}$$

Reference [10] has shown that, in general, the probability density function for the estimated time-of-arrival of a received signal, $\hat{\tau}$, based on the stored-reference cross-correlation receiver shown in Figure 3.1, is

$$\hat{\tau} \sim N\left(\tau_0, \quad \frac{N_0}{E_b \beta_s^{\,2}}\right) \tag{3.3}$$

where τ_0 is the true time-of-arrival, N_0 is the antenna noise power and E_b is the energy of the received pulse within one PRI. β_s is the received signal's second moment [7] defined as

$$E_b \cdot \beta_s^{\,2} = \int_{-\infty}^{\infty} r(t) \cdot \frac{d^2}{dt^2} r(t)\, dt \tag{3.4}$$

Hence, from the probability density function of (3.3), the root mean square error (standard deviation) of the estimated time-of-arrival of UWB signal is $\frac{1}{\beta_s}\sqrt{\frac{N_0}{E_b}}$.

3.3 Time-of-Arrival Estimation of UWB Signals at Off-boresight

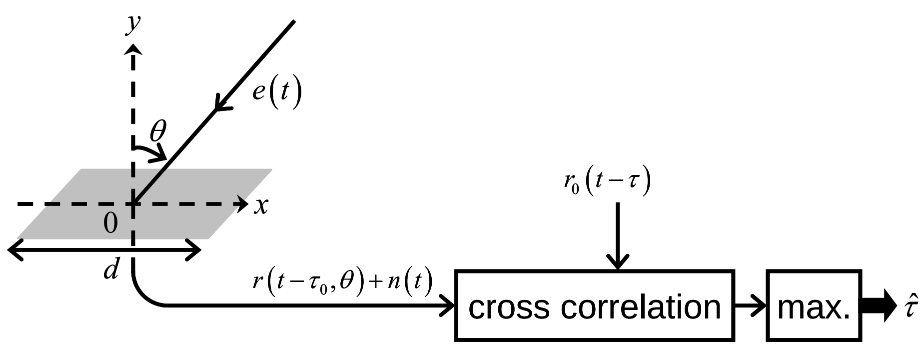

Figure 3.2: A UWB cross-correlation receiver.

In this section, we will derive the probability density function of the estimated time-of-arrival of UWB signals at off-boresight angles. The receiver used to estimate the time-of-arrival is the same cross-correlation receiver, as shown in Figure 3.2. Let the receiving antenna be the double-ridged horn by RCM Ltd. (model MDRH-1018) shown in Figure 2.2. The azimuth plane impulse response of the antenna in receiving mode can be derived as

$$f_r\left(t,\theta,\phi=0^\circ\right)=\frac{k}{\sin\theta}\cos^{12}\left(\frac{\pi ct}{\alpha\sin\theta}\right)\cdot\left[u\left(t+\frac{\tau_\alpha}{2}\right)-u\left(t-\frac{\tau_\alpha}{2}\right)\right] \tag{3.5}$$

where $u\ (t)$ is a unit step function, k is an proportionality constant, $\tau_\alpha = \alpha \sin\theta / c$ and α is the width of the ridged-horn aperture. $e\ (t)$, the incident UWB signal, has been defined in (2.15) as a second derivative Gaussian pulse with τ_e = 60 ps. The received signal is expressed as

$$r_n\left(t\right)=e\left(t-\tau_0\right)\otimes f_r\left(t,\theta,\phi=0^\circ\right)+n\left(t\right)=r\left(t-\tau_0,\theta\right)+n\left(t\right) \tag{3.6}$$

Based on the analysis provided in [10], the likelihood function of estimated time-of-arrival of the signal (3.6), when received with a stored reference cross-correlation receiver, is

$$P\left(\tau\right)\cong\exp\left[\frac{1}{N_0}\int_0^T r_n\left(t\right)r_0\left(t-\tau\right)dt\right]=\exp\left[v\left(\tau,\theta\right)+w\left(\tau\right)\right] \tag{3.7}$$

where

$$v\left(\tau,\theta\right)=\frac{1}{N_0}\int_0^T\left[e\left(t-\tau_0\right)\otimes f_r\left(t,\theta\right)\right]\cdot r_0\left(t-\tau\right)dt \tag{3.8}$$

$$w\left(\tau\right)=\frac{1}{N_0}\int_0^T n\left(t\right)r_0\left(t-\tau\right)dt \tag{3.9}$$

and $r_0\ (t)$ is the reference signal of the cross-correlation receiver. $r_0\ (t)$ is chosen to have the same shape as the received UWB signal at boresight direction ($\varphi = \theta = 0°$),

$$r_0\left(t\right)=e\left(t\right)\otimes f_r\left(t,\phi=\theta=0^\circ\right) \tag{3.10}$$

Functions v and w will be called the signal function and the noise function respectively. It can be observed that the signal function, $v(\tau, \theta)$, is maximum when $\tau = \tau_0$ and $\theta = \theta_{max} = 0°$,

$$v_{\max} = v\left(\tau = \tau_0, \theta = 0°\right) = \frac{E_b}{N_0} \tag{3.11}$$

The variance of the noise function, $w(\tau)$, can be found by sampling analysis. Taking an arbitrarily small value of Δt as the lower sampling time limit, equation (3.9) can be rewritten as

$$w = \frac{\Delta t}{N_0} \sum_{i=1}^{T/\Delta t} n_i r_{0i} \tag{3.12}$$

where r_{0i} are samples of $r(t - \tau)$, and each sample of n_i has a variance of $N_0 / \Delta t$. Since all n_i samples are statistically independent, the total variance is the sum of the variances of each sample,

$$\overline{w}^2 = \frac{\left(\Delta t\right)^2}{N_0^{\,2}} \sum_{i=1}^{T/\Delta t} \frac{N_0}{\Delta t} r_{0i}^{\,2} = \frac{E_b}{N_0} \tag{3.13}$$

It can be observed from (3.11) and (3.13) that the maximum value of signal function is equal to the mean square value of the noise function, which is also proportional to the signal-to-noise ratio (SNR) of the received UWB signal. When $E_b / N_0 \leq 1$, the contribution from the noise function to the probability density function $P(\tau)$ of (3.7) is equal or more than that of the signal function. However, when $E_b / N_0 >> 1$, the contribution from the noise function becomes insignificant compared to the signal function. Hence, by confining our attention to cases where $E_b / N_0 >> 1$, the contribution from the noise function can be neglected, and $P(\tau)$ can be approximated as

$$P(\tau) \cong \exp\left[v(\tau,\theta)\right] = \exp\left\{\frac{1}{N_0}\int_0^T \left[e(t-\tau_0)\otimes f_r(t,\theta)\right]\cdot r_0(t-\tau)\,dt\right\} \tag{3.14}$$

To further simplify the likelihood function, let $v(\tau, \theta)$ in (3.14) be expanded about τ_0 by Taylor's theorem, resulting in

$$P(\tau) \cong \exp\left\{\frac{E_b(\theta)}{N_0}\left[1-\frac{1}{2}\beta_s^2(\theta)(\tau-\tau_0)^2+\ldots\right]\right\} \propto \exp\left\{\frac{1}{2}\frac{(\tau-\tau_0)^2}{N_0\big/\left[2E_b(\theta)\beta_s^2(\theta)\right]}\right\} \tag{3.15}$$

where

$$E_b(\theta) = \int_0^T \left[e(t-\tau_0)\otimes f_r(t,\theta)\right]\cdot r_0(t-\tau)\,dt \tag{3.16}$$

$$E_b(\theta)\beta_s^2(\theta) = \int_0^T \left[e(t-\tau_0)\otimes f_r(t,\theta)\right]\cdot \frac{d^2}{dt^2}\left[r_0(t-\tau)\right]dt \tag{3.17}$$

Equation (3.15) shows that the estimated time-of-arrival is a Gaussian probability density function

$$\hat{\tau} \sim N\left[\tau_0, \frac{N_0}{E_b(\theta)\beta_s^2(\theta)}\right] \tag{3.18}$$

Hence, from the variance expression of (3.18), we can derive the root mean square error of the estimated time-of-arrival of UWB signal as

$$\sigma_\tau(\theta) = \frac{1}{\beta_s(\theta)}\sqrt{\frac{N_0}{E_b(\theta)}} \tag{3.19}$$

3.4 Angle-of-Arrival Estimation of UWB TDOA Receivers

In this section, we will derive the probability density function of the estimated angle-of-arrival by the UWB TDOA receiver array. To do that, we will first describe the TDOA array and how the TDOA processor estimates the angle-of-arrival. Then, the TDOA array will be modeled to derive the angle-of-arrival accuracy.

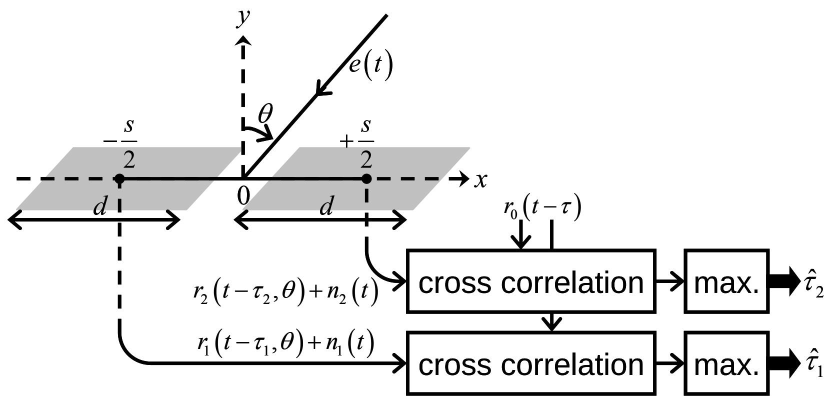

Figure 3.3: A UWB Time-difference-of-arrival (TDOA) receiver array.

Figure 3.3 shows a UWB TDOA array of two receivers. Each receiver captures the incident signal, $e(t)$, with a ridged-horn. The ridged-horn is connected to a stored-reference cross-correlator receiver that has been described in Section 3.2. The ridged-horn of the left receiver (Figure 3.3) is labeled as RH1, while the ridged-horn of the right receiver (Figure 3.3) is labeled as RH2. Both RH1 and RH2 have the same aperture length of $d = 0.236$ m. Modeling of this TDOA receiver will only be done for the azimuth plane.

Let the received UWB signals of RH1 and RH2 be $r_1(t-\tau_1, \theta)$ and $r_2(t-\tau_2, \theta)$ respectively. θ is the angle-of-arrival of the transmitted signal incident on the TDOA receiver; while τ_1 and τ_2 are the true time-of-arrivals of the received UWB signals from receivers RH1 and RH2. In the receivers, r_1 and r_2 are cross-correlated with the reference signal r_0 (3.10). The process of estimating the time-of-arrivals of r_1 and r_2 is similar to that described in Section 3.2. The impulse responses of the antennas RH1 and RH2 in receiving mode are f_{r1} $(t, \theta, \varphi = 0°)$ and f_{r2} $(t, \theta, \varphi = 0°)$ respectively, where

$$f_{r1}\left(t,\theta,\phi=0°\right)=\frac{1}{\sin\theta}\cos^{12}\left[\frac{c\pi}{d\sin\theta}\left(t-\frac{s\sin\theta}{2c}\right)\right]\cdot\left\{u\left[t-\frac{\left(s+d\right)\sin\theta}{2c}\right]-u\left[t-\frac{\left(s-d\right)\sin\theta}{2c}\right]\right\} \quad (3.20)$$

$$f_{r2}\left(t,\theta,\phi=0°\right)=\frac{1}{\sin\theta}\cos^{12}\left[\frac{c\pi}{d\sin\theta}\left(t+\frac{s\sin\theta}{2c}\right)\right]\cdot\left\{u\left[t+\frac{\left(s-d\right)\sin\theta}{2c}\right]-u\left[t-\frac{\left(s+d\right)\sin\theta}{2c}\right]\right\} \quad (3.21)$$

Let $\hat{\tau}_1$ and $\hat{\tau}_2$ be the estimated time-of-arrivals of the received signals from receivers RH1 and RH2 respectively. Applying the same analysis that derived (3.18) in Section 3.3, we can derive the probability density function of $\hat{\tau}_1$ and $\hat{\tau}_2$ as

$$\hat{\tau}_1 \sim N\left[\tau_1,\frac{N_1}{E_b\left(\theta\right)\beta^2\left(\theta\right)}\right] \quad (3.22)$$

$$\hat{\tau}_2 \sim N\left[\tau_2,\frac{N_2}{E_b\left(\theta\right)\beta^2\left(\theta\right)}\right] \quad (3.23)$$

It can be observed from the relative positions of the receivers RH1 and RH2, in Figure 3.3, that the estimated angle-of-arrival, $\hat{\theta}$, is related to $\hat{\tau}_1$ and $\hat{\tau}_2$ as

$$\sin\hat{\theta}=\frac{c}{s}\left(\hat{\tau}_2-\hat{\tau}_1\right) \quad (3.24)$$

where c is the speed of light in free space and s is the separation between the antennas. Substituting the probability density functions of $\hat{\tau}_1$ and $\hat{\tau}_2$ into (3.24), the probability density function of $\sin\hat{\theta}$ can be derived as

$$\sin\hat{\theta} \sim N\left[\sin\theta, \quad \frac{c^2\left(N_1+N_2\right)}{s^2\beta^2\left(\theta\right)E\left(\theta\right)}\right] \tag{3.25}$$

However, for (3.25) to be valid, values assumed by $\sin\hat{\theta}$ must be contained within [-1, 1]. Values beyond [-1, 1] have to be discarded because they do not translate into a valid $\hat{\theta}$ value. Hence, the probability density function of (3.25) has to be doubly-truncated [68] at [-1, 1] to

$$P_{DTN}\left(\sin\hat{\theta}\right) = \begin{cases} 0 & , \quad -\infty \le \sin\hat{\theta} \le -1 \\ \dfrac{P\left(\sin\hat{\theta}\right)}{\int_{-1}^{1} P\left(\sin\hat{\theta}\right) d\sin\hat{\theta}} & , \quad -1 \le \sin\hat{\theta} \le +1 \\ 0 & , \quad +1 \le \sin\hat{\theta} \le +\infty \end{cases} \tag{3.26}$$

Double truncation also results in inaccurate angle-of-arrival predictions at the angles near ±90°. This inaccuracy is acceptable since most angle-of-arrival estimations are done within the 3-dB beamwidth of the receiver antennas, which is far away from ±90°. Probability density function of $\hat{\theta}$ can be calculated from probability density function of doubly-truncated $\sin\hat{\theta}$ by a one-to-one mapping method of a random variable function [69] as

$$P_{DTN}\left(\hat{\theta}\right) = \begin{cases} 0 & , \quad -\infty \le \hat{\theta} \le -90^\circ \\ \dfrac{\cos\hat{\theta}}{k\sqrt{2\pi}\sigma}\exp\left[-\dfrac{1}{2}\left(\dfrac{\sin\hat{\theta}-\sin\theta}{\sigma}\right)^2\right] & , \quad -90^\circ \le \hat{\theta} \le +90^\circ \\ 0 & , \quad +90^\circ \le \hat{\theta} \le +\infty \end{cases} \tag{3.27}$$

where θ is only defined within [−90°, 90°], and

$$k = \int_{-1}^{1} P\left(\sin\hat{\theta}\right) d\sin\hat{\theta} = \int_{-1}^{1} \frac{1}{\sqrt{2\pi}\sigma} \exp\left[-\frac{1}{2}\left(\frac{\sin\hat{\theta} - \sin\theta}{\sigma}\right)^2\right] d\sin\hat{\theta} \tag{3.28}$$

$$\sigma^2 = \frac{c^2\left(N_1 + N_2\right)}{s^2\beta^2\left(\theta\right)E\left(\theta\right)} \tag{3.29}$$

The theoretical variance of $\hat{\theta}$ can be expressed as

$$\sigma_{\hat{\theta}}^{\ 2} = \int_{-90}^{90} \left(\hat{\theta} - \mu_{\hat{\theta}}\right)^2 \frac{\cos\hat{\theta}}{k\sqrt{2\pi}\sigma} \exp\left[-\frac{1}{2}\left(\frac{\sin\hat{\theta} - \sin\theta}{\sigma}\right)^2\right] d\hat{\theta} \tag{3.30}$$

where

$$\mu_{\hat{\theta}} = \int_{-90}^{90} \frac{\hat{\theta}\cos\hat{\theta}}{k\sqrt{2\pi}\sigma} \exp\left[-\frac{1}{2}\left(\frac{\sin\hat{\theta} - \sin\theta}{\sigma}\right)^2\right] d\hat{\theta} \tag{3.31}$$

Hence, the theoretical root mean square error (standard deviation) of angle-of-arrival, $\hat{\theta}$, for an arbitrary SNR can be calculated numerically from (3.30).

3.5 Verification of Time-of-Arrival Derivations

In Sections 3.2 and 3.3, the time-of-arrival accuracy has been derived for the case of a radiated UWB signal incident on a ridged-horn antenna. The derived accuracy, expressed in root-mean-square error, will be experimentally verified in this section. In the experiment, a UWB source is placed at far-field distance and radiates a train of UWB pulses. The amplitude of the radiated signal can be adjusted, by adding attenuators, so that different signal-to-noise ratios (SNR) can be achieved at the receiver. The radiated UWB signal is received by a ridged-horn antenna, and measured with a 40 GS/s sampling oscilloscope. During the measurement, no averaging is applied to the measured signal in the sampling oscilloscope. The receiving ridged-horn antenna is placed on a turn-table, which rotates in the azimuth plane from θ = -20° to 20°, at 1° intervals. In each interval, 50 samples of received signals are collected. The measurements are done at both antennas RH1 and RH2. Furthermore, the collection of received signals is repeated for three different UWB source amplitudes.

During the measurements, it is observed that receiving antennas RH1 and RH2 introduce different power levels of antenna noise to the received signal. Hence, by using both the antennas to receive radiated UWB signal at three different power levels, the received signal data for six cases of signal-to-noise ratios (SNR) can be analyzed.

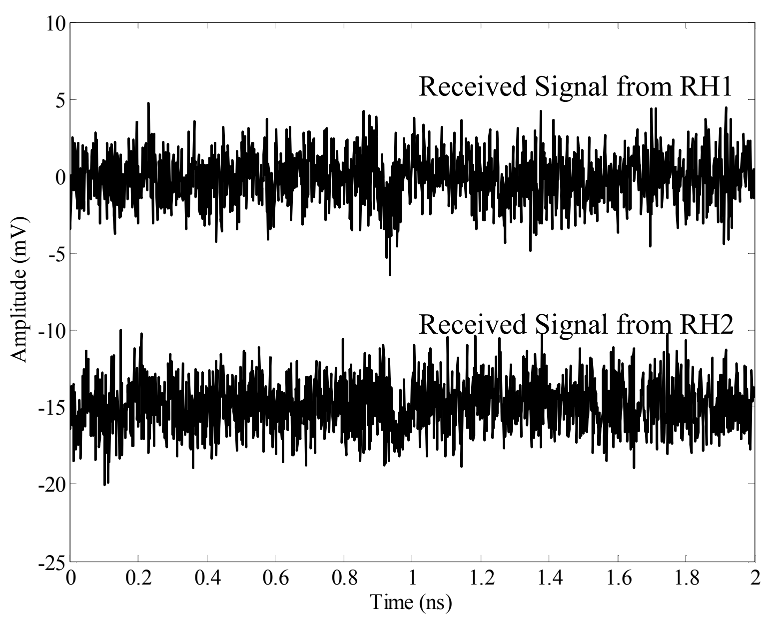

Figure 3.4: A sample of measured received signal with antennas RH1 and RH2.

Figure 3.4 shows a sample of the measured signal with antennas RH1 and RH2 at boresight. It can be seen from both traces that the received signal is corrupted with thermal noise, making it difficult to judge the true time-of-arrival. These measured signals are cross-correlated with the reference signal r_0 (3.10), and the instance of maximum cross-correlation is recorded as estimated time-of-arrivals. From the measured samples, the root mean square error can be found and compared with the derived root mean square error in (3.3) and (3.18).

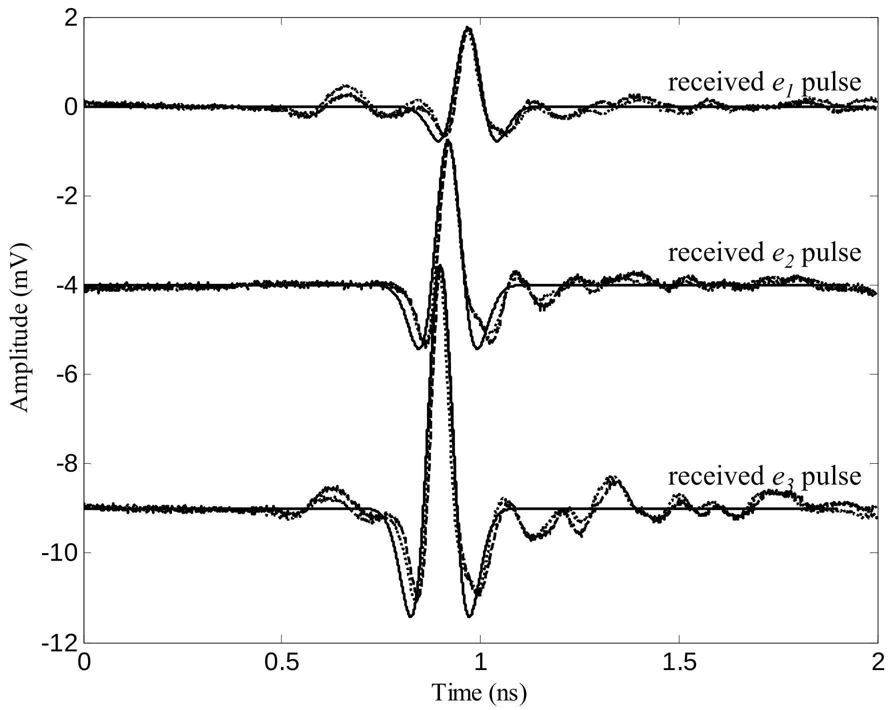

Figure 3.5: Measured received signal with antennas RH1 (dotted line) and RH2 (dashed line) compared to the modeled received signal (line) in three power levels.

To find the value of $E_b(\theta)$, we need to measure the received signal without noise corruption. To do that, the noise corrupted received signal is averaged 4096 times so that antenna noise corruption is suppressed. The dotted and dashed lines in Figure 3.5 are the measured received signals of three power levels – labeled as e_1, e_2 and e_3. The dotted line corresponds to antenna RH1 and the dashed line corresponds to antenna RH2. Let the energies of an e_1, e_2 and e_3 pulse be E_{b1}, E_{b2} and E_{b3}

respectively. By numerically integrating the e_1, e_2 and e_3 signals in Figure 3.5, it can be found that E_{b1} = 1.6e-16 J; E_{b2} = 5.0e-16 J; and E_{b3} = 1.4e-15 J. Furthermore, e_1, e_2 and e_3 are modeled as second derivative Gaussian pulses (2.15), as shown in the line trace of Figure 3.5 – e_1 is modeled with A = 1.75 mV and τ_p = 60.0 ps; e_2 is modeled with A = 3.22 mV and τ_p = 60.0 ps; While e_3 is modeled with A = 5.43 mV and τ_p = 60.0 ps.

Mean antenna noise power per unit bandwidth, N_0, can be calculated from measured n (t), according to (3.1). To measure n (t), the antenna output signal is measured without the presence of a UWB source signal. Measurements of n (t) are performed at the same conditions as the time-of-arrival measurements, and just before the measurements. Twenty sets of n (t) are measured, and N_0 is calculated for all the twenty measurements. A consistency check on the N_0 values shows negligible deviations.

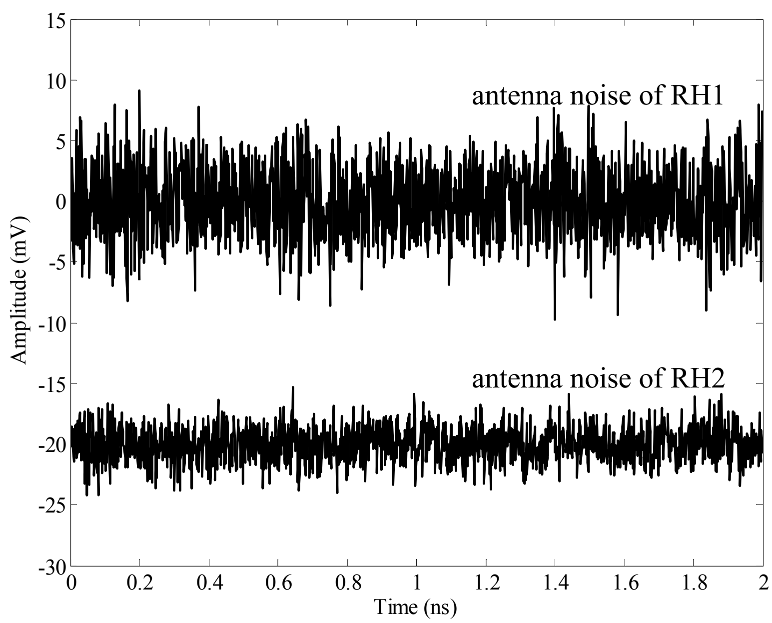

Figure 3.6: A sample of measured noise signal of antennas RH1 and RH2.

Figure 3.6 shows a sample of n (t) from RH1 and RH2. It can be seen that the antenna noise power for RH1 and RH2 are different, despite the fact that RH1 and RH2 are a matched pair of ridged-horns. This difference is attributed to errors in fabrication and mechanical tolerances of the ridged-horn. The measured value of antenna noise for RH1 is N_1 = 12.3e-18 J and RH2 is N_2 = 2.7e-18 J. From (3.17), β_s^2 value can be numerically calculated for all the relevant angles. From the measured values of E_{b1} (θ), E_{b2} (θ), E_{b3} (θ), N_1 and N_2, the theoretical standard deviation (root mean square error) can be calculated, and compared with the measured root mean square error. The comparisons at boresight, ±10° and ±20° are shown in Tables 3.1, 3.2 and 3.3 respectively.

No.	SNR	E_b / N_0 (dB)	s.d. (theoretical)	s.d. (measured)
1.	E_{b1} / N_1	11.1	7.44 ps	10.857 ps
2.	E_{b2} / N_1	16.1	4.21 ps	4.591 ps
3.	E_{b1} / N_2	17.7	3.49 ps	6.083 ps
4.	E_{b3} / N_1	21.3	2.52 ps	1.612 ps
5.	E_{b2} / N_2	22.7	1.97 ps	2.057 ps
6.	E_{b3} / N_2	27.1	1.179 ps	1.535 ps

Table 3.1: Theoretical and experimental time-of-arrival standard deviation at boresight for six cases of SNR.

No.	*SNR*	E_b / N_0 (dB)	s.d. (theoretical)	s.d. (-ve) measured	s.d. (+ve) measured
1.	E_{b1}/N_1	10.1	8.58 ps	6.00 ps	5.45 ps
2.	E_{b2}/N_1	15.4	4.66 ps	14.29 ps	5.82 ps
3.	E_{b1}/N_2	16.7	4.02 ps	4.97 ps	3.30 ps
4.	E_{b3}/N_1	19.9	2.76 ps	2.82 ps	2.20 ps
5.	E_{b2}/N_2	22.0	2.18 ps	5.27 ps	3.06 ps
6.	E_{b3}/N_2	26.5	1.29 ps	1.72 ps	1.07 ps

Table 3.2: Theoretical and experimental time-of-arrival standard deviation at ± 10° for six cases of SNR.

No	*SNR*	E_b / N_0 (dB)	s.d. (theoretical)	s.d. (-ve) measured	s.d. (+ve) measured
1.	E_{b1} / N_1	7.9	11.59 ps	6.49 ps	12.57 ps
2.	E_{b2} / N_1	13.2	6.29 ps	8.68 ps	9.14 ps
3.	E_{b1} / N_2	14.5	5.43 ps	3.43 ps	4.22 ps
4.	E_{b3} / N_1	17.8	3.73 ps	3.14 ps	3.57 ps
5.	E_{b2} / N_2	19.8	2.95 ps	2.39 ps	5.64 ps
6.	E_{b3} / N_2	24.4	1.75 ps	1.62 ps	1.85 ps

Table 3.3: Theoretical and experimental time-of-arrival standard deviation at ± 20° for six cases of

Comparison between theoretical and measured standard deviations shows that there is good agreement between the two values.

3.6 Numerical Simulation of Angle-of-Arrival

In this section, the theoretical standard deviation (root mean square error) calculated from (3.30) will be verified by simulation. To make sure that the simulated values of angle-of-arrival accuracy can be effectively compared with the theoretical and measured values, the simulation need to be done in conditions that are similar to the measurement. In the measurement, received signals in three power levels are measured. The energies of the received UWB signals are: E_{b1} = 1.6e−16 J; E_{b2} = 5.0e−16 J; and E_{b3} = 1.4e−15 J. As mentioned in the last section, the measured antenna noise power per unit bandwidth of RH1 and RH2 are N_1 = 12.3e−18 J and RH2 is N_2 = 2.7e−18 J respectively.

Based on these values, the theoretical standard deviation (3.30) has been calculated, and presented in Figure 3.7. In Figure 3.7, Case 1 refers to the situation where the received UWB signal has the energy of E_{b1} in a pulse repetition interval (PRI); Case 2 refers to the situation where the received UWB signal has the energy of E_{b2} in a PRI; and Case 3 refers to the situation where the received UWB signal has the energy of E_{b3} in a PRI. For all the Cases 1-3, the receiving antennas are RH1 and RH2 with antenna noise of N_1 and N_2 respectively.

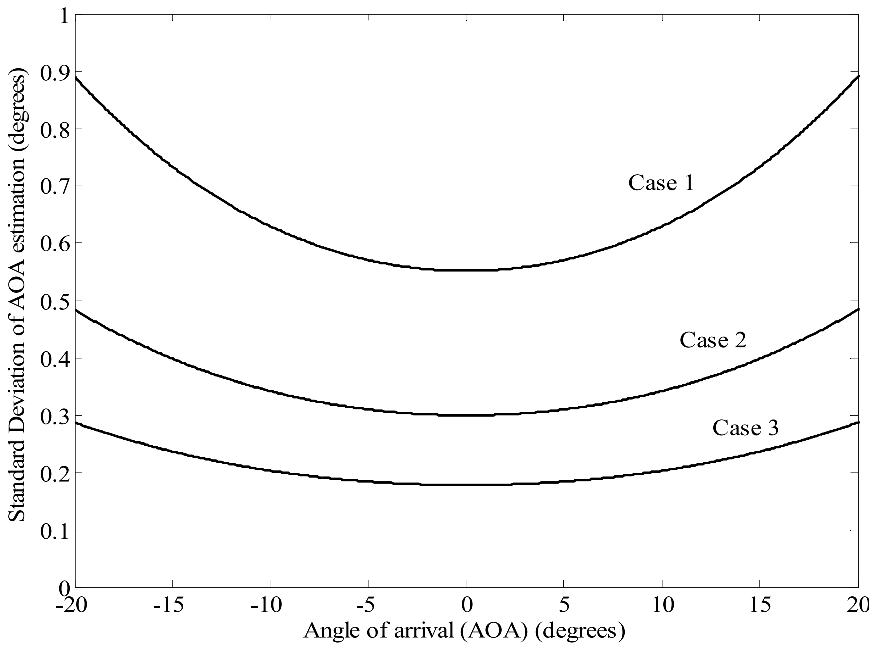

Figure 3.7: Theoretical standard deviations of estimated angle-of-arrival (AOA) for three cases of signal-to-noise ratio (SNR).

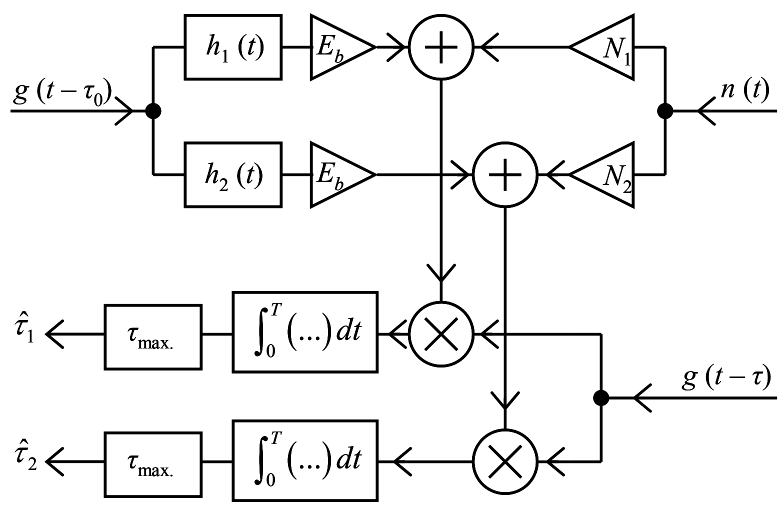

Figure 3.8: Schematic of simulation process to verify the TDOA receiver's angle-of-arrival accuracy.

The simulation is performed in MATLAB – a mathematical software. In the simulation, the received UWB signals are generated by convolution of (2.15) and (3.5), and are scaled according to the energy levels of E_{b1}, E_{b2} and E_{b3}. The antenna noise is generated by an existing AWGN noise signal generator in MATLAB. The antenna noise power is scaled according to N_1 and N_2, and then added to the received UWB signal to simulate the noise corrupted received signal. This signal is then cross-correlated with a 1 V amplitude reference signal, which is generated as defined in (3.10). The instances of maximum cross-correlation for both receivers are found, and substituted into equation (3.24) to calculate the estimated angle-of-arrival for one sample of data. Diagrammatically, the simulation process is shown in Figure 3.8.

For every angle, 200 samples of angle-of-arrival data are collected based on the simulation as described by Figure 3.8. The standard deviations from the simulations are tabulated and shown in Figure 3.9.

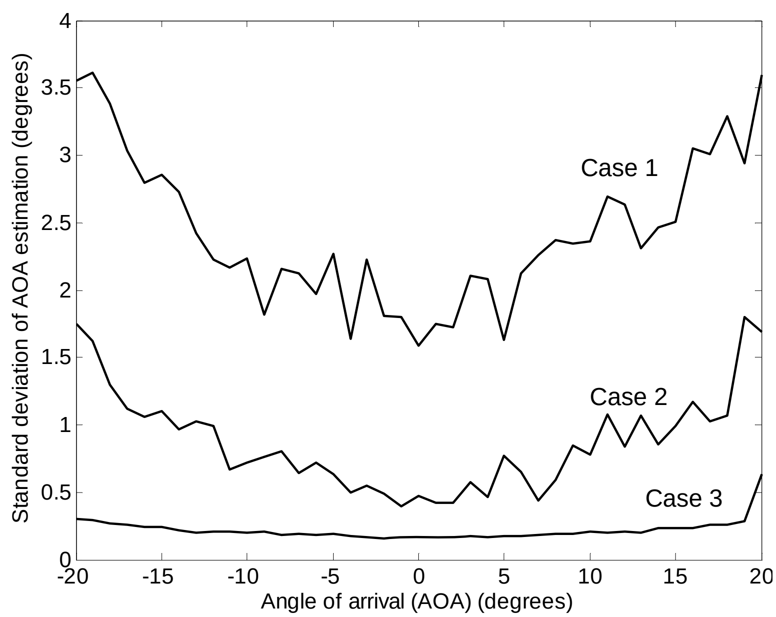

Figure 3.9: Simulated standard deviations of estimated angle-of-arrival (AOA) for three cases of signal-to-noise ratio (SNR).

3.7 Measurement of Angle-of-Arrival

In this section, the theoretical standard deviation (root mean square error) calculated from (3.30) will be verified by measurements. Figure 3.10 shows the measurement setup. In the measurement, the UWB TDOA receiver array, consisting of two double ridged-horns by RCM Ltd. (model MDRH-1018), are placed on a turn-table. The ridge-horns RH1 and RH2 are placed at a distance $s = 0.263$ m apart, with their aperture length $d = 0.236$ m. The turn-table is rotated, at 1° intervals, from −20° to 20°. The time domain signals are measured by a time-synchronized 40 GS/s sampling oscilloscope. To synchronize the pulse generator at the transmitter and the sampling oscilloscope, a 6.0 m coaxial cable is connected from the trigger signal of the pulse generator to the trigger input of the sampling oscilloscope.

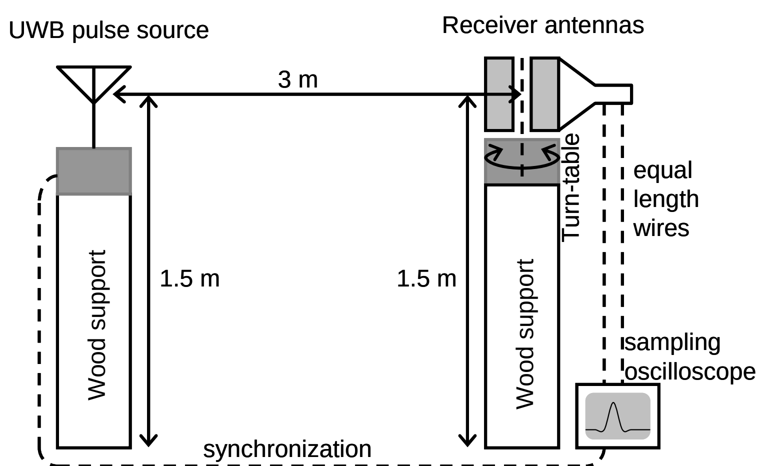

Figure 3.10: Angle-of-Arrival measurement setup.

Figure 3.11 shows a photograph of the setup during one of the angle-of-arrival measurements. The incident UWB pulse is radiated by an antenna placed at far-field distance. 50 samples of signals are measured (at both receivers) for every 1° rotation. The wooden turn-table seen in Figure 3.11 is constructed by bolting two circular boards together in alignment. To achieve measurements of 1°

accuracy, a Vernier scale is used – the lower circular board is marked at 10° intervals, while the upper circular board is marked at 11° intervals. The antennas are directly connected to the sampling oscilloscope with two equal length coaxial cables, as shown in Figure 3.11. The measured signals are then cross-correlated with the reference signal to obtain samples of measured angle-of-arrivals.

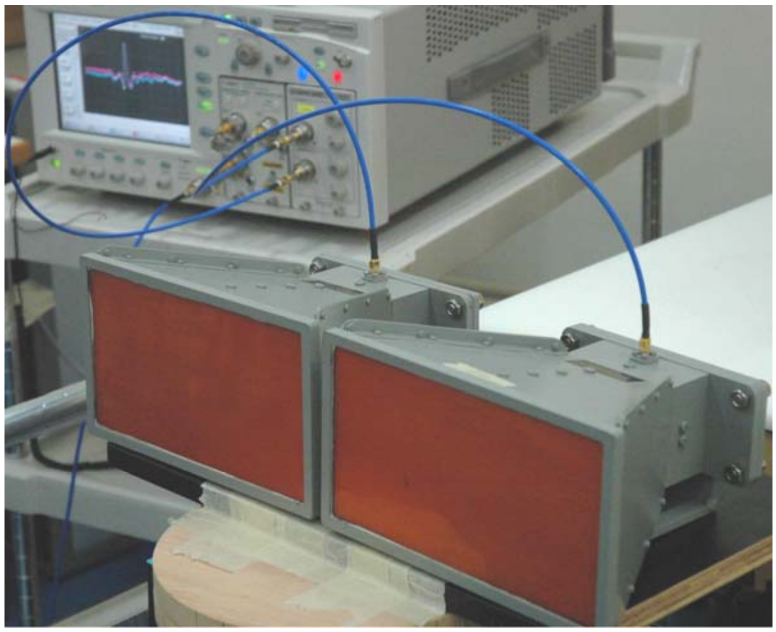

Figure 3.11: Picture of Angle-of-Arrival measurement setup.

A sample of measured waveform is shown in Figure 3.12, where received signals from antennas 1 and 2 are plotted with their respective cross-correlation outputs for Case 2 SNR at $\theta = +10°$. For the case in Figure 3.12, $\hat{\tau}_1 = 0.85$ ns and $\hat{\tau}_2 = 1.03$ ns, giving an angle-of-arrival reading of +11.8°, which is slightly off from $\theta = +10°$.

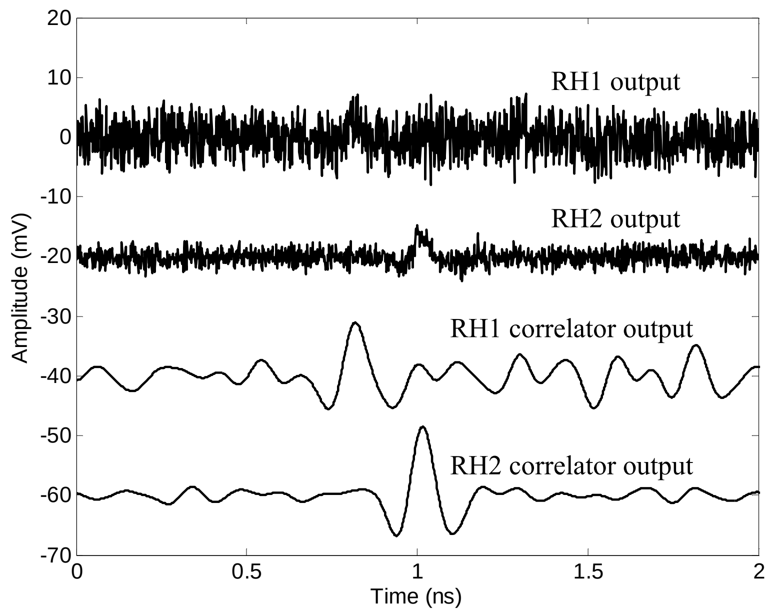

Figure 3.12: Measured received signals and correlator outputs for antennas RH1 and RH2 at $\theta = +10°$, Case 2 SNR.

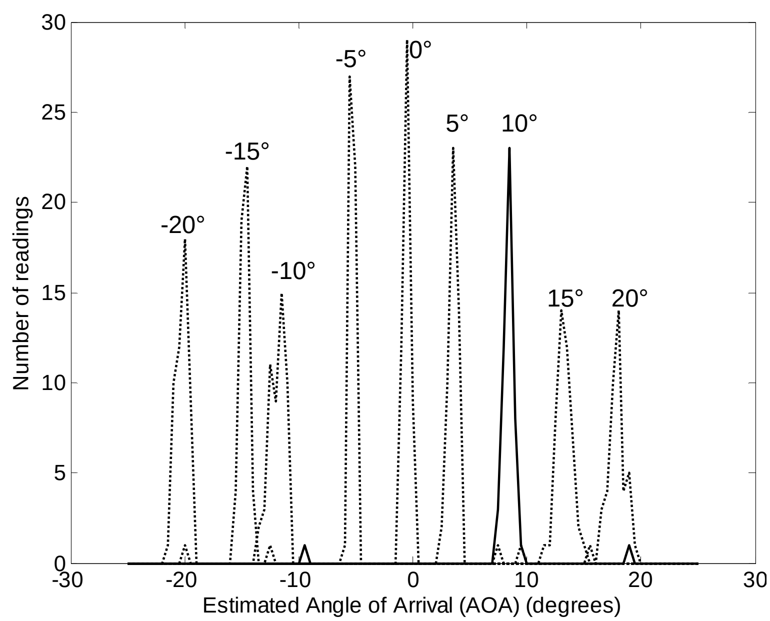

Figure 3.13: Distribution of measured Angle-of-Arrival (AOA) for $\theta = 10°$ (line) and other angles (dotted lines).

Figure 3.13 shows the distribution of measured angle versus true angle for experiments based on Case 2. Figure 3.13 shows that the measured angles follow the Gaussian-like distribution centered at their true angles. At boresight (Figure 3.13 – ‘0°’), the Gaussian-like distribution has the smallest standard deviation. As the target angle moves away from boresight, the standard deviation increases as predicted. The solid line in Figure 3.13 shows the measured angles at a true angle of +10°. The measurements, however, register two wrong readings: −9.8° and +20°. This error occurs randomly when the cross-correlation of reference signal with thermal noise registers a higher value than the cross-correlation of reference and received signal. The occurrences of such errors, despite not being considered in the modeling, exist and are major sources of errors in simulation and measurement.

Table 3.4 shows the mean and standard deviation of measured angles. The measured mean deviates slightly from the true angle because of errors in steering the turn-table. The increasing trend of standard deviations shows that accuracy of angle estimation errors varies from 0.1° at boresight to 3.0° at ± 20°.

Angle	Case 1: μ_1 / °	σ_1 / °	Case 2: μ_2 / °	σ_2 / °	Case 3: μ_3 / °	σ_3 / °
-20	-18.7	3.0	-17.7	3.3	-18.2	2.6
-15	-13.4	2.0	-13.0	2.1	-13.2	1.9
-10	-9.0	1.4	-8.4	2.0	-8.7	1.3
-5	-4.3	0.7	-3.5	0.6	-3.9	0.6
0	1.8	0.8	0.5	0.3	0.1	0.1
5	4.4	1.5	5.2	0.8	4.7	0.7
10	8.9	2.0	11.6	1.8	9.1	1.3
15	14.1	2.7	14.5	2.1	13.9	2.0
20	18.5	3.2	19.9	2.6	18.5	2.7

Table 3.4: Measured mean and standard deviation of angle-of-arrival for the three cases of SNR.

Theoretical, simulated and measured standard deviations are compared in Figure 3.14−16 for three cases of SNRs. The standard deviation in all cases shows similar values at the angles near boresight. Figure 3.14 shows that Case 1 theoretical standard deviation ranges from 0.6°−0.9°, while measured standard deviation ranges from 0.5°−3.5°. Figure 3.15 shows that Case 2 theoretical standard deviation ranges from 0.4°−0.5°, while measured standard deviation ranges from 0.4°−3.3°. Figure 3.16 shows that Case 3 theoretical standard deviation ranges from 0.3°−0.4°, while measured standard deviation ranges from 0.3°−2.6°. Although similar trends are observed in measured standard deviation *i.e.* the standard deviation increases with decreasing SNR, and increases with increasing θ, the measured values are higher than the theoretical value.

These differences become evident at off-boresight angles, and could be attributed to several reasons. Firstly, the proposed model only accounts for the noise contribution at the main peak of the correlator output. It did not account for effect of combination of noise and signal contributions at other local maxima besides the main maxima, thus underestimating the standard deviation of angle-of-arrival error. Next, as θ increases, the ratio $E_b(\theta) / N_0$ decreases. This decrease in SNR causes the higher order terms of the Taylor-expansion of (3.15) to have more significant contribution. Thus, by truncating the expansion at the 3rd term, the probability density function of time-of-arrival (3.18) becomes less accurate at larger theta values, which compromises the accuracy of angle-of-arrival. Thirdly, the probability of $w(t) > v(t, \theta)$ in (3.7) increases as the SNR decreases. This results in a higher number of erroneous time-of-arrival readings during measurements and simulations. This effect becomes more prominent as θ increases, causing greater deviation from theoretical results at larger θ values. Lastly, equations (3.20) and (3.21) are approximate models of aperture distribution functions of a ridged-horn, causing the modeled received signal to be slightly different from measured received signal at off-boresight angles, as can be seen in [55] and [58]. These differences cause a slight over-estimation of theoretical cross-correlation values compared with measurement.

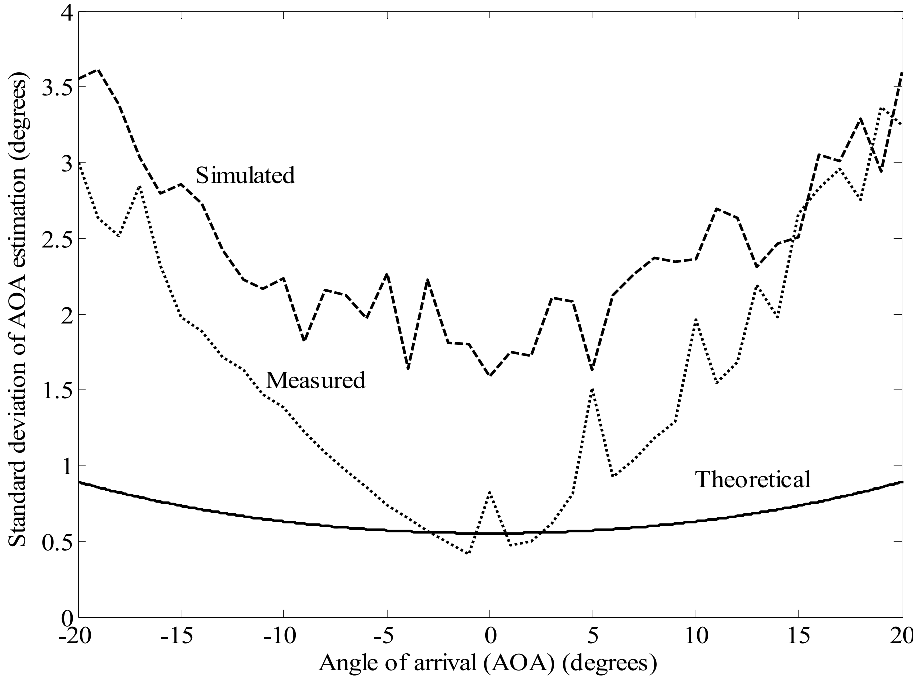

Figure 3.14: Theoretical, simulated and measured standard deviations of angle of arrival (AOA) estimation for Case 1 SNR.

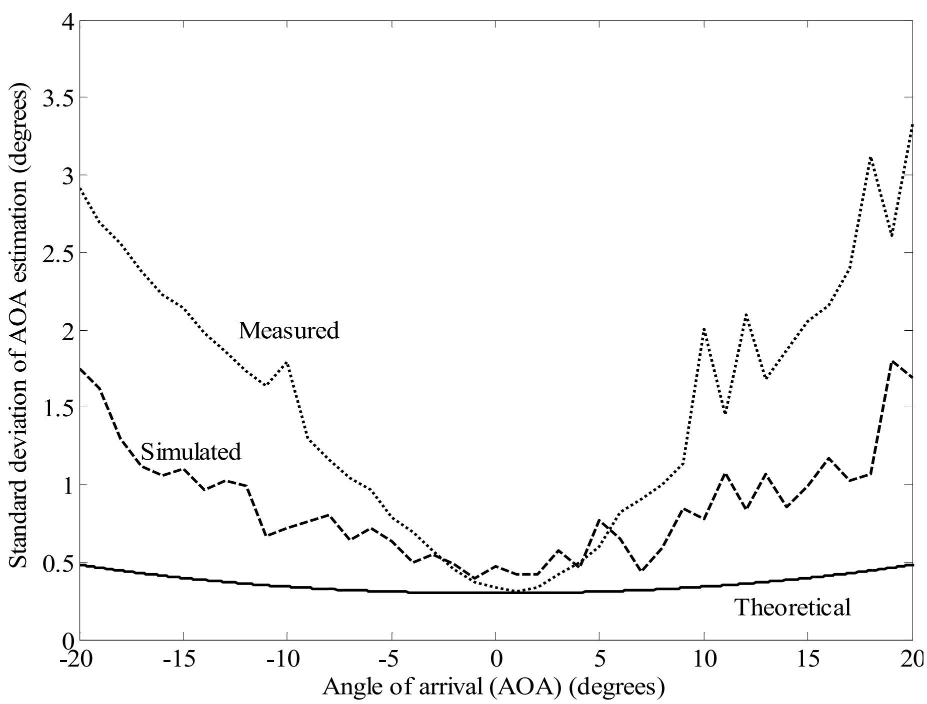

Figure 3.15: Theoretical, simulated and measured standard deviations of angle of arrival (AOA) estimation for Case 2 SNR.

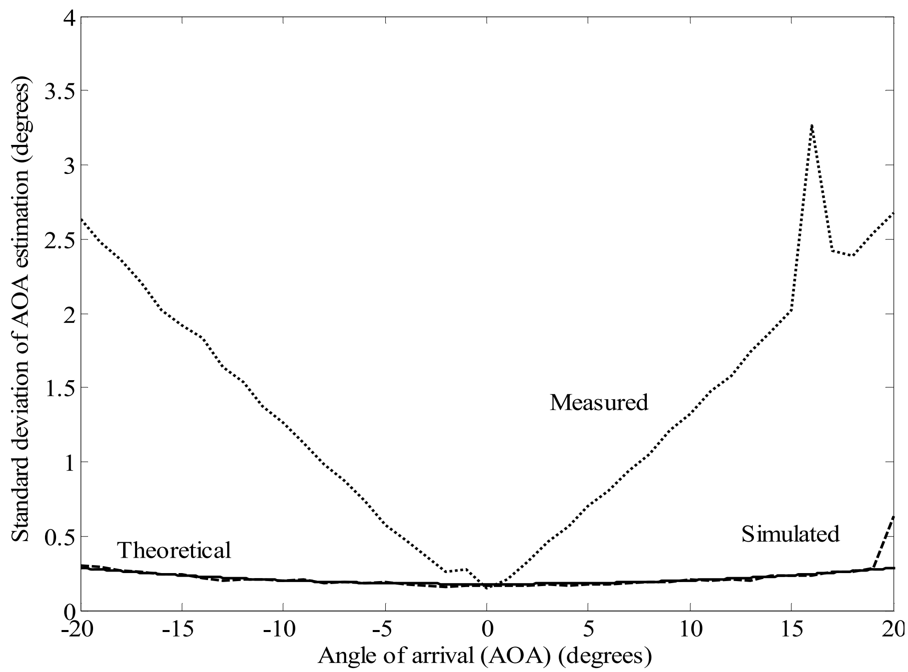

Figure 3.16: Theoretical, simulated and measured standard deviations of angle of arrival (AOA) estimation for Case 3 SNR.

3.8 Chapter Summary

In this chapter, we have presented a method to derive the accuracy of angle-of-arrival (AOA) estimation for thermal noise corrupted signal of UWB receiver. The derivation involves expanding Woodward's [10] estimation of time-of-arrival to incorporate the antenna pulse shaping effect of UWB signals. The probability density function of the angle-of-arrival is also derived and its statistical characteristics compared with simulation and measurements.

CHAPTER 4

DESIGN OF ULTRA-WIDEBAND MONOPULSE RECEIVER

4.1 Introduction

Monopulse technique is a radar technique to locate the angular direction of a target by receiving the incident signal simultaneously with two or more antennas [29]. It is used in existing pulsed and continuous-wave radars to track targets, providing guidance information and steering commands for missiles in missile-range instrumentations [30], [31]. Monopulse technique was proposed for ultra-wideband (UWB) radars [32] by Harmuth *et. al.*. The monopulse sum and difference patterns were derived for the case of equally spaced dipoles receiving short, rectangular pulses [32]−[35], and point antennas receiving Generalised Gaussian UWB Pulses [36]. Furthermore, two methods for finding the target direction were proposed in [36] – the slope processor and the linear-regression processor. Both processors' performances were studied in [36] when the sum and difference signals are corrupted by additive thermal noise.

In this chapter, a square-feed array [30] of four ridged-horns is considered for UWB monopulse receiver. Pulse distortion by the ridged-horn array needs to be considered because the array size is comparable with the electrical length of the incident UWB signal. To model the pulse distortion by the array, we will define a semi-continuous aperture function for the monopulse array, and then inverse Fourier transform it in spatial domain to derive the impulse response. A UWB monopulse receiver is also proposed. Furthermore, the accuracy of the monopulse receiver in estimating the UWB signal's angle-of-arrival is derived. The reception accuracy of the monopulse receiver is modelled as a probability density function, and the prediction accuracy of the model is verified with measured results of angle-of-arrival.

The proposed monopulse receiver is different from the receivers proposed by Harmuth and Hussain [32]−[36] in the following ways: Firstly, the pulse distortion due to the receiving antennas was not considered in [32]−[36], but it is considered in this UWB monopulse receiver. Secondly, the comparator circuit in [32]−[36] was placed after the sliding correlator and variable delay circuit; while in this UWB monopulse receiver, the comparator circuit is placed directly after the receiving antennas. This configuration avoids the problem of amplitude and phase mismatches at the sum and difference channels that may cause performance degradation of the monopulse receiver. Thirdly, to achieve the time resolution in detecting the signal gradient in the slope and linear-regression processors [35], [36], a high speed circuit is required to register the received signal amplitudes at different instances within the pulse width. In the proposed method, the monopulse receiver registers the cross-correlation output at the pulse repetition frequency, thus reducing the design requirements of the receiver.

In Section 4.2, we present an analysis to derive the impulse response of the monopulse square-feed array. In Section 4.3, we present a design of correlator-based UWB monopulse receiver. The receiver's output can then be processed by an Amplitude-Comparison monopulse processor [70] to estimate the angular position of the target. Measurements are presented in Section 4.4 to verify the impulse response of the monopulse array and the performance of the monopulse receiver. In Section 4.5, we will derive the accuracy of the monopulse receiver in estimating the angle-of-arrival, and verify it with measurements.

4.2 Impulse Response of Monopulse Square-Feed Array

A monopulse array of four ridged-horns is arranged in a square-feed configuration in the *x'y'*-plane, as shown in Figure 4.1. (*x', y', z'*) represents the coordinates of the antenna aperture, while (*r,*

θ, φ) represents the coordinates of the incident pulse, where θ and φ denotes the angles subtending from z' and x'-axes respectively. The ridged-horn apertures are labeled as A, B, C and D. All the ridged-horn apertures have the same dimensions of $d_1 \times d_2$ and the same aperture field distribution. The distances between adjacent ridge-horn apertures in the x' and y' directions are s_1 and s_2 respectively. The measured dimensions of the antenna configuration shown in Figure 4.1 are: d_1 = 0.236 m, d_2 = 0.129 m, s_1 = 0.253 m and s_2 = 0.145 m.

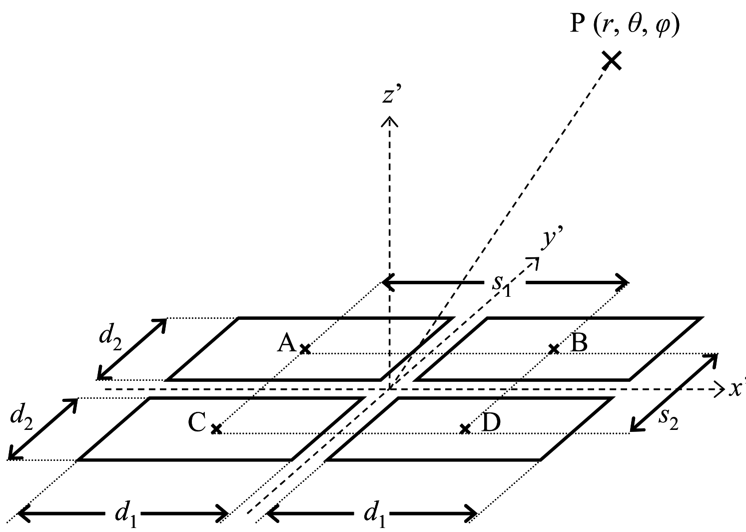

Figure 4.1: Monopulse receiver coordinate systems and antenna dimensions.

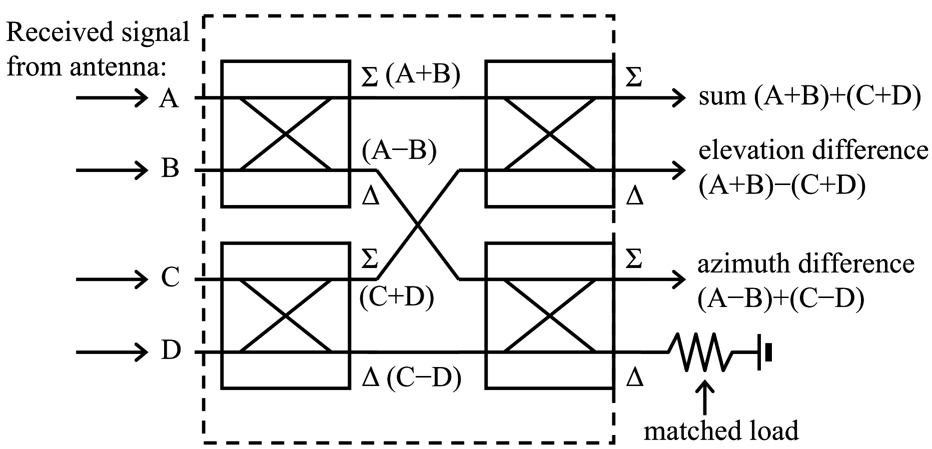

Figure 4.2: Monopulse comparator circuit with four 180° hybrid-couplers.

To obtain the monopulse sum and difference signals, the antenna apertures are connected to a comparator circuit [30] consisting of four 180° hybrid-couplers in the manner as shown in Figure 4.2. The outputs of the comparator are the sum signal, elevation difference signal, and azimuth difference signal. In Chapter 2, the pulse distortions due to the antennas were modeled as the impulse response of the antenna in transmitting or receiving mode − f_t (t, θ, φ) and f_r (t, θ, φ). In this chapter, pulse distortions of the UWB monopulse array are modeled in a similar manner. To do so, impulse response of the monopulse array is defined for the sum, elevation difference and azimuth difference arrays.

Let the impulse responses of the monopulse array for sum, elevation difference and azimuth difference be f_s (t, θ, φ), f_{ed} (t, θ, φ) and f_{ad} (t, θ, φ) respectively. A radiated UWB signal, e (t), is received by the monopulse array at an angle (θ, φ). The received sum, elevation difference and azimuth difference signals − r_s (t, θ, φ), r_{ed} (t, θ, φ) and r_{ad} (t, θ, φ), can be expressed as

$$r_s\left(t,\theta,\phi\right) = f_s\left(t,\theta,\phi\right) \otimes e\left(t\right) \tag{4.1}$$

$$r_{ed}\left(t,\theta,\phi\right) = f_{ed}\left(t,\theta,\phi\right) \otimes e\left(t\right) \tag{4.2}$$

$$r_{ad}\left(t,\theta,\phi\right) = f_{ad}\left(t,\theta,\phi\right) \otimes e\left(t\right) \tag{4.3}$$

Equations (4.1)−(4.3) can also be expressed in frequency domain, in which the spectrum of the monopulse signals R_s $(\omega, \theta, \varphi)$, R_{ed} $(\omega, \theta, \varphi)$ and R_{ad} $(\omega, \theta, \varphi)$ are the product of the spectrum of the incident signal E (ω) and the transfer functions of the monopulse array of the sum, elevation difference and azimuth difference − F_s $(\omega, \theta, \varphi)$, F_{ed} $(\omega, \theta, \varphi)$ and F_{ad} $(\omega, \theta, \varphi)$.

$$R_s\left(\omega,\theta,\phi\right) = F_s\left(\omega,\theta,\phi\right) \cdot E\left(\omega\right) \tag{4.4}$$

$$R_{ed}\left(\omega,\theta,\phi\right) = F_{ed}\left(\omega,\theta,\phi\right) \cdot E\left(\omega\right) \tag{4.5}$$

$$R_{ad}\left(\omega,\theta,\phi\right) = F_{ad}\left(\omega,\theta,\phi\right) \cdot E\left(\omega\right) \tag{4.6}$$

F_s $(\omega, \theta, \varphi)$, F_{ed} $(\omega, \theta, \varphi)$ and F_{ad} $(\omega, \theta, \varphi)$ are the normalized gain of the monopulse array. The normalized gain are related to the array's aperture field distributions of the monopulse sum, elevation difference and azimuth difference − g_s (x', y'), g_{ed} (x', y') and g_{ad} (x', y'), as

$$F_s\left(\omega,\theta,\phi\right)=\int_{area} g_s\left(x',y'\right)\exp\left[j\frac{\omega}{c}\sin\theta\left(x'\cos\phi+y'\sin\phi\right)\right]dx'dy' \tag{4.7}$$

$$F_{ed}\left(\omega,\theta,\phi\right)=\int_{area} g_{ed}\left(x',y'\right)\exp\left[j\frac{\omega}{c}\sin\theta\left(x'\cos\phi+y'\sin\phi\right)\right]dx'dy' \tag{4.8}$$

$$F_{ad}\left(\omega,\theta,\phi\right)=\int_{area} g_{ad}\left(x',y'\right)\exp\left[j\frac{\omega}{c}\sin\theta\left(x'\cos\phi+y'\sin\phi\right)\right]dx'dy' \tag{4.9}$$

where c is the speed of light in free space; g_s (x', y') is the aperture field distribution function of antenna array in A+B+C+D configuration (Figure 4.1); g_{ed} (x', y') is the field distribution function of antenna array in A+B−C−D configuration (Figure 4.1); and g_{ad} (x', y') is the field distribution function of antenna array in A−B+C−D configuration (Figure 4.1). Assuming that the x' and y' terms of g_s (x', y'), g_{ed} (x', y') and g_{ad} (x', y') are separable, the aperture field distribution functions can be re-written as

$$g_s\left(x',y'\right)=g_s\left(x'\right)g_s\left(y'\right)=\left[g\left(x'-\frac{s_1}{2}\right)+g\left(x'+\frac{s_1}{2}\right)\right]\left[g\left(y'-\frac{s_2}{2}\right)+g\left(y'+\frac{s_2}{2}\right)\right] \tag{4.10}$$

$$g_{ed}\left(x',y'\right)=g_{ed}\left(x'\right)g_{ed}\left(y'\right)=\left[g\left(x'-\frac{s_1}{2}\right)+g\left(x'+\frac{s_1}{2}\right)\right]\left[g\left(y'-\frac{s_2}{2}\right)-g\left(y'+\frac{s_2}{2}\right)\right] \tag{4.11}$$

$$g_{ad}\left(x',y'\right)=g_{ad}\left(x'\right)g_{ad}\left(y'\right)=\left[g\left(x'-\frac{s_1}{2}\right)-g\left(x'+\frac{s_1}{2}\right)\right]\left[g\left(y'-\frac{s_2}{2}\right)+g\left(y'+\frac{s_2}{2}\right)\right] \tag{4.12}$$

where g (x') is the aperture field function of the ridged-horn antenna in the x'-axis, and g (y') is the aperture field function of the ridged-horn antenna in the y'-axis. By substituting (4.10)−(4.12) into

(4.7)−(4.9), the normalized field patterns of the monopulse array − $F_s(\omega, \theta, \varphi)$, $F_{ed}(\omega, \theta, \varphi)$ and $F_{ad}(\omega, \theta, \varphi)$, can be expressed as

$$F_s(\omega,\theta,\phi) = \frac{\left(\int_{\beta_1}^{\alpha_1} g(x'-s_1/2)\mathrm{e}^{j\omega x'\sin\theta\cos\phi/c}\,dx' + \int_{-\alpha_1}^{-\beta_1} g(x'+s_1/2)\mathrm{e}^{j\omega x'\sin\theta\cos\phi/c}\,dx'\right)}{\left(\int_{\beta_2}^{\alpha_2} g(y'-s_2/2)\mathrm{e}^{j\omega y'\sin\theta\sin\phi/c}\,dy' + \int_{-\alpha_2}^{-\beta_2} g(y'+s_2/2)\mathrm{e}^{j\omega y'\sin\theta\sin\phi/c}\,dy'\right)} \quad (4.13)$$

$$F_{ed}(\omega,\theta,\phi) = \frac{\left(\int_{\beta_1}^{\alpha_1} g(x'-s_1/2)\mathrm{e}^{j\omega x'\sin\theta\cos\phi/c}\,dx' + \int_{-\alpha_1}^{-\beta_1} g(x'+s_1/2)\mathrm{e}^{j\omega x'\sin\theta\cos\phi/c}\,dx'\right)}{\left(\int_{\beta_2}^{\alpha_2} g(y'-s_2/2)\mathrm{e}^{j\omega y'\sin\theta\sin\phi/c}\,dy' - \int_{-\alpha_2}^{-\beta_2} g(y'+s_2/2)\mathrm{e}^{j\omega y'\sin\theta\sin\phi/c}\,dy'\right)} \quad (4.14)$$

$$F_{ad}(\omega,\theta,\phi) = \frac{\left(\int_{\beta_1}^{\alpha_1} g(x'-s_1/2)\mathrm{e}^{j\omega x'\sin\theta\cos\phi/c}\,dx' - \int_{-\alpha_1}^{-\beta_1} g(x'+s_1/2)\mathrm{e}^{j\omega x'\sin\theta\cos\phi/c}\,dx'\right)}{\left(\int_{\beta_2}^{\alpha_2} g(y'-s_2/2)\mathrm{e}^{j\omega y'\sin\theta\sin\phi/c}\,dy' + \int_{-\alpha_2}^{-\beta_2} g(y'+s_2/2)\mathrm{e}^{j\omega y'\sin\theta\sin\phi/c}\,dy'\right)} \quad (4.15)$$

where $\alpha_1 = (s_1 + d_1) / 2$, $\alpha_2 = (s_2 + d_2) / 2$, $\beta_1 = (s_1 - d_1) / 2$ and $\beta_2 = (s_2 - d_2) / 2$. s_1, s_2, d_1 and d_2 are the antenna dimensions of Figure 4.1. Using a similar approach discussed in Chapter 2, we apply a change in variable of $x' = -tc / (\sin\theta\cos\varphi)$ and $y' = -tc / (\sin\theta\sin\varphi)$ to (4.10)−(4.12), and then inverse Fourier transform (4.10)−(4.12) to find the time-domain impulse responses $f_s(t, \theta, \varphi)$, $f_{ed}(t, \theta, \varphi)$ and $f_{ad}(t, \theta, \varphi)$,

$$f_s(t,\theta,\phi) = \frac{c\left\{\begin{array}{l} g\left[\dfrac{c(t-\tau_{s1})}{\sin\theta\cos\phi}\right]\dfrac{u(t-\tau_{s1}-\tau_{d1})-u(t-\tau_{s1}+\tau_{d1})}{\sin\theta\cos\phi}+ \\ g\left[\dfrac{c(t+\tau_{s1})}{\sin\theta\cos\phi}\right]\dfrac{u(t+\tau_{s1}-\tau_{d1})-u(t+\tau_{s1}+\tau_{d1})}{\sin\theta\cos\phi} \end{array}\right\}\otimes}{c\left\{\begin{array}{l} g\left[\dfrac{c(t-\tau_{s2})}{\sin\theta\sin\phi}\right]\dfrac{u(t-\tau_{s2}-\tau_{d2})-u(t-\tau_{s2}+\tau_{d2})}{\sin\theta\sin\phi}+ \\ g\left[\dfrac{c(t+\tau_{s2})}{\sin\theta\sin\phi}\right]\dfrac{u(t+\tau_{s2}-\tau_{d2})-u(t+\tau_{s2}+\tau_{d2})}{\sin\theta\sin\phi} \end{array}\right\}} \quad (4.16)$$

$$f_{ed}\left(t,\theta,\phi\right)=\begin{matrix} c\left\{\begin{matrix} g\left[\dfrac{c\left(t-\tau_{s1}\right)}{\sin\theta\cos\phi}\right]\dfrac{u\left(t-\tau_{s1}-\tau_{d1}\right)-u\left(t-\tau_{s1}+\tau_{d1}\right)}{\sin\theta\cos\phi}+ \\ g\left[\dfrac{c\left(t+\tau_{s1}\right)}{\sin\theta\cos\phi}\right]\dfrac{u\left(t+\tau_{s1}-\tau_{d1}\right)-u\left(t+\tau_{s1}+\tau_{d1}\right)}{\sin\theta\cos\phi} \end{matrix}\right\}\otimes \\ c\left\{\begin{matrix} g\left[\dfrac{c\left(t-\tau_{s2}\right)}{\sin\theta\sin\phi}\right]\dfrac{u\left(t-\tau_{s2}-\tau_{d2}\right)-u\left(t-\tau_{s2}+\tau_{d2}\right)}{\sin\theta\sin\phi}- \\ g\left[\dfrac{c\left(t+\tau_{s2}\right)}{\sin\theta\sin\phi}\right]\dfrac{u\left(t+\tau_{s2}-\tau_{d2}\right)-u\left(t+\tau_{s2}+\tau_{d2}\right)}{\sin\theta\sin\phi} \end{matrix}\right\} \end{matrix} \tag{4.17}$$

$$f_{ad}\left(t,\theta,\phi\right)=\begin{matrix} c\left\{\begin{matrix} g\left[\dfrac{c\left(t-\tau_{s1}\right)}{\sin\theta\cos\phi}\right]\dfrac{u\left(t-\tau_{s1}-\tau_{d1}\right)-u\left(t-\tau_{s1}+\tau_{d1}\right)}{\sin\theta\cos\phi}- \\ g\left[\dfrac{c\left(t+\tau_{s1}\right)}{\sin\theta\cos\phi}\right]\dfrac{u\left(t+\tau_{s1}-\tau_{d1}\right)-u\left(t+\tau_{s1}+\tau_{d1}\right)}{\sin\theta\cos\phi} \end{matrix}\right\}\otimes \\ c\left\{\begin{matrix} g\left[\dfrac{c\left(t-\tau_{s2}\right)}{\sin\theta\sin\phi}\right]\dfrac{u\left(t-\tau_{s2}-\tau_{d2}\right)-u\left(t-\tau_{s2}+\tau_{d2}\right)}{\sin\theta\sin\phi}+ \\ g\left[\dfrac{c\left(t+\tau_{s2}\right)}{\sin\theta\sin\phi}\right]\dfrac{u\left(t+\tau_{s2}-\tau_{d2}\right)-u\left(t+\tau_{s2}+\tau_{d2}\right)}{\sin\theta\sin\phi} \end{matrix}\right\} \end{matrix} \tag{4.18}$$

where $\tau_{d1} = d_1 \sin\theta \cos\varphi / (2c)$, $\tau_{s1} = s_1 \sin\theta \cos\varphi / (2c)$, $\tau_{d2} = d_2 \sin\theta \sin\varphi / (2c)$ and $\tau_{s2} = s_2 \sin\theta \sin\varphi / (2c)$.

4.3 Monopulse Receiver

Figure 4.3 shows a block diagram of the proposed monopulse receiver. Transmitted UWB signals incident to the receiver's square-feed array of ridged-horns A, B, C and D is received and then added or subtracted from each other in the comparator circuit. The comparator circuit outputs, *S*, *AD* and *ED*, as shown in Figure 4.3, are then multiplied with their reference signals $p_s(t)$, $p_{da}(t)$ and $p_{de}(t)$. The outputs of the multipliers are then integrated over the pulse repetition interval *T*. The output of the integrator circuits are then sampled at the pulse repetition frequency, and processed by an amplitude-comparison monopulse processor [60].

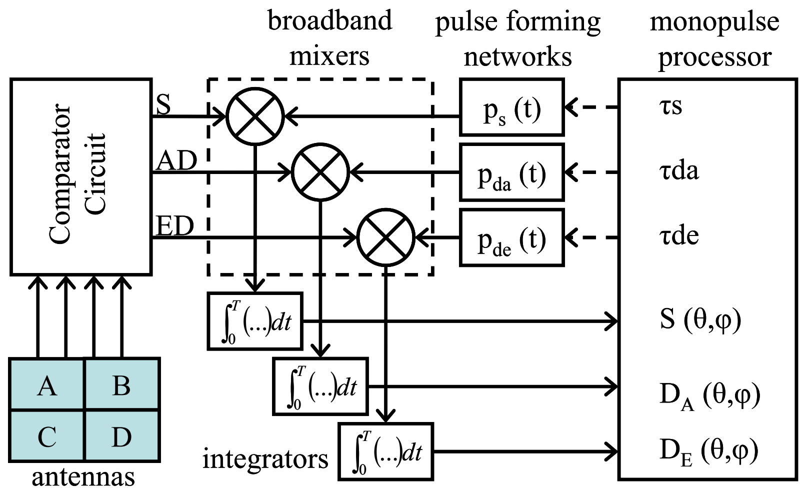

Figure 4.3: Block diagram of UWB monopulse receiver.

The reference signals can be generated by a bank of pulse forming networks (PFN) [39], [40], [59] that are triggered at the appropriate instances. The triggering instance for each PFN can be estimated by sweeping the delay of the reference signal across the pulse repetition interval and then finding the maximum cross-correlation value of the sum signal. The method of estimating the triggering instance of the receiver is similar to the time-of-arrival estimation method described in Chapter 3. In this section, it is assumed that the triggering instance has been estimated by ranging system, and the UWB monopulse receiver is able to trigger the PFNs at the appropriate times (τ_s, τ_{da} and τ_{de}) such that the cross-correlation value of the sum signal is maximum. In a realistic receiver, the triggering instance may not be accurate because of antenna noise that is present in the received signals. The effect of antenna noise on the accuracy of this monopulse receiver will be further discussed in Section 4.5.

The reference signal of the sum channel, p_s (t), is equal to the received sum signal at boresight direction, r_s (t, θ = 0°, φ = 0°). The reference signal of the azimuth difference channel, p_{da} (t), however, is equal to the received azimuth difference signal in a direction where D_A (θ, φ = 0°) is a global maximum. Similarly, the reference signal of the elevation difference channel, p_{de} (t), is equal to the received elevation difference signal in a direction where D_E (θ, φ = 90°) is a global maximum. Let the angles where the monopulse output voltages D_A and D_E are global maximum be (θ_A, 0°) and (θ_E, 90°) respectively.

Based on the description above, both D_A and D_E will be in global maximum when $r_{da}(t)$ and $r_{de}(t)$ has the highest signal energy. Hence, to find (θ_A, 0°) and (θ_E, 90°), we need to find an analytical expression of $r_{da}(t)$ and $r_{de}(t)$, and then find the angle (θ_A, 0°) when $r_{da}(t)$ is maximum, and the angle (θ_E, 90°) when $r_{de}(t)$ is maximum. To find an analytical expression of $r_{da}(t)$ and $r_{de}(t)$, we first assume that the field distribution of the ridged-horn aperture to be rectangular in shape with an area of $d_1 \times d_2$. By doing so, we can now derive the aperture distribution function of the sum, azimuth difference and elevation difference array as

$$g_s(x',y') = \left[\Pi\left(x'/d_1 - s_1/2\right) + \Pi\left(x'/d_1 + s_1/2\right)\right] \cdot \left[\Pi\left(y'/d_2 - s_2/2\right) + \Pi\left(y'/d_2 + s_2/2\right)\right] \quad (4.19)$$

$$g_{ed}(x',y') = \left[\Pi\left(x'/d_1 - s_1/2\right) + \Pi\left(x'/d_1 + s_1/2\right)\right] \cdot \left[\Pi\left(y'/d_2 - s_2/2\right) - \Pi\left(y'/d_2 + s_2/2\right)\right] \quad (4.20)$$

$$g_{ad}(x',y') = \left[\Pi\left(x'/d_1 - s_1/2\right) - \Pi\left(x'/d_1 + s_1/2\right)\right] \cdot \left[\Pi\left(y'/d_2 - s_2/2\right) + \Pi\left(y'/d_2 + s_2/2\right)\right] \quad (4.21)$$

where $\Pi(t)$ is a rectangle function. Based on the substitution method described in Section 4.2, the impulse response of the sum, azimuth difference and elevation difference channel can be derived as

$$f_s(t,\theta,\phi) = c^2 \frac{\Pi\left(\tau_{d1}t + \tau_{s1}\right) + \Pi\left(\tau_{d1}t - \tau_{s1}\right)}{\sin\theta\cos\phi} \otimes \frac{\Pi\left(\tau_{d2}t + \tau_{s2}\right) + \Pi\left(\tau_{d2}t - \tau_{s2}\right)}{\sin\theta\sin\phi} \quad (4.22)$$

$$f_{ed}(t,\theta,\phi) = c^2 \frac{\Pi\left(\tau_{d1}t + \tau_{s1}\right) + \Pi\left(\tau_{d1}t - \tau_{s1}\right)}{\sin\theta\cos\phi} \otimes \frac{\Pi\left(\tau_{d2}t + \tau_{s2}\right) - \Pi\left(\tau_{d2}t - \tau_{s2}\right)}{\sin\theta\sin\phi} \quad (4.23)$$

$$f_{ad}(t,\theta,\phi) = c^2 \frac{\Pi\left(\tau_{d1}t + \tau_{s1}\right) - \Pi\left(\tau_{d1}t - \tau_{s1}\right)}{\sin\theta\cos\phi} \otimes \frac{\Pi\left(\tau_{d2}t + \tau_{s2}\right) + \Pi\left(\tau_{d2}t - \tau_{s2}\right)}{\sin\theta\sin\phi} \quad (4.24)$$

Let a radiated UWB signal, possibly from a transponder or a radar target reflection, be incident on the monopulse array in Figure 4.1 at an angle (θ, φ). The signal is received by antennas A, B, C and D.

The received signals pass through the comparator circuit in Figure 4.2 to generate monopulse sum, azimuth difference and elevation difference signals. Let the incident pulse, e (t), be a second derivative Gaussian function, with $\tau = 60$ ps, where

$$e(t) = \left(2t^2/\tau^2 - 1\right)\exp\left(-t^2/\tau^2\right) \tag{4.25}$$

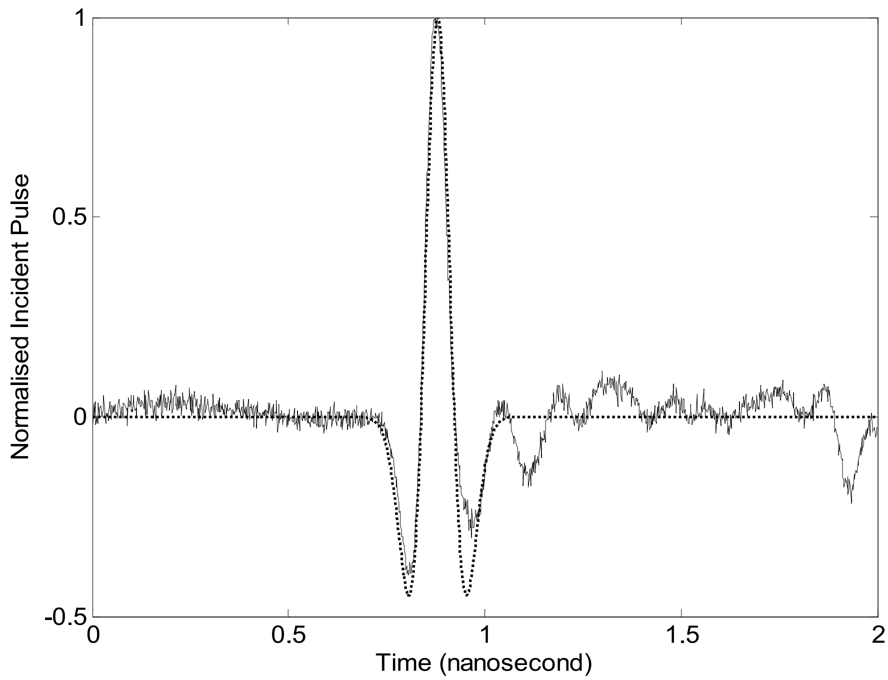

Figure 4.4: Experimental (line) and modeled (dotted line) incident signal.

In Figure 4.4, e (t) (dotted line) is compared with the measured received signal (line) of a ridged-horn antenna used in the monopulse array of Figure 4.1. To find the received monopulse sum and difference signals, we substitute e (t) into (4.1)−(4.3). The monopulse sum and difference signals at the azimuth ($x'z'$) plane, r_s (t, θ, $\varphi = 0°$) and r_{da} (t, θ, $\varphi = 0°$), can be found by substituting $\varphi = 0°$ into (4.1) and (4.3). The monopulse sum and difference signals at the elevation ($y'z'$) plane, r_s (t, θ, φ = 90°) and r_{de} (t, θ, $\varphi = 90°$), can be found by substituting $\varphi = 90°$ into (4.1) and (4.2). Assuming that the impulse responses of the sum and difference monopulse array is defined in (4.22)−(4.24), r_s (t, θ, φ = 0°), r_{da} (t, θ, φ = 0°), r_s (t, θ, φ = 90°) and r_{de} (t, θ, φ = 90°) can be derived as

$$r_s\left(t,\theta,\phi=0°\right)=\frac{\tau^2c^2}{2\sin\theta}\Big[m'\left(t+\tau_{\alpha 1}\right)-m'\left(t+\tau_{\beta 1}\right)+m'\left(t-\tau_{\beta 1}\right)-m'\left(t-\tau_{\alpha 1}\right)\Big] \tag{4.26}$$

$$r_{da}\left(t,\theta,\phi=0°\right)=\frac{\tau^2c^2}{2\sin\theta}\Big[m'\left(t+\tau_{\alpha,i}\right)-m'\left(t+\tau_{\beta,i}\right)-m'\left(t-\tau_{\beta,i}\right)+m'\left(t-\tau_{\alpha,i}\right)\Big] \tag{4.27}$$

$$r_s\left(t,\theta,\phi=90°\right)=\frac{\tau^2c^2}{2\sin\theta}\Big[m'\left(t+\tau_{\alpha 2}\right)-m'\left(t+\tau_{\beta 2}\right)+m'\left(t-\tau_{\beta 2}\right)-m'\left(t-\tau_{\alpha 2}\right)\Big] \tag{4.28}$$

$$r_{de}\left(t,\theta,\phi=90°\right)=\frac{\tau^2c^2}{2\sin\theta}\Big[m'\left(t+\tau_{\alpha,i}\right)-m'\left(t+\tau_{\beta,i}\right)-m'\left(t-\tau_{\beta,i}\right)+m'\left(t-\tau_{\alpha,i}\right)\Big] \tag{4.29}$$

where m' (t) is the first derivative Gaussian signal expressed as

$$m'\left(t\right)=-2t/\tau^2\exp\left(-t^2/\tau^2\right) \tag{4.30}$$

$\tau_{\alpha 1}$, $\tau_{\alpha 2}$, $\tau_{\beta 1}$ and $\tau_{\beta 2}$ of (4.26)−(4.29) are delays expressed as $\tau_{\alpha 1} = (s_1 + d_1) \sin\theta / 2c$, $\tau_{\alpha 2} = (s_2 + d_2) \sin\theta / 2c$, $\tau_{\beta 1} = (s_1 - d_1) \sin\theta / 2c$, and $\tau_{\beta 2} = (s_2 - d_2) \sin\theta$. It is noted here that (4.26) and (4.28) are even functions of θ, while (4.27) and (4.29) are odd functions of θ. This even / odd property of the sum / difference signal enables the monopulse receiver to decide on whether the incident signal is located at the left or right half plane.

The theoretical reference signals for cross-correlation, r_{s0} (t), r_{da0} (t) and r_{de0} (t), can be found by substituting appropriate angle values into (4.26)−(4.29). Since the sum signal has maximum amplitude at boresight, the theoretical sum channel reference signal, r_{s0} (t), can be found by substituting $\theta = \varphi = 0°$ into (4.26),

$$r_{s0}\left(t\right)=r_s\left(t,\theta=0°,\phi=0°\right) \tag{4.31}$$

The angle where $r_{da}(t)$ of (4.27) is at global maximum is θ_A and the angle where $r_{de}(t)$ of (4.29) is at global maximum be θ_E. Because $r_{da}(t)$ and $r_{de}(t)$ are odd functions of θ, the angles at which they are at global minimum are $-\theta_A$ and $-\theta_E$. Numerical method is used to find these angles. Once found, θ_A and θ_E, are then substituted back into (4.27) and (4.29),

$$r_{da0}(t) = r_{da}(t, \theta = \theta_A, \phi = 0°) \tag{4.32}$$

$$r_{de0}(t) = r_{de}(t, \theta = \theta_E, \phi = 90°) \tag{4.33}$$

The ideal sum channel reference signal (4.31) can be generated since it is a second derivative Gaussian function. The ideal difference channel reference signals, (4.32) and (4.33), however, are complex and difficult to generate. To simplify the pulse generation process, we approximate (4.32) and (4.33) with first derivative Gaussian pulses, $a_{DA}(t)$ and $a_{DE}(t)$, where

$$a_{DA}(t) = -\left(2t/d_{DA}^2\right)\exp\left(-t^2/d_{DA}^2\right) \tag{4.34}$$

$$a_{DE}(t) = -\left(2t/d_{DE}^2\right)\exp\left(-t^2/d_{DE}^2\right) \tag{4.35}$$

with pulse widths of d_{DA} and d_{DE}. d_{DA} can be calculated from the time difference between the instance when $r_{da0}(t)$ (4.27) is maximum, $t_{max\,(rda0)}$, and the instance when $r_{da0}(t)$ (4.27) is minimum, $t_{min\,(rda0)}$; while d_{DE} can be calculated from the time difference between the instance when $r_{de0}(t)$ (4.29) is maximum, $t_{max\,(rde0)}$, and the instance when $r_{de0}(t)$ (4.29) is minimum, $t_{min\,(rde0)}$,

$$d_{DA} = \frac{1}{\sqrt{2}}\left|t_{\max(rda0)} - t_{\min(rda0)}\right| \tag{4.36}$$

$$d_{DE} = \frac{1}{\sqrt{2}}\left|t_{\max(rde0)} - t_{\min(rde0)}\right| \tag{4.37}$$

To illustrate the calculation of the sum and difference reference signals, let the incident signal be second derivative Gaussian pulse as shown in (4.25), and the aperture field distribution functions of the receiving array be (4.19)−(4.21). θ_A can be found as 3.9°. Figure 4.5 compares the measured difference signal at azimuth plane (θ = θ_A = 3.9°) with theoretical difference signal (4.32) and approximated reference signal (4.34). By coding (4.27) in MATLAB code to find the global maximum and global minimum points for all values of t and θ, the time difference between the instances of global maximum and global minimum in (4.27) is found to be 73 ps. By substituting the time difference into (4.36), it can be shown that d_{DA} = 52 ps. Furthermore, by substituting d_{DA} into (4.34), the approximated reference signal a_{DA} (t) can be plotted out, as shown in Figure 4.5.

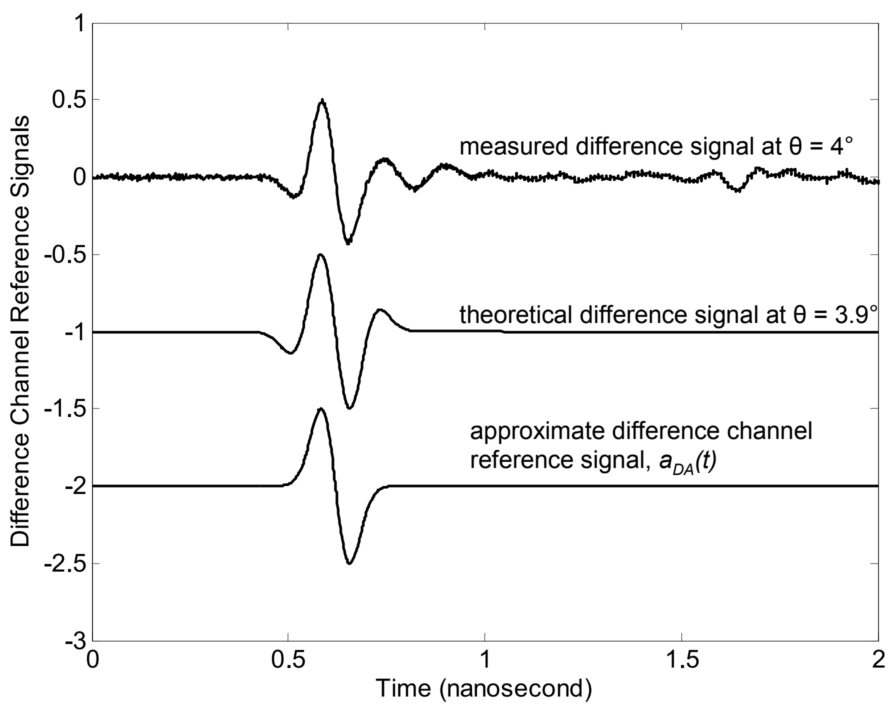

Figure 4.5: Theoretical, measured and approximate difference signal in the azimuth plane for $\theta = \theta_A \approx$ 3.9°.

Using (4.34) and (4.35) as reference signals for the cross-correlation receivers in Figure 4.4 are valid only if the incident UWB signal has a pulse shape of (4.25). UWB monopulse radars employing other pulse shapes can derive their respective reference signals based on the method proposed in this section. However, should the incident signal suffers slight pulse distortion from (4.25), the monopulse receiver still remains functional, although with degraded performance. The rate of performance degradation is proportional to the extent of pulse distortion. By cross-correlating the sum channel reference signal (4.31) with the received sum signal (4.26) and (4.28), we can derive the azimuth sum output voltage, S (θ, 0), and the elevation sum output voltage, S (θ, π / 2). By cross-correlating the azimuth / elevation difference channel reference signal (4.34) and (4.35) with the received azimuth / elevation difference signal (4.27) and (4.29), we can derive the azimuth difference output voltage, D_A (θ, 0), and the elevation difference output voltage, D_E (θ, π / 2). The derived output voltages are expressed as follow:

$$S(\theta,0) = \max\left\{\frac{\tau^4}{4\sin\theta}\begin{bmatrix} m'''\left(t+\tau_{\alpha 1}-\tau_s,\tau+d_s\right)-m'''\left(t+\tau_{\beta 1}-\tau_s,\tau+d_s\right) \\ +m'''\left(t-\tau_{\beta 1}-\tau_s,\tau+d_s\right)-m'''\left(t-\tau_{\alpha 1}-\tau_s,\tau+d_s\right)\end{bmatrix}\right\} \tag{4.38}$$

$$S\left(\theta,\frac{\pi}{2}\right) = \max\left\{\frac{\tau^4}{4\sin\theta}\begin{bmatrix} m'''\left(t+\tau_{\alpha 2}-\tau_s,\tau+d_s\right)-m'''\left(t+\tau_{\beta 2}-\tau_s,\tau+d_s\right) \\ +m'''\left(t-\tau_{\beta 2}-\tau_s,\tau+d_s\right)-m'''\left(t-\tau_{\alpha 2}-\tau_s,\tau+d_s\right)\end{bmatrix}\right\} \tag{4.39}$$

$$D_A(\theta,0) = \max\left\{\frac{\tau^4}{4\sin\theta}\begin{bmatrix} m''\left(t+\tau_{\alpha 1}-\tau_{DA},\tau+d_{DA}\right)-m''\left(t+\tau_{\alpha 1}-\tau_{DA},\tau+d_{DA}\right) \\ -m''\left(t-\tau_{\alpha 1}-\tau_{DA},\tau+d_{DA}\right)+m''\left(t+\tau_{\alpha 1}-\tau_{DA},\tau+d_{DA}\right)\end{bmatrix}\right\} \tag{4.40}$$

$$D_E\left(\theta,\frac{\pi}{2}\right) = \max\left\{\frac{\tau^4}{4\sin\theta}\begin{bmatrix} m''\left(t+\tau_{\alpha 2}-\tau_{DA},\tau+d_{DA}\right)-m''\left(t+\tau_{\alpha 2}-\tau_{DA},\tau+d_{DA}\right) \\ -m''\left(t-\tau_{\alpha 2}-\tau_{DA},\tau+d_{DA}\right)+m''\left(t+\tau_{\alpha 2}-\tau_{DA},\tau+d_{DA}\right)\end{bmatrix}\right\} \tag{4.41}$$

where $m''(t, \tau)$ and $m'''(t, \tau)$ are the second and third derivatives of Gaussian function, expressed as

$$m''\left(t,\tau\right) = 2/\tau^2\left(2t^2/\tau^2-1\right)\exp\left(-t^2/\tau^2\right) \tag{4.42}$$

$$m'''\left(t,\tau\right) = 4t/\tau^4\left(3-2t^2/\tau^2\right)\exp\left(-t^2/\tau^2\right) \tag{4.43}$$

4.4 Measurements

Measurements are conducted to validate the sum and difference waveforms given in (4.26)−(4.29), the azimuth sum channel pattern (4.38), and the azimuth difference channel pattern (4.40). Figure 4.6 shows the experimental setup to measure time-domain received monopulse sum and difference signals at various angles. A pulse source with $V_{p\text{-}p}$ = 2.0 V, *PRF* = 1 MHz and Jitter = 1.5 ps (rms) is used as transmitter. The receiver consists of two identical ridged-horn antennas placed side-by-side as a one-dimension monopulse receiver. This arrangement restricts the monopulse measurement to azimuth plane only. The return loss of the ridged-horn antenna is less than -10 dB over 1 to 18 GHz. The ridged-horns are connected to a 180° hybrid-coupler with 3-dB bandwidth from 1 to 12.4 GHz. In the measurements, the hybrid-coupler introduces some signal distortion. Furthermore, the amplitude and phase mismatches in the hybrid-coupler may result in inefficient combining of the antenna outputs to form the monopulse sum and difference signals. These imperfections, however, are negligible, and not modeled in the derivations. The sum and difference signals of the coupler are recorded by a 40 GS/s sampling oscilloscope, averaged at 1,024 times.

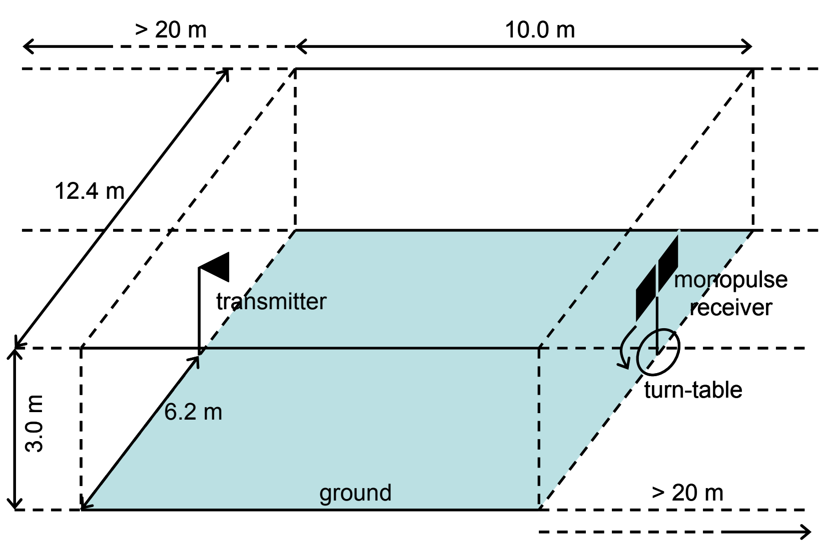

Figure 4.6: Experimental setup to measure the received monopulse sum and difference signals.

The receiving monopulse array is placed on a turn-table so that the axis of the rotation is located in the middle of the apertures. The sum and difference signals are measured from -20° to 20° in steps of 1°. To find the sum and difference patterns at the output of the cross-correlation receiver, the measured signals are mathematically correlated with reference signals (4.31), (4.34) and (4.35) derived in Section 4.3. The presence of ridges in a horn concentrates the field intensity at the middle of the horn aperture. Hence, a rectangular aperture function used in Section 4.3 may not be an accurate approximation for the aperture field distribution. To obtain a better approximation of the aperture field distribution, we model it as a 12-th power half-cosine function. Figure 4.7 plots the normalized energy pattern, as defined in Chapter 2, of antenna aperture functions of rectangular shape (Trace 1), $\cos^2$ shape (Trace 2), $\cos^4$ shape (Trace 3), $\cos^8$ shape (Trace 4) and $\cos^{12}$ shape (Trace 5). It is observed in Figure 4.7 that when n = 12, the aperture function provides the best fit with the measured radiation pattern (Trace 6).

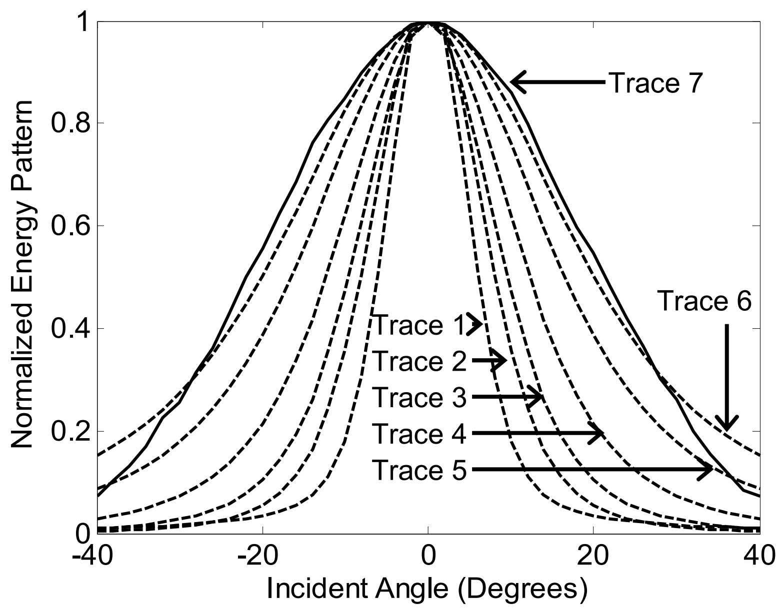

Legend:
- Trace 1 shows radiation pattern when aperture field is approximated by rectangular function.
- Traces 2-6 show the radiation patterns when the approximations are cos^1, cos^2, cos^4, cos^8 and cos^{12} functions.
- Trace 7 shows the measured radiation pattern of a single ridged-horn.

Figure 4.7: Comparison between measured normalized energy pattern of a single ridged-horn with the normalized energy patterns derived from various theoretical aperture functions.

Hence, the impulse response of the sum and azimuth difference monopulse array can be re-written as,

$$f_s\left(t,\theta,\phi=0^\circ\right)=\frac{c}{\sin\theta}\left\{\begin{bmatrix}u\left(t-\tau_{s1}-\tau_{d1}\right)-\\u\left(t-\tau_{s1}+\tau_{d1}\right)\end{bmatrix}\cos^{12}\left[\frac{c\pi\left(t-\tau_{s1}\right)}{d\sin\theta}\right]+\begin{bmatrix}u\left(t+\tau_{s1}-\tau_{d1}\right)-\\u\left(t+\tau_{s1}+\tau_{d1}\right)\end{bmatrix}\cos^{12}\left[\frac{c\pi\left(t+\tau_{s1}\right)}{d\sin\theta}\right]\right\} \tag{4.44}$$

$$f_{ad}\left(t,\theta,\phi=0^\circ\right)=\frac{c}{\sin\theta}\left\{\begin{bmatrix}u\left(t-\tau_{s1}-\tau_{d1}\right)-\\u\left(t-\tau_{s1}+\tau_{d1}\right)\end{bmatrix}\cos^{12}\left[\frac{c\pi\left(t-\tau_{s1}\right)}{d\sin\theta}\right]-\begin{bmatrix}u\left(t+\tau_{s1}-\tau_{d1}\right)-\\u\left(t+\tau_{s1}+\tau_{d1}\right)\end{bmatrix}\cos^{12}\left[\frac{c\pi\left(t+\tau_{s1}\right)}{d\sin\theta}\right]\right\} \tag{4.45}$$

Numerical results of sum and difference signals for a monopulse receiver consisting of ridge-horns with $\cos^{12}$ aperture function are compared with the measured signals in Figures 4.8 and 4.9. The sum and difference signals, as shown in Figures 4.8 and 4.9, are cross-correlated with the reference signals (4.31), (4.34) and (4.35) to generate the monopulse output signals. As seen from the monopulse receiver in Figure 4.3, the monopulse output signals are constant voltage values that correspond to a particular target angle. The angle-dependent monopulse values for θ from −20° to 20° are shown in Figure 4.10 (line), for sum channel, and Figure 4.11 (line), for difference channel. Both Figures 4.10 and 4.11 show that the theoretical monopulse output voltages based on the rectangular aperture function (dotted line) and the $\cos^{12}$ aperture function (dashed line).

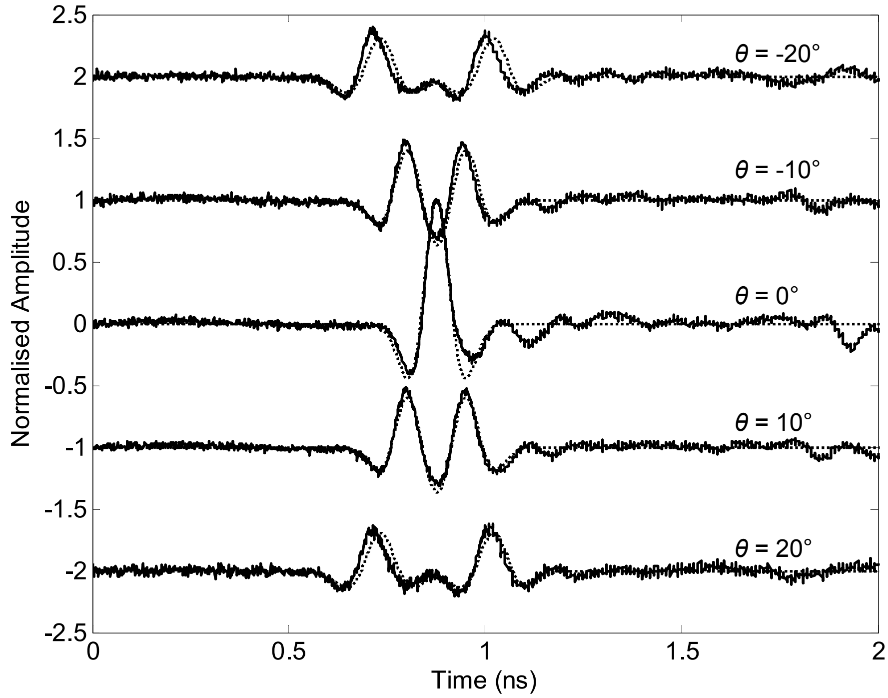

Figure 4.8: Comparison between simulated (dotted line) and measured (line) sum signals for $\theta = -20°, -10°, 0°, 10°$ and $20°$.

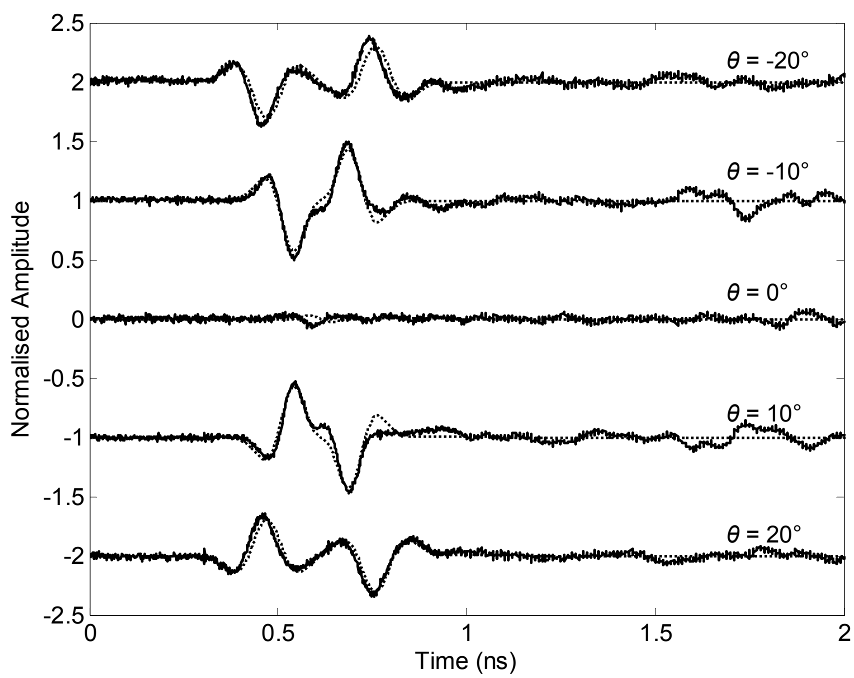

Figure 4.9: Comparison between simulated (dotted line) and measured (line) difference signals for $\theta = -20°, -10°, 0°, 10°$ and $20°$.

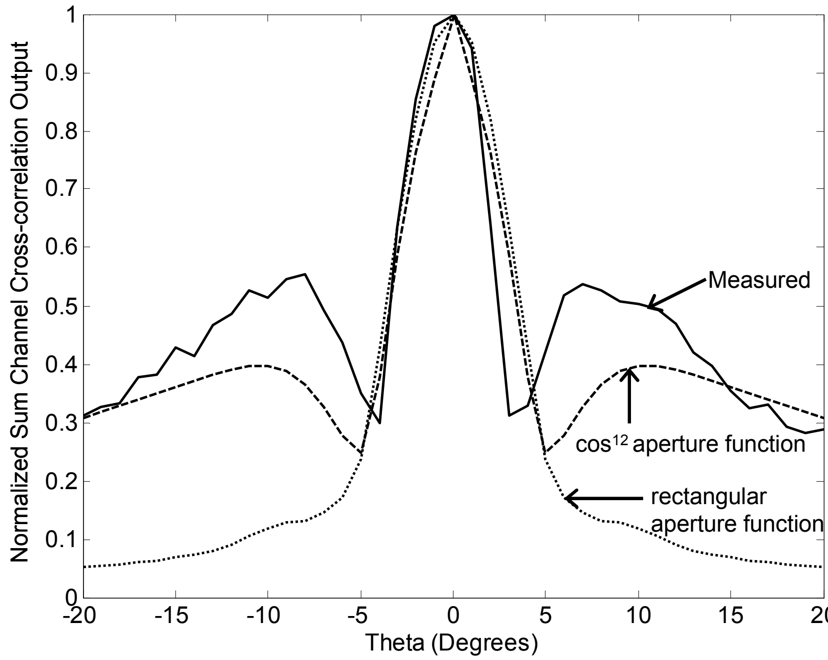

Figure 4.10: Theoretical and measured (line) monopulse sum channel cross-correlation output. The theoretical monopulse sum outputs are calculated based on rectangular aperture function (dotted line) and $\cos^{12}$ aperture function (dashed line).

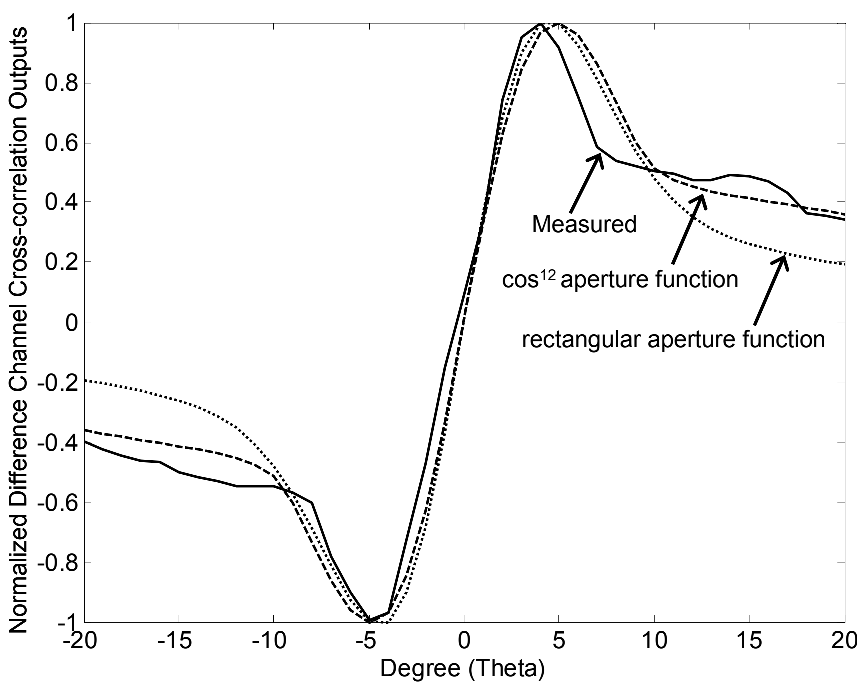

Figure 4.11: Theoretical and measured monopulse difference channel cross-correlation output. The theoretical monopulse sum outputs are calculated based on rectangular aperture function (dotted line) and $\cos^{12}$ aperture function (dashed line).

The signal used by the amplitude-comparison monopulse processor to determine the angle-of-arrival of the incident signal is the monopulse ratio, which is the ratio of $D(\theta)$ over $S(\theta)$. This ratio ensures that the monopulse processor output depends only on the incident angle, and not on the target range and radar cross-section [58]. Based on the cross-correlation outputs of the sum and azimuth difference channels that are derived with $\cos^{12}$ aperture function, the theoretical monopulse ratio is plotted (line) in Figure 4.12 and compared with measured (circles) incident signals at 1° intervals from −20° to +20°. As can be seen from Figure 4.12, the unambiguous tracking range of this monopulse radar is ± 6°. The radar's angular resolution, defined as its ability to resolve many targets [23], is dependent on array beamwidth, which is 6° in this configuration. The proposed model accurately predicts the performance of the UWB monopulse radar in terms of signal shapes, receiver patterns and the monopulse ratio.

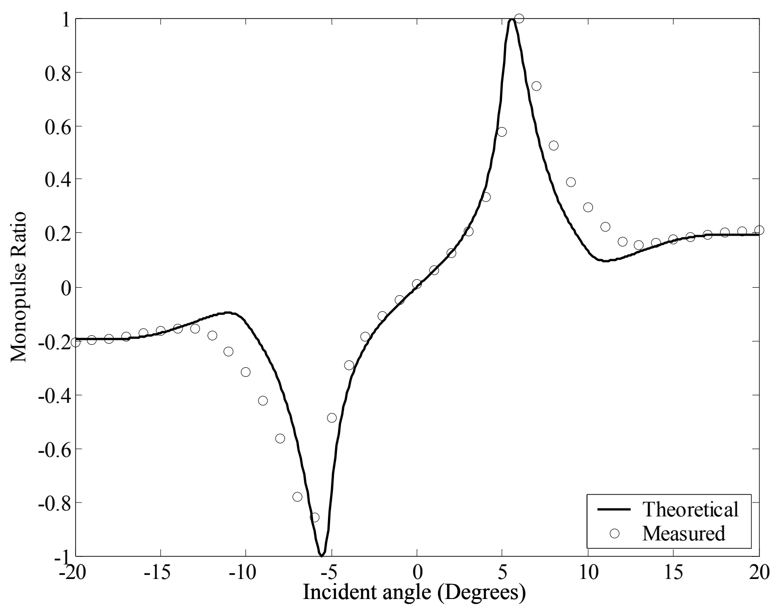

Figure 4.12: Comparison between theoretical (line) and measured (circles) monopulse ratio. The theoretical (line) monopulse ratio is derived based on ridged-horn aperture functions that are defined by $\cos^{12}$ functions.

The effects of antenna configuration and received signal shape on the Monopulse ratio are studied. In the first study, the aperture size of the individual horns is increased, and the effect of this variation to the Monopulse ratio is plotted out in Fig. 4.13. The net effect of increasing the aperture size of the individual horns of the Monopulse square-feed array is that the directivity of both the sum and difference modes of the array has increased, because the directivity of its constituent horns has increased. As shown in Fig. 4.14, the angular range and accuracy of the Monopulse tracking is changed when this happens – with increased directivity of the individual horns, the angular range of the Monopulse tracking is reduced, while the accuracy of the tracking is increased. This variation of Monopulse tracking performance can be utilized by the transceiver designer to design either a highly accurate tracking Monopulse receiver, or a large angular range tracking Monopulse receiver with a decreased tracking accuracy.

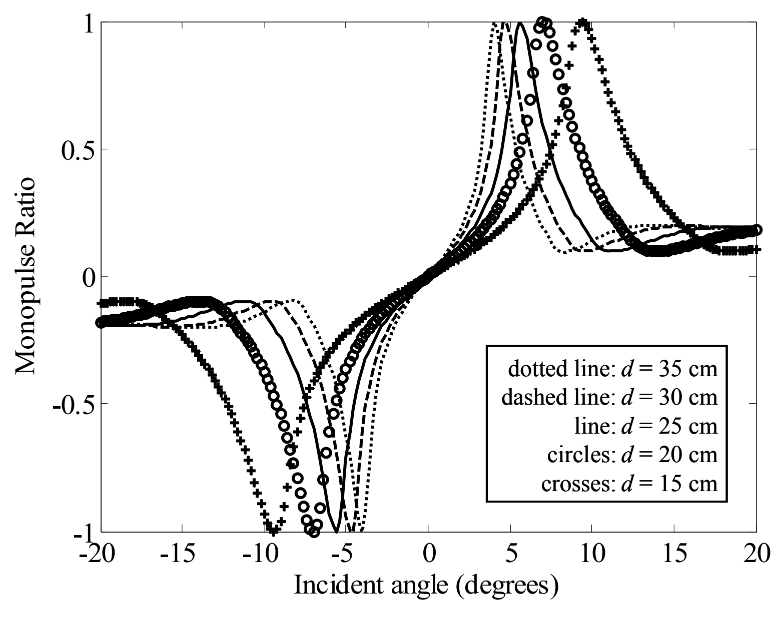

Figure 4.13: The effect of the antenna aperture length on the Monopulse ratio and the performance of the Monopulse tracking receiver.

In the second study, the pulse-width of the incident signal is varied, and its effect on the Monopulse ratio is observed in Fig. 4.14. The net effect of reducing the pulse-width of the incident signal is to increase the frequency component of the incident signal. As can be observed from Fig. 4.14, reducing the pulse-width of the incident signal increases the angle accuracy of the Monopulse receiver while it also narrows the angular range of the Monopulse ratio.

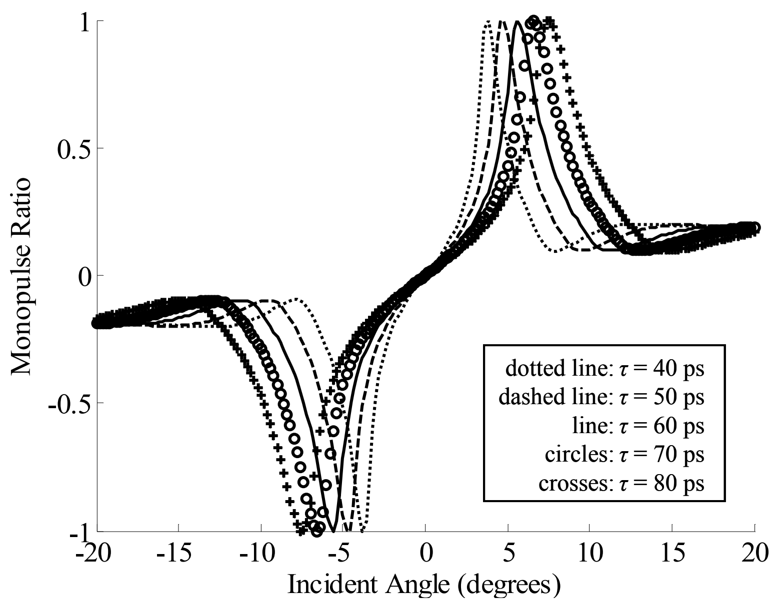

Figure 4.14: The effect of the incident signal's pulse-width on the Monopulse ratio and the performance of the Monopulse tracking receiver.

4.5 Antenna Noise Effect on Receiver

Let the output of the monopulse comparator circuit in Figure 4.3 be corrupted by additive thermal noise due to the antenna noise of the antennas of the monopulse array [10]. Let the noise corrupted sum and azimuth difference signals be modeled as $r_{sn}(t)$ and $r_{dan}(t)$, where

$$r_{sn}(t) = e(t-\tau_0) \otimes f_s(t) + n(t,\sigma) \tag{4.46}$$

$$r_{dan}(t) = e(t-\tau_0) \otimes f_{ad}(t) + n(t,\sigma) \tag{4.47}$$

τ_0 is the true time-of-arrival of the incident signal, e (t). f_s (t) and f_{ad} (t) are the impulse responses of the monopulse array in sum and azimuth channels defined in (4.44) and (4.45) respectively. n (t) is the antenna noise, modeled as Additive White Gaussian Noise of energy σ^2. Similar to the noise analysis in Chapter 3, σ^2 is related to N_0 and antenna temperature, T_{ant} as $\sigma^2 = N_0 = kT_{ant}$, where k is the Boltzmann's constant. The time-of-arrival of the signals is estimated from the sum channel waveform, r_{sn} (t). Similar to the derivations in (3.7)−(3.18), assuming that the ratio of sum channel signal energy to noise energy is much greater than 1, *i.e.* $E_s(\theta) / N_0 >> 1$, the estimated time-of-arrival of r_{sn} (t) can be approximated to be

$$\hat{\tau}_0 \sim N\left\{\tau_0, \quad N_0 \middle/ \left[E_s(\theta)\beta_s^2(\theta)\right]\right\} \tag{4.48}$$

$E_s(\theta)$ and $\beta_s^2(\theta)$ can be expressed as

$$E_s(\theta) = \int_0^T \left[e(t) \otimes f_s(t,\theta)\right] r_{s0}(t)\,dt \tag{4.49}$$

$$\beta_s^2(\theta) E(\theta) = \int_0^T \left[e(t) \otimes f_{ad}(t,\theta)\right] \frac{d^2}{dt^2} r_{s0}(t)\,dt \tag{4.50}$$

Measurements of received monopulse sum signal, for $\theta = -5°$ to $5°$ in $1°$ intervals, have been conducted to verify the standard deviation of theoretical time-of-arrival, as predicted in (4.48). For each angle, 50 sets of received monopulse sum signal have been measured in accordance to the measurement setup described in Section 3.5. The measurement of received signals is performed for one SNR levels. The measured sum signals have been cross-correlated with the sum channel reference signal, r_{s0} (t), to find the estimated time-of-arrival, $\hat{\tau}_0$. The thermal noise signal that is corrupting the monopulse sum signal has also been measured, and the mean noise power per bandwidth is found to be N_0 = 6.2e-19 J.

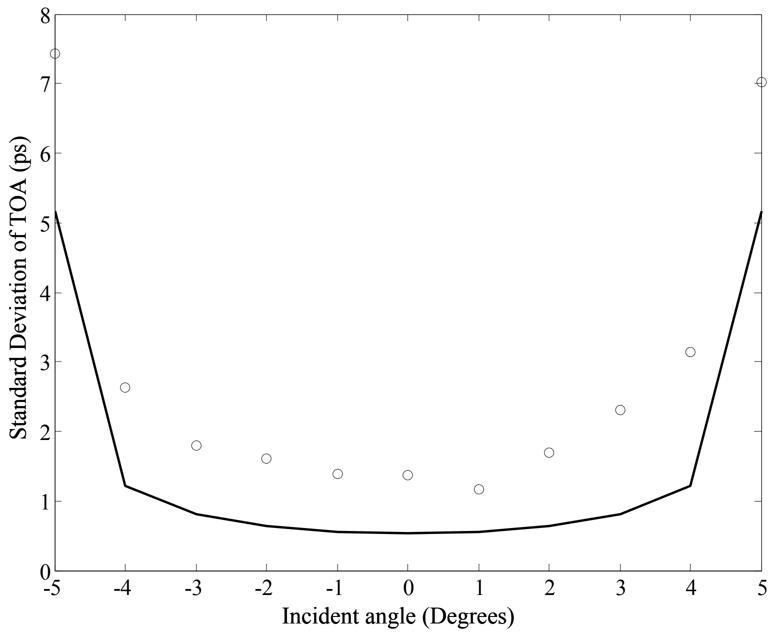

Figure 4.15: Comparison between theoretical (line) and measured (circles) standard deviations of time-of-arrival (TOA) for different angles.

To find the energy of the noiseless received signal at boresight, E_s (θ = 0°), the sum signal is averaged 4096 times to suppress the noise contribution. The measured E_s (θ = 0°) is 4.4e-16 J for a received signal amplitude of 2.8 mV. Hence, the signal-to-noise ratios (SNR) at which the monopulse receiver is experimented upon is +28.5 dB. Figure 4.13 shows the comparison between theoretical (line) and measured (circle) standard deviations of estimated time-of-arrivals for the case where the SNR is +28.5 dB. From Figure 4.15, it can be observed that the measured standard deviations of TOA for all measured angles are close to the theoretical standard deviations.

The monopulse radar finds the angle-of-arrival of the incident signal by finding the monopulse ratio, as shown in Figure 4.12. The process of estimating the monopulse ratio, however, involves finding the time-of-arrival of the sum signal first. As shown above, the time-of-arrival of the sum signal follows the probability density function of (4.40). Hence, the probability density function of the monopulse ratio, $\hat{R}$, can be expressed as

$$\hat{R} = \frac{\hat{D}}{\hat{S}} = \frac{v_d\left(\hat{\tau}_0,\theta\right) + w_d\left(\hat{\tau}_0\right)}{v_s\left(\hat{\tau}_0,\theta\right) + w_s\left(\hat{\tau}_0\right)} \tag{4.51}$$

where

$$v_s\left(\hat{\tau}_0,\theta\right) = \int_0^T \left[r\left(t-\tau_0\right) \otimes f_s\left(t\right)\right] r_{s0}\left(t-\hat{\tau}_0\right) dt \tag{4.52}$$

$$w_s\left(\hat{\tau}_0,\sigma\right) = \int_0^T n\left(t,\sigma\right) r_{s0}\left(t-\hat{\tau}_0\right) dt \tag{4.53}$$

$$v_d\left(\hat{\tau}_0,\theta\right) = \int_0^T \left[r\left(t-\tau_0\right) \otimes f_{ad}\left(t\right)\right] r_{da}\left(t-\hat{\tau}_0\right) dt \tag{4.54}$$

$$w_d\left(\hat{\tau}_0,\sigma\right) = \int_0^T n\left(t,\sigma\right) r_{da0}\left(t-\hat{\tau}_0\right) dt \tag{4.55}$$

Applying similar method of derivation as Section 3.3, functions v_s and v_d are expanded about τ_0 with Taylor expansion and only the first three terms are retained,

$$v_s\left(\hat{\tau}_0,\theta\right) \simeq E_s\left(\theta\right) \cdot \left[1 - \beta_s^2\left(\theta\right) \hat{\tau}_0^2 / 2\right] \tag{4.56}$$

$$v_d\left(\hat{\tau}_0,\theta\right) \simeq E_d\left(\theta\right) \cdot \left[1 - \beta_d^2\left(\theta\right) \hat{\tau}_0^2 / 2\right] \tag{4.57}$$

where $\hat{\tau}_0$ is the probability density function of the estimated time-of-arrival, defined in (4.48). $E_s\ (\theta)$ and $\beta_s^2\ (\theta)$ are defined in (4.49) and (4.50), and $E_d\ (\theta)$ and $\beta_d^2\ (\theta)$ are

$$E_d(\theta) = \int_T \left[e(t) \otimes f_{ad}(t,\theta) \right] r_{da0}(t)\, dt \tag{4.58}$$

$$\beta_d^{\,2}(\theta) E_d(\theta) = \int_T \left[e(t) \otimes f_{ad}(t,\theta) \right] \frac{d^2}{dt^2} r_{da0}(t)\, dt \tag{4.59}$$

Functions w_s (4.53) and w_d (4.55) are weighted average n (t), and therefore has a Gaussian distribution of zero mean [10]. The variance of w_s (τ) and w_d (τ) can be found by sampling analysis. Taking an arbitrarily small value of Δt as the lower sampling time limit, w_s (τ) and w_d (τ) can be rewritten as

$$w_s = \Delta t \sum_{i=1}^{T/\Delta t} n_i r_{s0i} \tag{4.60}$$

$$w_d = \Delta t \sum_{i=1}^{T/\Delta t} n_i r_{da0i} \tag{4.61}$$

where r_{s0i} and r_{da0i} are samples of r_{s0} ($t - \tau$) and r_{da0} ($t - \tau$) respectively. Each sample of n_i has a variance of N_0 / Δt. Since all n_i samples are statistically independent, the total variance is the sum of the variances of each sample,

$$\overline{w}_s^{\,2} = (\Delta t)^2 \sum_{i=1}^{T/\Delta t} \frac{N_0}{\Delta t} r_{s0i}^{\,2} = N_0 E_{rs} \tag{4.62}$$

$$\overline{w}_d^{\,2} = (\Delta t)^2 \sum_{i=1}^{T/\Delta t} \frac{N_0}{\Delta t} r_{da0i}^{\,2} = N_0 E_{rd} \tag{4.63}$$

where E_{rs} and E_{rd} are the energy of the reference signals for the sum and difference channel. Hence, w_s and w_d are derived as

$$w_s \sim N\left(0, N_0 E_{rs}\right) \tag{4.64}$$

$$w_d \sim N\left(0, N_0 E_{rd}\right) \tag{4.65}$$

Comparing the variances between the random variables in the numerator of (4.51), we find that if $E_s(\theta) >> N_0$, variance of w_d is much greater than variance of v_d. Comparing the variances between the random variables in the denominator of (4.51), we can find that under same condition of $E_s(\theta) >> N_0$, variance of w_s is much greater than variance of v_s. Thus, error contributions by v_s and v_d can be neglected. Hence, $\hat{R}$ can be rewritten as

$$\hat{R} = \frac{E_d\left(\theta\right) + w_d}{E_s\left(\theta\right) + w_s} \tag{4.66}$$

The probability density function of estimated angle-of-arrival, $\hat{\theta}$, can be obtained by dividing the estimated monopulse ratio, $\hat{R}$, with the true monopulse ratio in Figure 4.12, and then multiplying with the true angle-of-arrival,

$$\hat{\theta} = \theta \frac{E_s\left(\theta\right)}{E_d\left(\theta\right)} \hat{R} = \theta \frac{1 + w_d / E_d\left(\theta\right)}{1 + w_s / E_s\left(\theta\right)} \tag{4.67}$$

Equation (4.67) is a ratio of two independent random variables, which is difficult to resolve. Further simplification can be done by approximating the denominator of (4.67) to one, since

$$\operatorname{var}\left[w_s / E_s\left(\theta\right) \right] = N_0 E\left(\theta = 0\right) / E\left(\theta\right)^2 \ll 1 \tag{4.68}$$

The error contribution of the random variable at the denominator is neglected. Hence, the estimated angle-of-arrival is approximately

$$\hat{\theta} \simeq \theta\left[1 + w_d / E_d(\theta)\right] \tag{4.69}$$

Thus, the standard deviation (root-mean-square error) of angle estimate for the proposed monopulse radar is derived from (4.69) as

$$\sigma_{\hat{\theta}} \simeq \theta\sqrt{N_0 E_{rd}} / E_d(\theta) \tag{4.70}$$

In Figure 4.16, the standard deviations of estimated angle-of-arrival, as derived in (4.70), are calculated and then compared with angle-of-arrival measurements for the angles −5° to +5°. In the measurement, the same receiver setup in Section 4.4 is used. A UWB signal source is placed in far-field distance, transmitting signal in a power levels similar to the case above where the SNR is +28.5 dB. 50 sets of sum and difference signals are measured for each angle, where the monopulse ratio and the angle-of-arrival are estimated from each of the measured signals. The standard deviation of the angle-of-arrival accuracy is then calculated from the values of the 50 measured samples. Figure 4.16 shows the theoretical and measured standard deviation of angle-of-arrival accuracy of the monopulse receiver for the case when SNR = +28.5 dB. The theoretical standard deviations are less than measurements because of the approximations applied underestimate the errors. Figure 4.16 shows a significant rise in error at angles near boresight because the receiver is unable to decide whether the monopulse processor output is from left-hand-side of the antenna, or the right-hand-side.

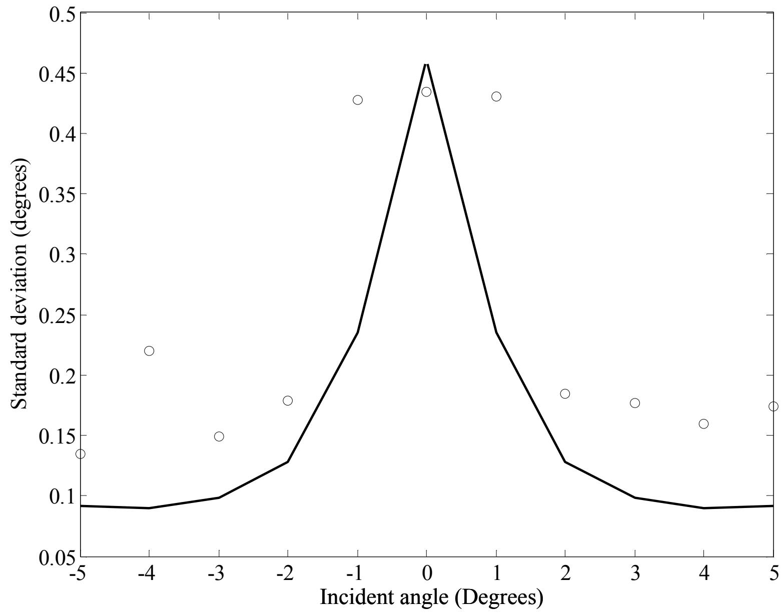

Figure 4.16: Theoretical (line) and measured (circles) standard deviations of angle error for E_b / N_0 of 28.5 dB.

4.6 Chapter Summary

In this chapter, we have proposed an amplitude-comparison monopulse receiver for ultra-wideband (UWB) receivers. The receiver captures the incident signal with a square-feed array of four ridged-horns. Based on the aperture field distribution functions of the ridged-horns, we have derived the monopulse sum and difference signals. The proposed model has been evaluated with measurements, and found good agreement between measurement and theory. The angular accuracy of the monopulse receiver is also derived and verified by measurements.

CHAPTER 5

SUB-NANOSECOND PULSE FORMING NETWORK FOR UWB TRANSCEIVER

5.1 Introduction

In ultra-wideband (UWB) radio systems, the transmitter needs to generate sub-nanosecond pulses to be transmitted through the wireless channel. In a UWB radar system, the pulses are transmitted directly after the pulse generation circuit, and the scattered signal is collected by the receiver. In a UWB communication system, the generated pulses are further modulated and then transmitted through the wireless channel. The circuit that generates these pulses is generally called the pulse forming network (PFN). In this chapter, we propose a novel PFN design to generate electrical pulses in the sub-nanosecond regime, specifically for the short range UWB radar and the high data rate UWB communication systems. The proposed PFN is designed to generate pulses at pulse repetition frequency (PRF) of about 500 MHz at power levels comparable to FCC emission limit [2]. Furthermore, the proposed PFN only consumes a DC power supply of 3.3 V, 20 mA during operation. The PFN is designed in SiGe BiCMOS for the ease of circuit integration. The PFN circuit occupies a small area 0.25 mm^2, making it suitable to be incorporated into short range (< 0.3 m) UWB radars and high data rate UWB communication systems like the wireless video streaming and wireless personal area network (WPAN).

As shown in Figure 5.1, the pulse forming network (PFN) can be used in a UWB transceiver in two ways – to generate pulses in transmitter, and to generate reference signals for the cross-correlation receivers, as described in the receivers in Chapters 3–5. It is important that the PFN consumes low DC power supply, especially for portable devices, and generates pulses in sufficiently high amplitudes without the assistance of additional broadband amplifiers, so that electrical power is conserved. To meet the FCC's emission mask [2], the transmitter requires further pulse shaping on the pulse generated by the PFN. Pulse shaping can be achieved by cascading numerous PFNs to achieve higher order Gaussian-like pulses [61], cascading the PFN with bandpass filter, or using the bandpass characteristics of the transmitter antenna. A patent has been filed for this method of generating UWB pulses [61].

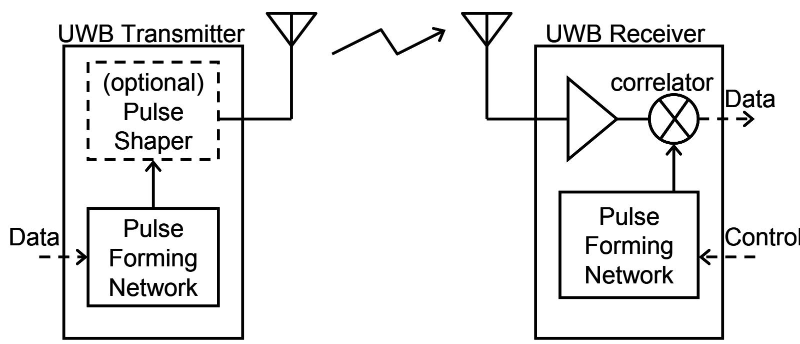

Figure 5.1: A time domain UWB transceiver using the pulse forming network in the transmitter and receiver.

In the open literature, there are many PFNs that are designed for long range UWB radars [30]−[35]. However, these PFNs are unsuitable for high data rate UWB radio systems because of different pulse repetition frequency (PRF) requirements of the latter systems. In long range UWB radars, pulses are generated at medium to high power levels, *i.e.* watts to kilowatts, and at relatively low PRF, *i.e.* few kHz to tens of MHz [41]. In UWB radios [6], [42], and some high pulse rate UWB radar systems, however, pulses are generated at lower power levels and at higher PRF. UWB radios may require PRF to be in the order of several hundred MHz to GHz, for high data rate transmission in hundreds of Mbps to Gbps. UWB radars may require PRF to be in the order of several MHz to several hundred of MHz. Furthermore, a UWB radio system needs to be implemented in silicon integrated circuit to be economical in volume production. Pulse forming methods for long range UWB radars require specialized components like Step-Recovery Diodes [39], [40], avalanche transistors, non-linear transmission lines [37] *etc*. which are not amenable to implementation in silicon integrated circuit.

An alternative and popular method for generating pulses for high data rate UWB radio can be found in [3]. In this method, a differential clock signal is used as source signal. One of the differential signal pair is fed into more delay buffers than the other, creating two single ended clock signals of different delays. The two single ended signals are then combined using an exclusive OR gate to form a sub-nanosecond pulse.

This chapter describes the theory, design, fabrication and measurement of our proposed pulse forming network (PFN). Section 5.2 presents the theory and schematic design of the PFN circuit. Section 5.3 presents the layout design, fabrication and measurement methodology of the fabricated circuit. Finally, Section 5.4 presents the experimental results and compares them with theoretical and simulated results.

5.2 Schematic Design of the Pulse Forming Network

In this section, we will present the schematic design of the pulse forming network (PFN). It is necessary to determine the required system specification. 5.2.1 presents two intended applications of the PFN and the PFN's system specification. Next, in 5.2.2 and 5.2.3, the PFN is designed based on the stated system specifications. The PFN is designed based on the strategy of performing time derivative on an input step signal. In 5.2.2, we will present a circuit that enhances the input step signal so that the characteristics of the PFN's output pulses do not deteriorate with input signal deterioration.

In 5.2.3, we present the design of a transistor-base differentiation circuit that generates the pulses for the PFN.

5.2.1 System Requirement of the Pulse Forming Network

In this section, we will find the required system specification of the PFN based on the intended applications. To do so, we need to first look into the requirements of a transceiver system that incorporates the proposed PFN to transmits data at 500 MHz PRF. A possible high data rate application is the UWB video streaming from set-up box to High-Definition Television (HDTV) and speakers for home entertainment system. The radio system required for this video streaming application is a UWB transmitter with directional antenna, placed at the set-up box, to transmit video data to a UWB receiver that is placed at the HDTV.

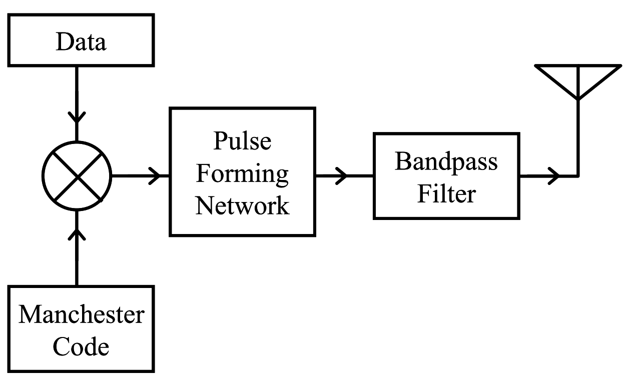

Figure 5.2: Schematic diagram of a time domain UWB transmitter using the pulse forming network.

A possible transmitter design for the above application is shown in Figure 5.2. The transmitter first codes the data with Manchester coding, and then generates the sub-nanosecond UWB pulses from the digital coded data signal. The output pulses from the PFN are shaped by a bandpass filter to meet FCC limit on the transmitter's EIRP [2] of −41.25 dBm/MHz from 3.1 – 10.5 GHz, and then transmit the signal with a directional antenna [4]. Directional antenna is used here, instead of omnidirectional antenna, because it is more suitable for the directional wireless data transmission from the set-up box to the HDTV. Multiple directional antennas have also been used for transmitter diversity to enhance wireless performance. It is assumed that antenna gain of 7 dBi is used for directional coverage in video streaming applications. It is also assumed that there is a 3 dB insertion loss between the connection from the PFN's output to antenna input. With these assumptions, it can be calculated that the required output power spectral density of the PFN needs to be −44.25 dBm/MHz from 3.1 to 10.5 GHz.

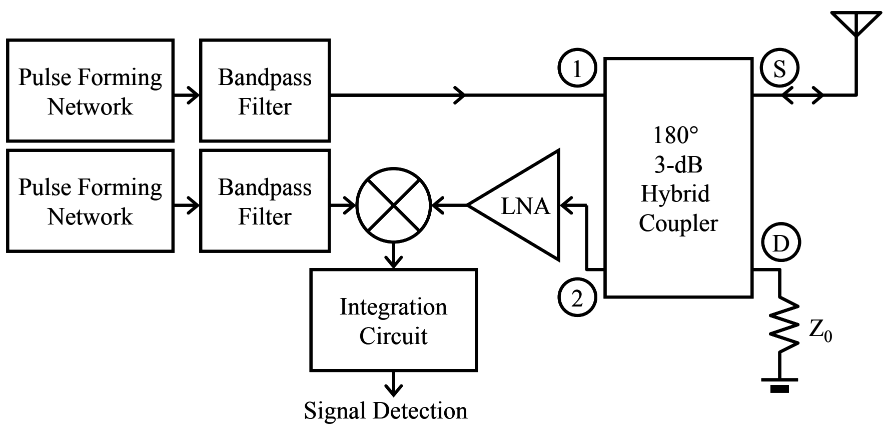

Figure 5.3: Schematic diagram of a time domain UWB radar using the pulse forming network.

Another possible application of the PFN is in short range (< 0.3 m) UWB radars. Figure 5.3 shows the transceiver architecture of a short range radar with single transmit/receive antenna. The pulse forming is used as a signal source to be fed to port 1 of the 180° hybrid coupler through a bandpass filter that pulse shapes the PFN output. The hybrid coupler acts as duplexer between the transmitter (port 1) and the receiver (port 2) of the radar. The antenna is connected to the sum port (port 'S'), and a directional antenna is used as both transmit and receive antenna. A matched load (Z_0 = 50 Ω) is connected at the difference port (port 'D') to ensure no signal from the transmitter chain (port 2) is leaked to the receiver chain (port 3). The received signal from the antenna is coupled to port 2 of the hybrid coupler with 3-dB loss. The signal is amplified with a low noise amplifier (LNA) and then cross-correlated with a reference signal, which is generated by another PFN, and pulse shaped by a different bandpass filter. For the short range radar, we assume that the same directional antenna (~7 dBi gain) is used, and a 3 dB loss between the output of the PFN to the input of the antenna. Hence, the requirement for the PFN used in the radar is the same as that of the wireless HDTV transmitter.

It can be shown, by simulation, that for a Gaussian-shaped pulse with 175 ps pulse width, to achieve the output power spectral density of −44.25 dBm/MHz, the pulse should have an amplitude of 0.15 V and a PRF of 500 MHz. The output Gaussian-shaped pulse train, however, contains spectral components at frequencies below 3.1 GHz which are undesirable for transmission. These spectral components can be filtered out by pulse shaping the PFN's output with any of the methods described in Section 5.1. Hence, the system requirement for the PFN is to generate an output Gaussian-shape pulse with 175 ps pulse width, 0.15 V amplitude and 500 MHz PRF.

5.2.2 Input Signal Enhancing Circuit

In this section, a circuit to enhance the input signal to the differentiator circuit will be presented. A major limitation to performing time derivative on an input digital signal is to ensure a consistent output pulse amplitude and pulse shape. This is because the input signal may have varying rise-times and fall-times and contain distortions. Distortions in input signal result in undesirable ringing signals that superimpose on the output pulse train, increasing the noise floor of the transmitted signal. Furthermore, variation in the input signal's rise time causes the output pulse to suffer from degradation of both pulse width and pulse amplitude.

To ensure that the PFN can consistently generate output pulses with sufficiently short rise-times (~200 ps), we propose that a fast switching circuit, as shown in Figure 5.4, to be inserted before the differentiation circuit to enhance the input signal. The fast switching circuit consists of a two stage bipolar junction transistor (BJT) differential pair. The operation of a differential pair is known [60].

Using 2-stages of differential pair acting as current-steering switch [71] ensures that the input clock signal is switched at the highest speed of the transistors, as long as the transistors are not in saturation during operation. This improves the rise time of the clock signal thus improving the output pulse shape consistency.

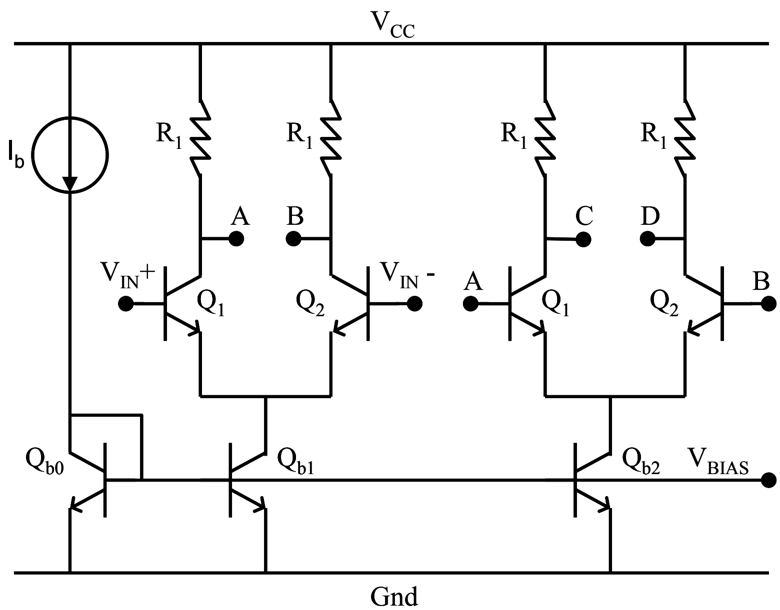

Figure 5.4: Schematic diagram of the input signal enhancing circuit.

To reduce input offset currents and voltages, precautions are taken in the circuit layout to ensure that the important components are matched to each other. For example, the resistors R_1 are clustered together in parallel with dummy resistors placed at both sides; Q_1 and Q_2 transistors are placed in close proximity, with dummies placed at the sides. The same applies to the current biasing transistors (Q_{b1}, Q_{b2} and Q_{b6}).

Transient simulations are done to evaluate the rise-time improvement of the circuit shown in Figure 5.4. In the simulation, the rise-times of input and output signals are compared, as shown in Figure 5.5. An 80 ps rise time step signal produces a 30 ps rise time step. If the input rise time is slowed down by 700 ps, the output rise time only slows down by 53 ps. Figure 5.5 shows that the 2-

stage differential pair is able to reduce the input step rise-time of 800 ps to less than 100 ps, and reduce rise-time variation to 7.57%. The improvements are the same for positive and negative steps.

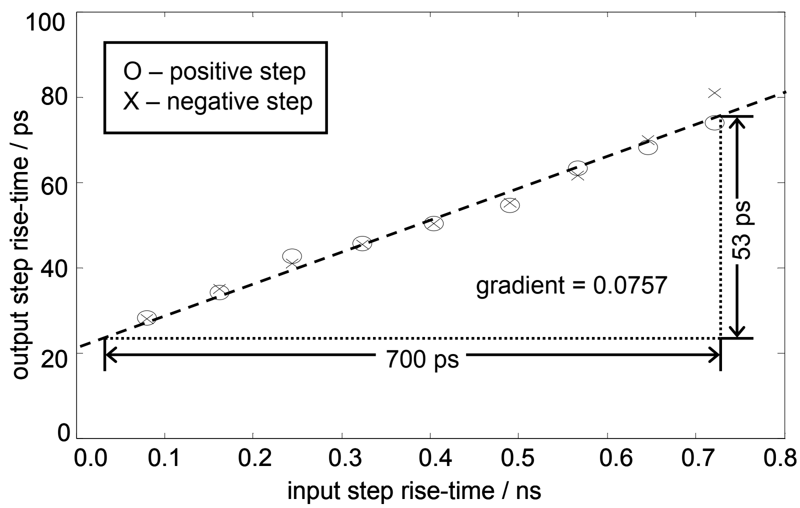

Figure 5.5: Plot of output positive step rise-time (o) and output negative slope rise-time (x) for a input step rise-time.

5.2.3 Time Derivative Circuit

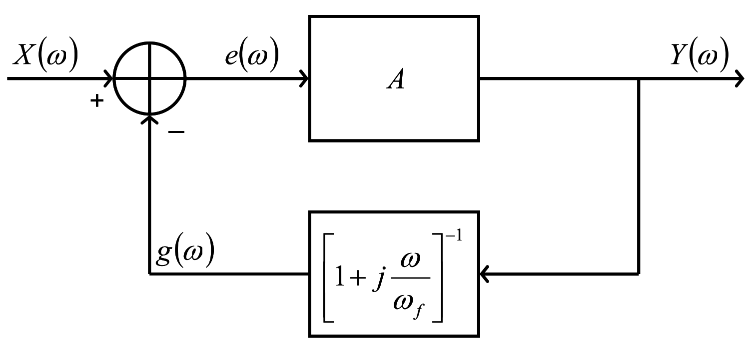

Figure 5.6: Negative feedback used to realize the differentiator block.

In this section, we will present the design of time derivative circuit, which will perform time derivative onto the input step signals to generate pulses at its output. Designing a time derivative circuit in time domain is equivalent to designing a $j\omega$ transfer function in frequency domain. One way to realize this in active circuit is to use a frequency dependent negative feedback system [49], as shown in Figure 5.6. This transfer function of a frequency dependent negative feedback is

$$\frac{Y(\omega)}{X(\omega)} = A\frac{1 + j\omega/\omega_f}{1 + A + j\omega/\omega_f} \tag{5.1}$$

Equation (5.1) can be approximated to become a differentiating function within the frequency range when $\{1 < j\omega / \omega_f < 1 + A\}$. To realize the system shown in Figure 5.6, the circuit in Figure 5.7 is used. Furthermore, by analyzing the components R_2, Q_7, Q_{b5} and C_f in Figure 5.7 in small signal, the equivalent circuit in Figure 5.8 can be arrived. Correspondingly, r_π, c_π and g_m in Figure 5.8 are the transistor parameters equivalent to the transistors Q_7 and Q_8 in Figure 5.7; r_o in Figure 5.8 is the equivalent collector-emitter resistance of the transistors Q_{b5} and Q_{b6} in Figure 5.7; C_f in Figure 5.8 is equivalent to the capacitance C_f introduced at the emitter of transistors Q_7 and Q_8 in Figure 5.7; Z_{bias} and Z_{out} in Figure 5.8 are the equivalent impedances of the input bias circuit and output impedances around transistors Q_7 and Q_8 in Figure 5.7.

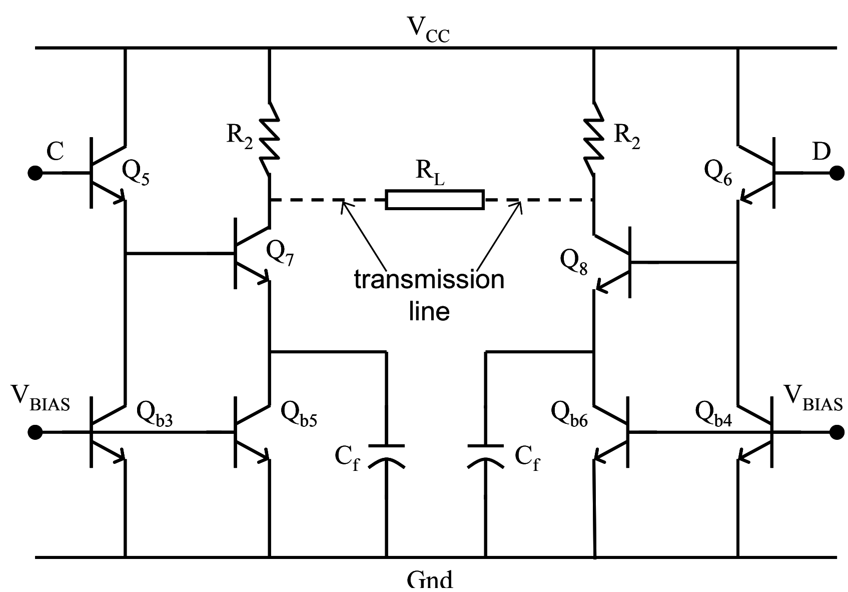

Figure 5.7: The proposed differentiator circuit.

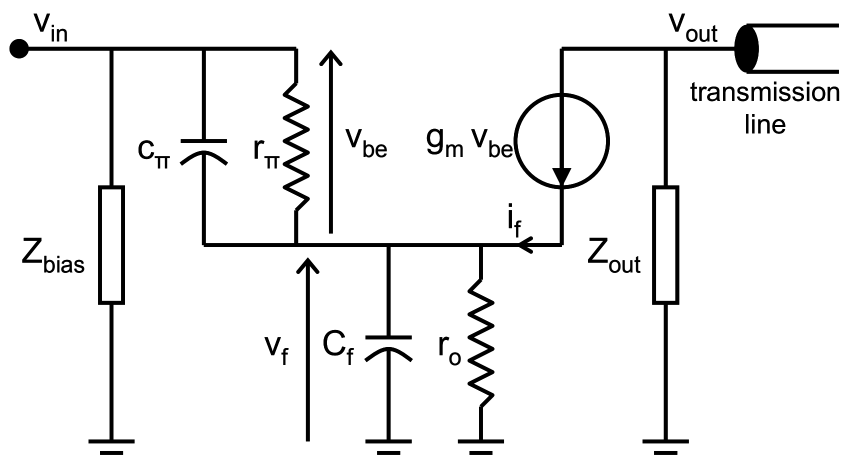

Figure 5.8: Small signal analysis of the proposed differentiator circuit.

The differentiator circuit output is connected to an external, 50 Ω load via an electrically long transmission line (Figure 5.7 – dashed line; Figure 5.8 – transmission line). The relationship between output voltage, v_o, and input voltage, v_i, of Figure 5.8 are shown in (2).

$$\frac{v_o}{v_i} = -\frac{R\left(j\omega C_f + 1/r_0\right)}{1 + 1/g_m r_\pi + 1/g_m r_0 + j\omega\left(C_f + C_\pi\right)/g_m} \tag{5.2}$$

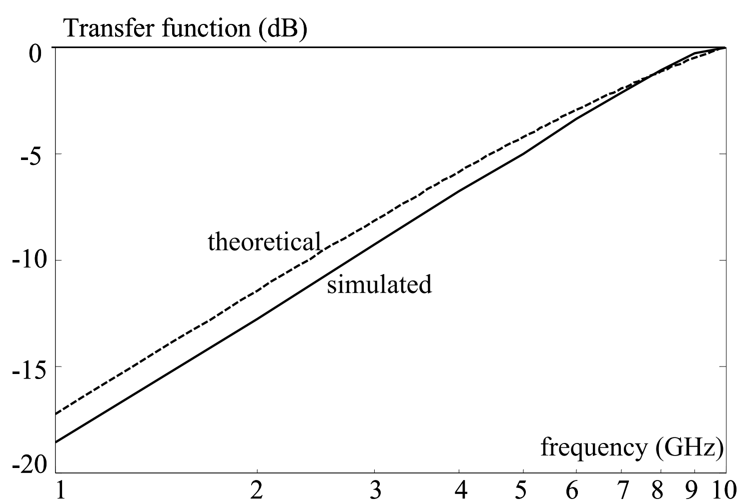

Figure 5.9: Theoretical and simulated frequency response of the differentiator circuit show a linear gain profile for frequencies 1 – 10 GHz.

Analyzing the circuit in Figure 5.7 and its equivalent circuit in Figure 5.8, we can observe that the circuit is a current-voltage (series-series) negative feedback system with current feedback i_f, feedback circuit of shunt C_f and r_o, and voltage v_f being fed back to input. Figure 5.9 compares the AC simulation of the differentiator circuit compared with (5.2). As seen in Figure 5.9, the circuit function acts as a differentiator in the frequency range from 1 GHz to 10 GHz. At frequencies above 10 GHz, the poles of transistors Q_7 and Q_8 begin to attenuate the output.

Negative feedback systems are potentially unstable, because additional poles in the forward block, A, in Figure 5.6 will contribute to additional phase shift to R-C regime of v_f in Figure 5.8 or g (ω) in Figure 5.6. The additional poles can potentially cause the circuit to oscillate. To check the stability of the circuit, AC simulation is done on the circuit to observe the response of v_f in Figure 5.8. Simulation result, as shown in Figure 5.10, shows that the gain variation is 1 dB at 10 GHz, and phase variation is 50° at 10 GHz, showing that the system is stable.

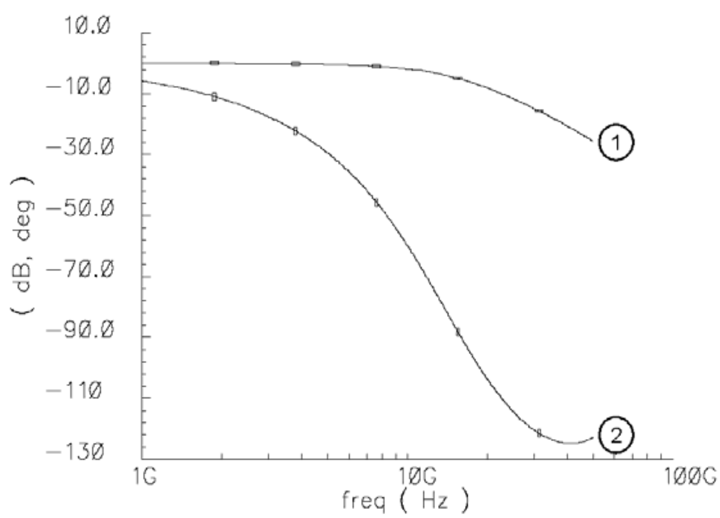

Figure 5.10: Frequency domain simulation of the feedback voltage, v_f, shows that the gain variation of v_f is less than 1 dB at 10 GHz (Trace 1), and the phase variation of v_f is less than 50° (Trace 2).

5.3 Circuit Implementation and Measurements

The pulse forming network (PFN) is fabricated with 0.25 μm SiGe BICMOS process, and packaged in ASAT Quad Flat Pack. The combined area of the input signal enhancing circuit and time derivative circuit is 0.25 mm^2 (Figure 5.11). This circuit is designed and simulated using Cadence, and fabricated in IBM SiGe BiCMOS6HP process. Figure 5.11 below show a simple schematic of the fabricated circuit. In Figure 5.4, an adjustable bias current, I_b, at Q_{b0} ensures a constant biasing voltage, V_{bias}, is applied at Q_{b1} to Q_{b6} of Figures 5.4 and 5.7. To ensure performance consistency amongst Q_{b1} to Q_{b6}, they are placed close to each other, in a row, with dummy transistors being placed at both ends. Similar layout method of placing critical components in a row and placing dummy components at both ends have been applied to the four R_1 resistors in Figure 5.4; the two R_2 resistors in Figure 5.7; the matched pairs of transistors Q_1 and Q_2 in Figure 5.4; Q_5 and Q_6 in Figure 5.7; and Q_7 and Q_8 in Figure 5.7. Q_5 and Q_6 are emitter followers that provide isolation between the signal enhancing circuit and time derivative circuit.

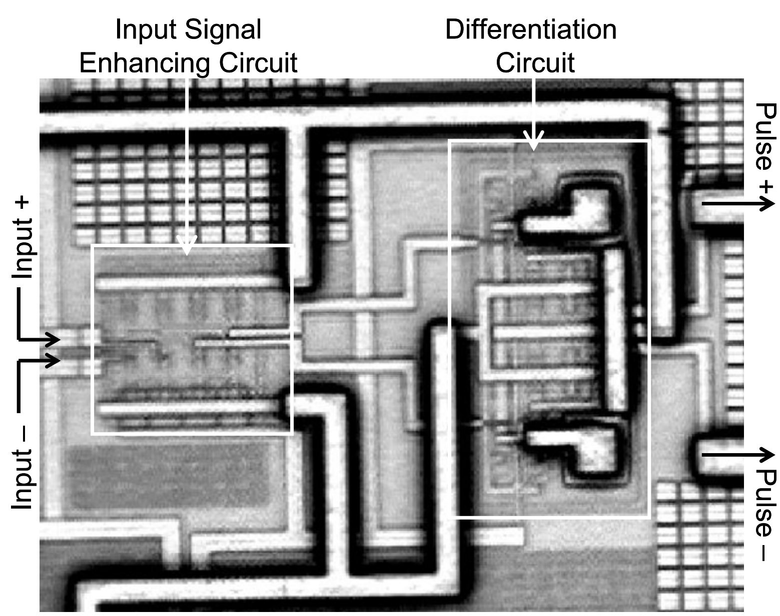

Figure 5.11: Magnified picture of the fabricated circuit.

Figure 5.11 shows the circuit's good horizontal symmetry. Two copper lines (extreme left) are the differential input signal lines. The differential input signal lines are connected to the input signal enhancing circuit; and then to the time derivative circuit. The time derivative circuit output is connected out via the two copper lines (extreme right). A PCB board is fabricated to interface the chip for measurement. It has a DC 3.3 V, 20 mA power supply, and 50 Ω microstrip lines connect the chip to differential input and output ports, as shown in Figure 5.12.

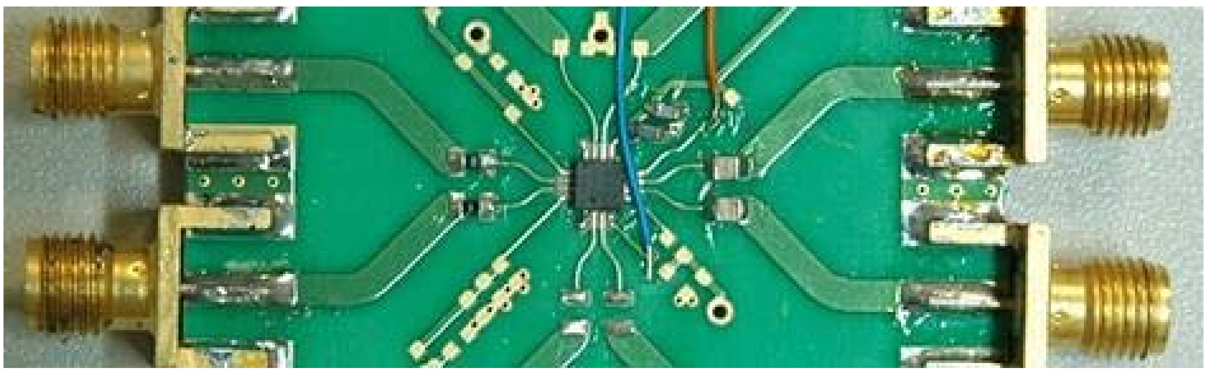

Figure 5.12: Picture of the PCB board used for testing purposes, and the IC chip.

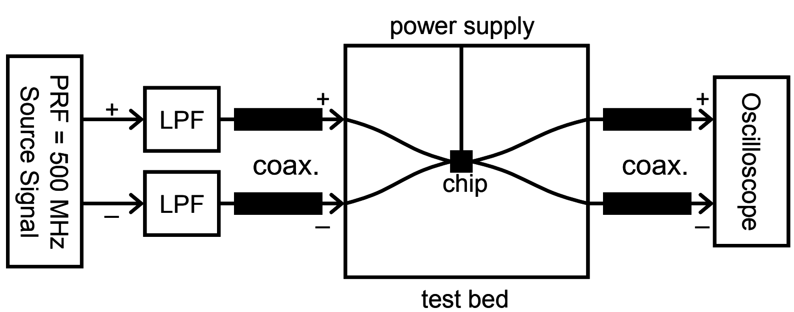

Figure 5.13: Schematics of test setup for time domain measurement of the PFN output.

Three measurements are performed to evaluate the circuit. In the first measurement, the circuit's output waveform and spectrum is measured, as shown in the measurement schematic in Figure 5.13. This is compared with theoretical and simulated result to evaluate the circuit performance. The pair of 'LPF' blocks that are placed in between the source signal and the test bed in Figure 5.13 are used to simulate input signal deterioration. In one of the time domain measurements, the input signal integrity is intentionally deteriorated by low pass filters to see its effect on the output pulse shape and pulse amplitude. In the second measurement, the circuit's output is filtered with a 2.4-5.3 GHz (10 dB bandwidth) bandpass filter, and the output waveform and spectrum is measured.

In the third measurement, the transmitter's EIRP is measured based on FCC's requirements [2]. The experimental setup to measure the transmitter's EIRP is shown in Figure 5.14. In the measurement, a 500 MHz PRF data signal source is fed into the PFN circuit. The circuit output is then cascaded with the above-mentioned bandpass filter. The output is connected directly with a 7 dBi gain TEM-horn antenna, which has a return loss of < −10 dB from 1 – 8 GHz. The transmitter and a UWB receiver are placed in the anechoic chamber at a distance 3.0 m apart. The UWB receiver consists of a receiver double-ridged horn by RCM Ltd. (model MDRH-1018) which has an average gain of 15 dBi (frequency dependent) and a return loss of < −10 dB from 1 – 18 GHz. The received UWB signal is amplified with a 26 dB gain low noise amplifier. The signal is then measured with either a sampling oscilloscope or spectrum analyzer for time and frequency domain measurements respectively. The method of calculating the transmitter's EIRP can be found from [2].

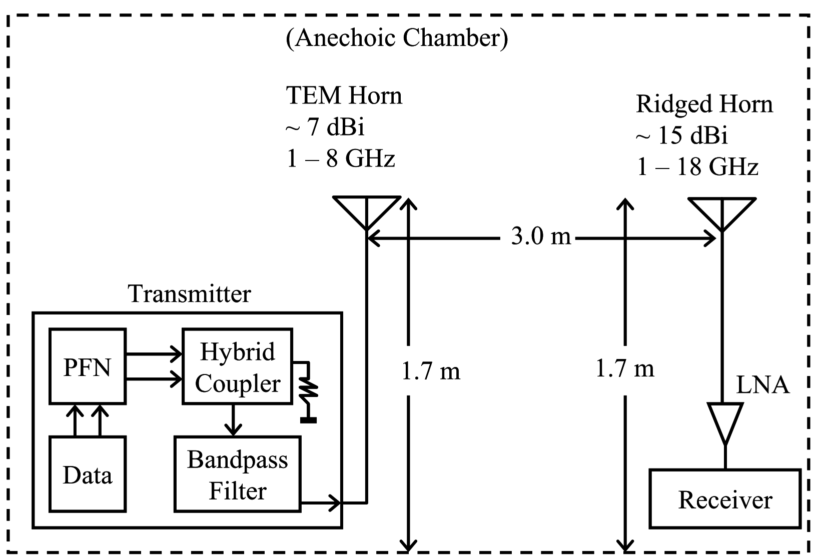

Figure 5.14: Schematic of the test setup for the EIRP measurement of a transmitter with the fabricated PFN.

5.4 Measurement Results

5.4.1 Pulse Shape

The output pulse shape is measured and compared with simulation and theory, as shown in Figure 5.15. To measure the differential signal, both ports are recorded simultaneously in a 20 GHz bandwidth sampling oscilloscope. The measured signal is the subtraction of signal of one of the ports with another. It is observed that the measured pulse width (175 ps) is longer than the simulated pulse width (150 ps); and the measured pulse amplitude (0.17 V) is higher than the simulated pulse amplitude (0.13 V).

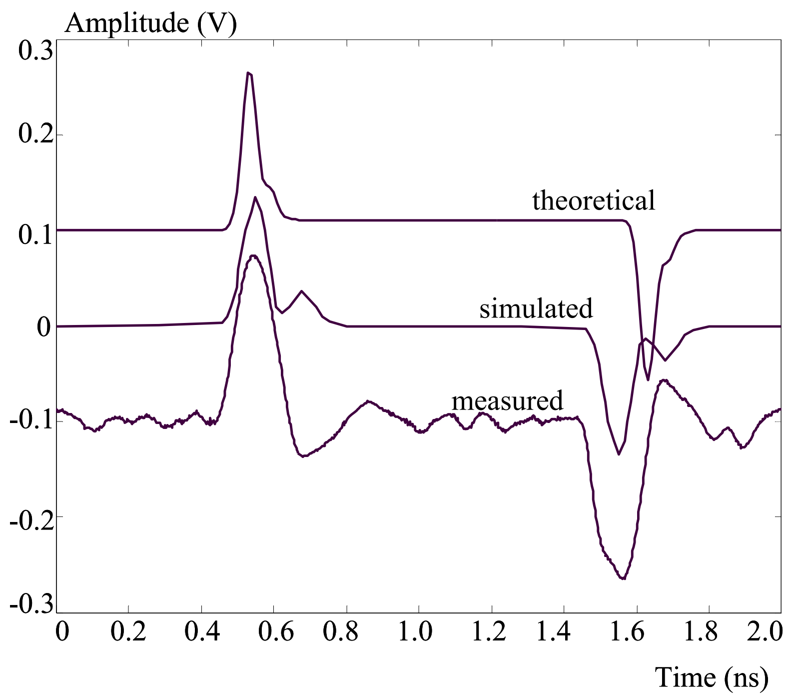

Figure 5.15: Comparison between theoretical, simulated and measured pulse shape of the PFN for an input data signal of 40 ps rise-time.

Overall, the theory, simulated and measured result coincides reasonably. The simulated waveform has slightly larger pulse width compared to the theoretical pulse width because it has considered parasitic effects of the layout. The measured waveform is slightly different from the simulated waveform because of several factors – the timing jitter of the source and the oscilloscope, the package effect of the Quat Flat Package, which is not modeled in the simulation, and the cable dispersion of the measurement setup. These factors will lengthen the measured pulse width and introduce 'ringing' at the end of the pulse.

In another measurement, the input signal is low pass filtered, increasing the rise and fall times from 40 ps to 300 ps. The output pulse amplitude decreases from 0.17 V to 0.15 V, while the output pulse width lengthens from 175 ps to 180 ps, as shown in Figure 5.16. This measurement illustrates the point that the PFN is less susceptible to rise-time variations of the input signal.

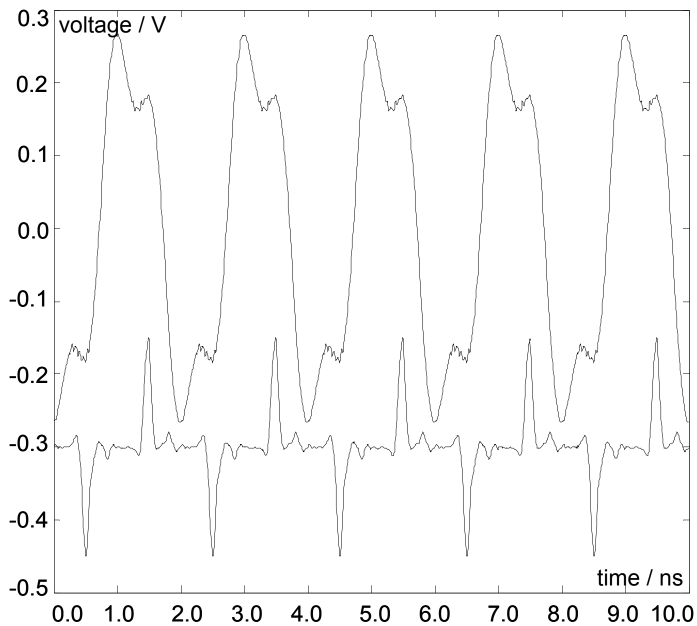

Figure 5.16: Output of the PFN when input signal is a highly distorted 500 MHz clock signal with 300 ps rise-time.

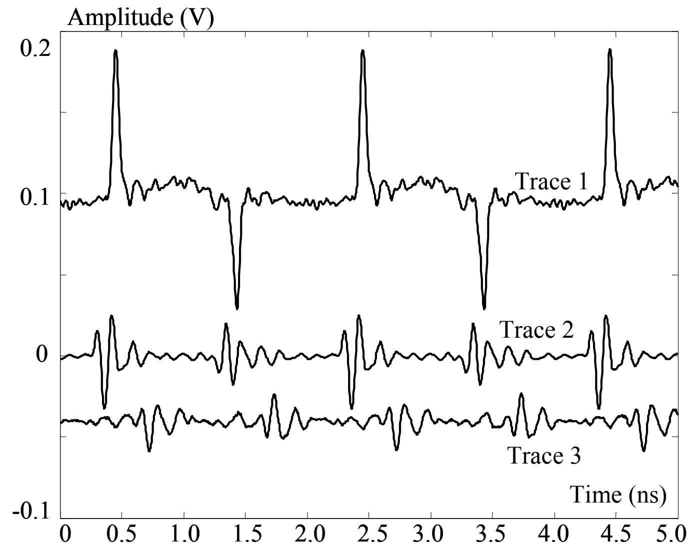

Trace 1 = Hybrid coupler's output; Trace 2 = Bandpass filter's output;
Trace 3 = Signal at the receiver
Figure 5.17: Measured time-domain signals at various stages of the transceiver system in Figure 5.14.

Figure 5.17 shows the comparison between the measured time-domain signals from different stages of the UWB transceiver in Figure 5.14. In 'Trace 1', the output signal of the hybrid coupler is shown; in 'Trace 2', the output signal of the bandpass filter is shown; and in 'Trace 3', the output signal of the receiver's low noise amplifier (LNA) is shown. The broadband coupler attenuates the peak amplitude of the pulse by 6 dB, thus causing the measured 'Trace 1' signal to have significantly lower amplitude.

5.4.2 Power Spectral Density

The transmitted pulse train of a short range UWB radar is generated by a clock signal with PRF = 500 MHz. The measured power spectral density of the PFN output pulse is shown in 5.18; the measured power spectral density of the bandpass filter output is shown in Figure 5.19; and the measured transmitter EIRP in shown in Figure 5.20. Figure 5.20 shows that the transmitted signals of the short range UWB radar is within the FCC's emission limit, where the EIRP is limited to −41.25 dBm/MHz.

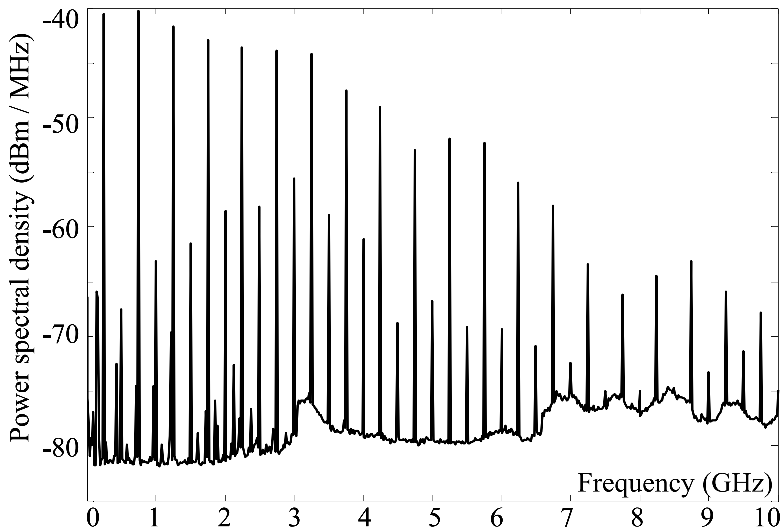

Figure 5.18: Measured spectral content of PFN output shows that it contains sufficient spectral power for UWB signal from 3.1 – 10.6 GHz.

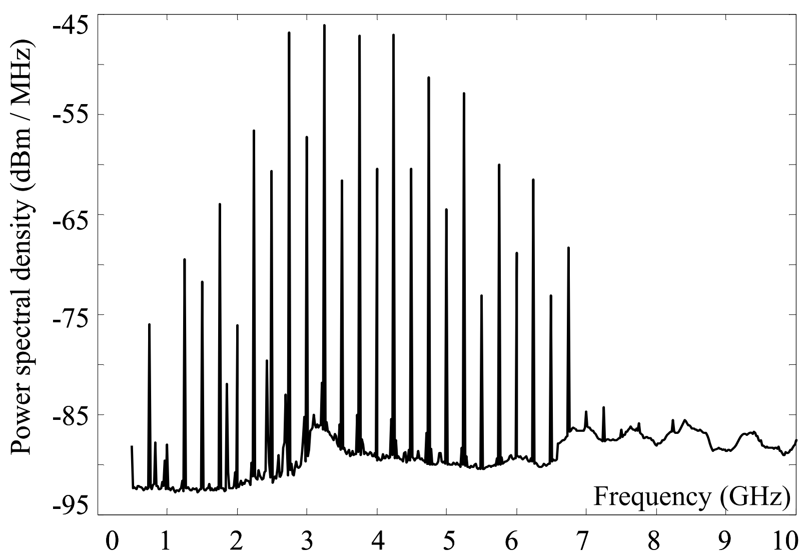

Figure 5.19: Measured spectral content of 3 – 6 GHz bandpass filtered output of the PFN.

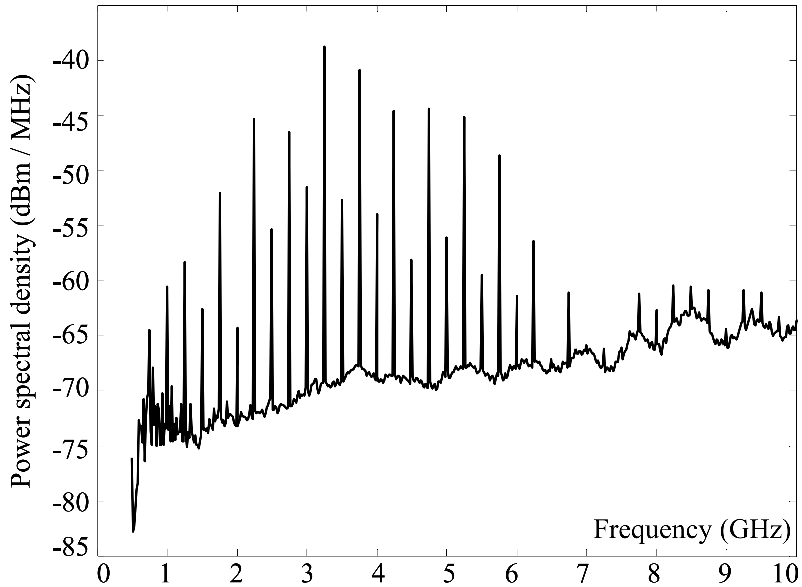

Figure 5.20: Measured EIRP of the transmitter.

To simulate the transmission of data signals, we generated Manchester coded pseudorandom bit sequence to input into the transmitter, and then measured the EIRP. The result is presented in Figure 5.21, where we show both EIRP of clock and data inputs, and compare it with the FCC EIRP mask. As shown in the figure, the EIRP of transmitter transmitting clock signal slightly exceeds the FCC EIRP limit, while that of data signal is less. The spectral content decreases at 6 GHz onwards primarily because the bandpass filter filters out higher frequency components. The low-power high frequency-components of the pulses generated by the PFN (e.g. −45 dBm/MHz at 6 GHz, −57 dBm/MHz at 9 GHz, etc.) also limit the spectral contents at these frequencies.

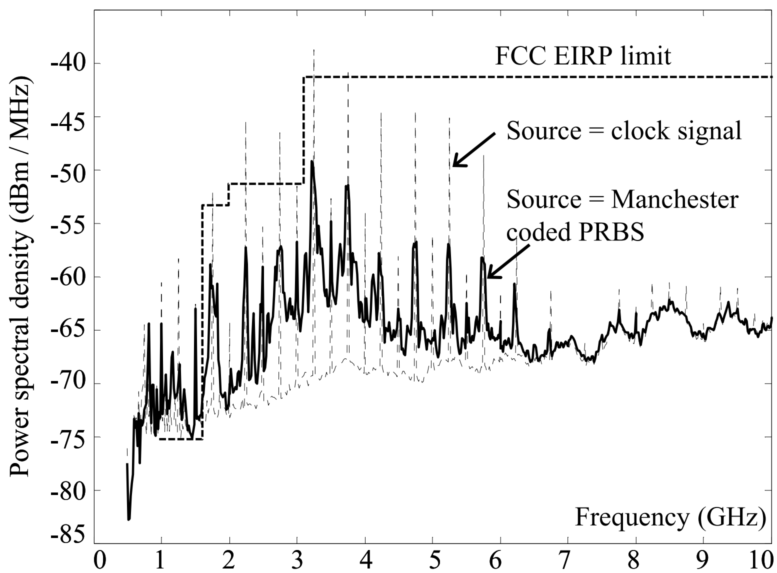

Figure 5.21: Comparison between the FCC emission limit and the measured EIRP for Manchester coded an alternate bit [1,0] sequence and a pseudo-random bit sequence.

Figure 5.15 shows that the measured amplitude of the PFN output (0.17 V) meets the system specification set in Section 5.2.1, which requires the pulse to have at least 0.15 V. Figure 5.16 shows the robustness of the PFN should the input signal is a slow and distorted input signal. Figure 5.17 shows that the time domain signal of the transmitter using the proposed PFN can be visually identified at a receiver placed 3 m away. Figure 5.21 shows that the spectral content of the PFN has sufficient power to cover the frequency range up to 10 GHz. Figure 5.21 shows that, after bandpass filtering, one can pulse shape the PFN output to transmit at frequency spectrum that are FCC complaint. It also gives an indication of the change in spectral content of the signal if we transmit PRBS instead.

5.5 Chapter Summary

A pulse forming network for high data rate UWB radio systems has been developed. The design occupied 0.25 mm^2 of an IC chip, consumed 3.3 V, 20 mA power supply. The output power is high enough in high pulse rate transceivers without additional broadband amplifier at the front-end.

Further improvements can be done to extend the pulse shaping capability of the circuit, to increase the output power of the pulse forming network, and also to use this circuit as the front-end of a single chip solution for UWB communication and radar system.

CHAPTER 6

MEASURING HUMAN BODY'S IMPULSE RESPONSE WITH ULTRA-WIDEBAND RADAR

6.1 Introduction

An ultra-wideband (UWB) radar detects a target by transmitting discrete electromagnetic pulses and receiving the scattered signal from the target [46]. The pulses transmitted by the UWB radar has a short (sub-nanosecond) pulse width, enabling the radar to estimate accurate location information of the target from the received scattered signals [1]. Furthermore, since the transmitted pulses are wideband, a UWB radar receiver is able to collect much more information from the scattered signals, as compared to narrowband radars [1]. It is reported in [47] that, because of the beneficial characteristics, UWB radar is a potential candidate for non-invasive medical monitoring and imaging tool. In [37], however, the research effort is focused on UWB radars that operate at frequencies below 1 GHz. Furthermore, many research papers in the existing literature focus on imaging techniques employing (ultra-wideband) frequency scanning radars [48]−[50] rather than emitting discrete electromagnetic pulses. On the other hand, some time-domain UWB radars have been developed [51], [52] to detect breathing and heartbeat of a person.

In this chapter, we propose a method of using UWB radar that will measure the physical and electrical properties of the human body. The proposed UWB radar finds the impulse response of the human body from the scattered signal. The radar transmits discrete second derivative Gaussian pulses of bandwidth (10 dB) 2 – 10 GHz onto the target (human body), and receives the scattered signal from the target. Many samples of the received signal are aggregated and averaged to increase the signal-to-noise ratio (SNR), and then processed to obtain the impulse response of the human body. The impulse response of the human body can be intuitively linked to the electrical and physical properties of the human body. By analyzing the impulse response, information like range, dielectric properties, and, if there is signal penetration into the internal organs, the location and dielectric properties of the organs within the human body can be determined.

In Section 6.2, the method of using UWB radar to measure the impulse response of a human body is presented. In Section 6.3, the impulse response of the human body target is derived. In Section 6.4, the human phantom construction, used as radar target, and the UWB radar design is presented. Lastly, in Section 6.5, the measured result are presented and verified with the theoretical result.

6.2 Measurement Method

In this section, we would like to present the method we propose to measure the impulse response of a human target. Firstly, we need to justify the choice of modeling the human target as an impulse response, because it is different from the more conventional choice of modeling it as a radar cross-section (RCS) [46]. The RCS is defined as the variable σ in the radar equation [46]. The RCS is a property of the scattering target, and it measures the power scattered per unit solid angle by the target in a given direction and normalized with respect to the power density of the incident field. Even when the RCS has been expanded to incorporate properties like frequency dependence and cross polarization in the scattering matrix [1], its derivation is still based on target detection and recognition. It is found that the RCS, expressed in its current form, is unsuitable for predicting the characteristics of a large radar target, like a human body placed near to the UWB radar.

It can also be argued that, since the UWB signal is discrete and short, it is possible to intuitively link the received signal waveform with the physical properties of the target, without the need to find the target impulse response. In practical UWB radars, however, this is not possible. Firstly, due to regulation restrictions on the emissions of UWB systems [2], the UWB radar is unable to transmit signals with too wide a bandwidth. These emission limitations impose restrictions on the UWB signal shapes and power levels. Hence, the transmitted signal shape maybe suboptimal for direct identification of the target properties. Secondly, the transmitter circuits, consisting of trigger circuits, pulse forming networks [59], amplifiers, couplers, transmit/receive (TR) switches and antenna causes distortions and ringing of the transmitted signal. The ringing, which occurs at the tail-end of the transmitted signal, interferes with the UWB radar receiver's ability to detect secondary reflections from the target.

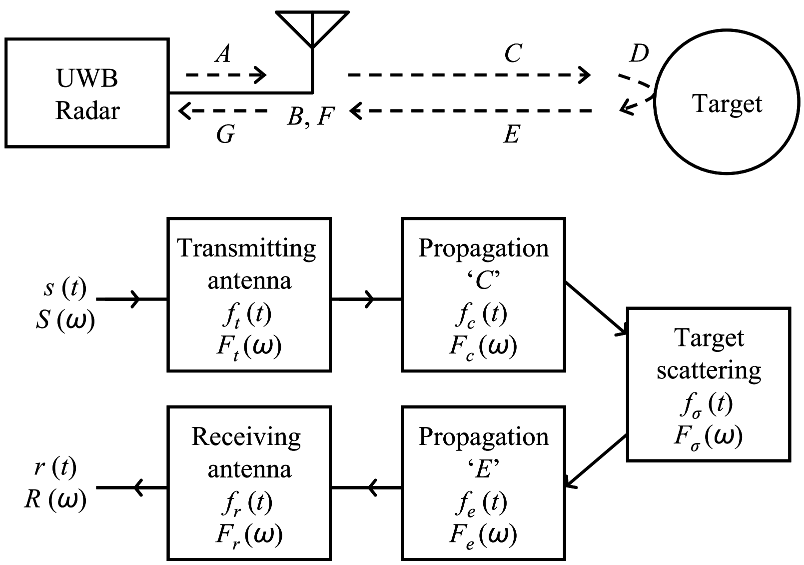

Figure 6.1: A monostatic UWB radar detecting a radar target and the linear transfer function model.

Figure 6.1 shows how a monostatic UWB radar, using the same transmitting and receiving antenna, detects a radar target. For simplicity in the analysis, let the distance between the radar and the target be known. The alphabets '*A*' to '*G*' label the arrows, showing the propagation paths of the UWB signal for one instance of radar detection. '*A*' labels the path where the UWB source signal propagates across the transmitter chain to reach the transmitting antenna. '*B*' labels the path where the

UWB source signal propagates from the input port to the radiating aperture of the antenna. '*C*' labels the path where the transmitted UWB signal propagates through air towards the target. '*D*' labels the path where part of the transmitted UWB signal is scattered, and some of the scattered signal heads back towards the radar. '*E*' labels the path where the scattered signal propagates through air, back to the UWB radar. '*G*' labels the path where the scattered signal is received by the same antenna. '*F*' labels the path where the received signal propagates across the receiver chain (*i.e*. bandpass filter, low-noise amplifier *etc*.).

Figure 6.1 also shows a linear model of the monostatic UWB radar detecting the target. Let the UWB source signal that is fed to the antenna be $s\ (t)$. The impulse response of the antenna in transmitting mode is $f_t\ (t, \theta = 0°, \varphi = 0°)$. $\theta = \varphi = 0°$ because the target is assumed to be at boresight. The propagation as described in '*C*' is modeled as impulse response $f_c\ (t)$. The scattering of the transmitted UWB signal back towards the UWB radar is modeled as impulse response $f_\sigma\ (t)$. The propagation as described in '*E*' is modeled as impulse response $f_e\ (t)$. The impulse response of the antenna in receiving mode is $f_r\ (t, \theta = 0°, \varphi = 0°)$. Let the received signal from the antenna be $r\ (t)$.

$s\ (t)$, $f_t\ (t)$, $f_c\ (t)$, $f_\sigma\ (t)$, $f_e\ (t)$, $f_r\ (t)$ and $r\ (t)$ can be Fourier transformed to frequency domain as $S\ (\omega)$, $F_t\ (\omega)$, $F_c\ (\omega)$, $F_\sigma\ (\omega)$, $F_e\ (\omega)$, $F_r\ (\omega)$ and $R\ (\omega)$ respectively. The source signal, the transfer functions and the received signal can be cascaded together as shown in Figure 6.1 to model the monostatic UWB radar detecting the target. In both time and frequency domains, the received signal is related to the source signal as

$$r(t) = s(t) \otimes f_t(t) \otimes f_c(t) \otimes f_\sigma(t) \otimes f_e(t) \otimes f_r(t) \tag{6.1}$$

$$R(\omega) = S(\omega) F_t(\omega) F_c(\omega) F_\sigma(\omega) F_e(\omega) F_r(\omega) \tag{6.2}$$

Figure 6.2 shows how a UWB radar (Receiver) receives the transmitted signal from a similar UWB radar (Transmitter) placed at a distance apart. The propagation path of the UWB signal in

Figure 6.2 is similar to that of Figure 6.1, except for the absence of a radar target to scatter the transmitted signal. The transmission process as shown in Figure 6.2 can be modeled as a cascade of impulse responses in time-domain, or transfer functions in frequency domain. Because of the similarity of propagation path as in Figure 6.1, the impulse responses from Figure 6.1 – f_t (t), f_c (t), f_e (t) and f_r (t), can be used. Furthermore, the source signal s (t) used in this transmission process is the same as that used in Figure 6.1. The received signal in the case of Figure 6.2, however, is different, and it is defined as r_0 (t).

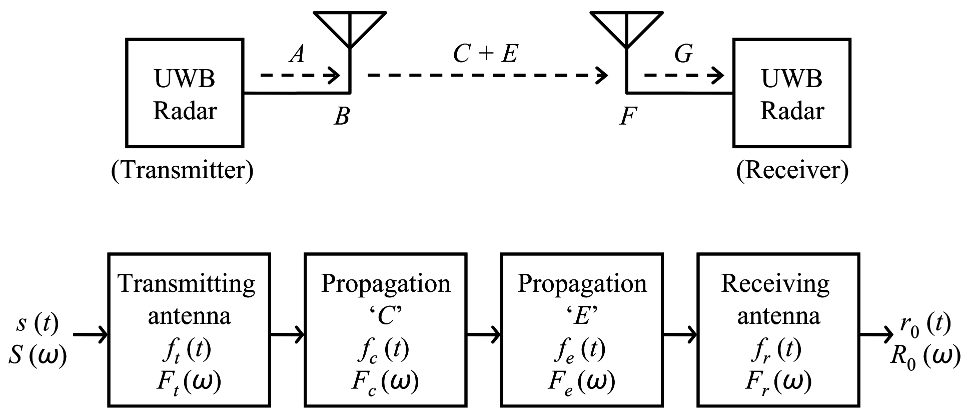

Figure 6.2: A UWB radar (Receiver) detecting a transmitted signal from a similar UWB radar (Transmitter), and the linear transfer function model.

The relationship between the received and transmitted signal in the transmission process shown in Figure 6.2 can be expressed as

$$r_0(t) = s(t) \otimes f_t(t) \otimes f_c(t) \otimes f_e(t) \otimes f_r(t) \tag{6.3}$$

$$R_0(\omega) = S(\omega) F_t(\omega) F_c(\omega) F_e(\omega) F_r(\omega) \tag{6.4}$$

in time and frequency domains respectively. Dividing (6.2) with (6.4), the transfer function of the scattering by the radar target, F_σ (ω), can be expressed as

$$F_\sigma(\omega) = R(\omega)/R_0(\omega) \tag{6.5}$$

In time domain,

$$f_\sigma(t) = \Im^{-1}\left\{\frac{\Im[r(t)]}{\Im[r_0(t)]}\right\} \tag{6.6}$$

where $\Im\{\ldots\}$ and $\Im^{-1}\{\ldots\}$ denote Fourier transform and inverse Fourier transform of the functions within the bracket. It can be seen from (6.6) that the impulse response of the radar target, f_σ (t), can be found from the time-domain waveforms of the measurements shown in Figures 6.1 and 6.2. To find f_σ (t), measurements, as shown in Figures 6.1 and 6.2, are conducted first. Then, the measured result is Fourier transformed, and result from Figure 6.1 is divided with the result from Figure 6.2. Finally, the result from the division is inverse Fourier transformed. However, r (t) and r_0 (t) are band limited signals – their out-of-band frequency components are below noise level. The out-of-band noise components contribute significant error to (6.6) because, at these frequencies, rather than being a ratio of signal, it is a ratio of random noise. To remedy this situation, frequency windowing [72] is applied on (6.6) to attenuate the contributions of the out-of-band frequencies. The frequency windowed impulse response, f_σ^w (t), can be expressed as

$$f_\sigma^w(t) = \Im^{-1}\left\{\frac{\Im[r(t)]}{\Im[r_0(t)]} W_g(\omega)\right\} \tag{6.7}$$

where W_g (ω) is the frequency window function. W_g (ω) is chosen to be a Gaussian function

$$W_g(\omega) = \exp\left(-\omega^2/\omega_c^{\ 2}\right) \tag{6.8}$$

ω_c is the frequency at which the Gaussian window W_g is −9.1 dB. ω_c can be adjusted based on the bandwidth and the signal-to-noise ratio of the received signal. The suitable value of ω_c is found at the frequency where the spectral component contributed by the received signal is indistinguishable from the spectral component contributed by the receiver noise. Having a lower value of ω_c makes the measured impulse response less noisy, but compromises the information content and the accuracy of the impulse response.

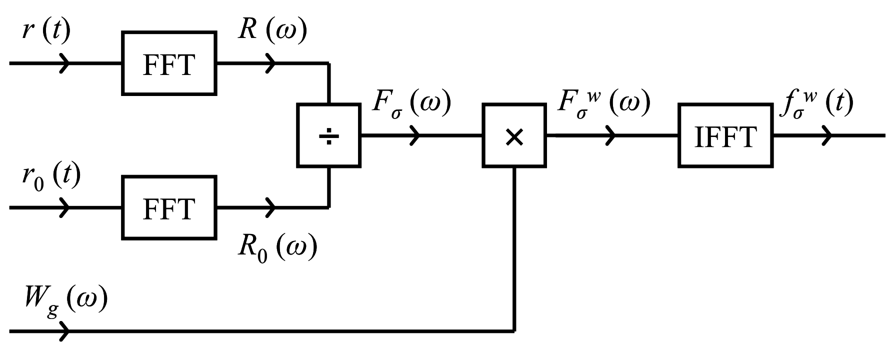

Figure 6.3: Signal processing blocks implemented in ADS Ptolemy [73] simulation to compute impulse response of target.

Equation (6.7) is implemented in the ADS Ptolemy [73] simulation. The schematic of the simulation is as shown in Figure 6.3. ADS Ptolemy is used as simulation tool because the measured signal from the oscilloscope can be fed directly to the computer, enabling fast calculation of the human body impulse response. In the measurement, sampling oscilloscope is used to obtain high resolution in the measured waveform. Furthermore, waveform averaging is performed to increase the SNR of the received signal. Hence, we have to ensure that the human body target is stationary during the period of measurement.

6.3 Modeling of the Human Body Impulse Response

In this Section, we will derive the theoretical human body impulse response, $f_{\sigma}^{w}(t)$, to verify the measured impulse response (6.7) in Section 6.2. It is known that the human body impulse response models the electromagnetic interaction between the incident signal, the human body shape and the dielectric properties. To reduce the complexity of derivation, we assume that the transmited UWB signal is incident to the human body at right angles. Furthermore, we assume that the UWB signal incident to the human body is a plane wave, and the area of human body under probing is relatively flat. In the measurement, we position the human body or human phantom at boresight direction, and in far-field region of the UWB radar, so that the UWB signal is incident perpendicularly to the human body as a plane wave. Furthermore, the area of interest in the human body is the torso region, which is relatively flat in shape.

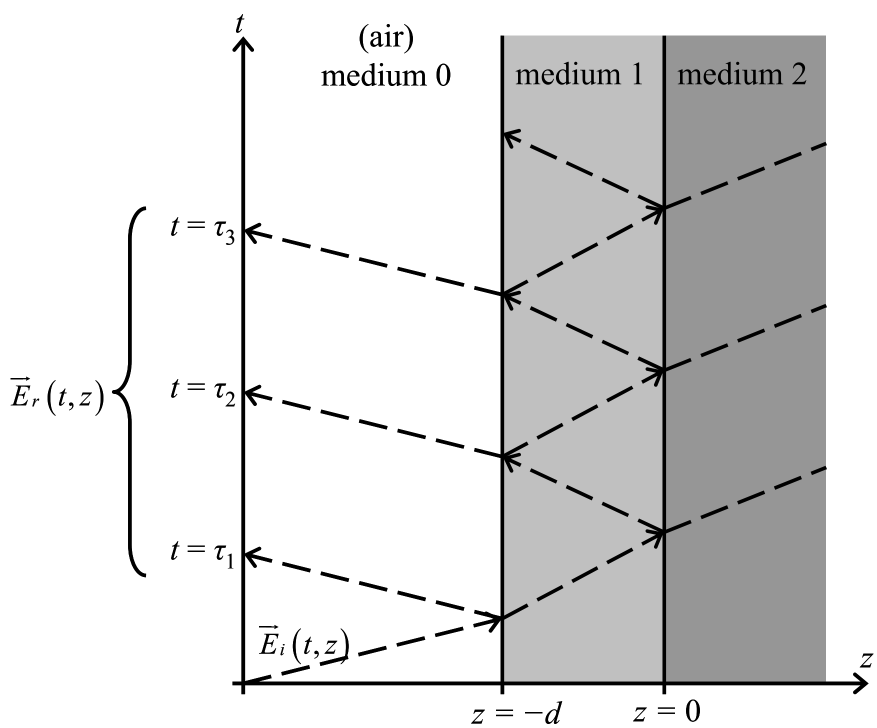

Figure 6.4: Reflection diagram of a target consisting of a two layer medium.

Figure 6.4 shows the reflection diagram of a human body target consisting of a two-layered medium. Let the outer layer be called 'medium 1' and the inner layer, 'medium 2'. For this experiment, because both mediums 1 and 2 are highly lossy human tissues, any reflections beyond the inner layer are assumed to have negligible contribution to the scattered signal. The *z*–axis in Figure 6.4 denotes distance. Let the transition between medium 1 and 2 be at $z = 0$. The thickness of medium 1 is d. The *t*–axis of Figure 6.4 denotes time. The radiated UWB signal, E_i, is incident on the target at right angles. When the signal reaches the transition between air and medium 1, some of the signal energy is reflected back to the UWB radar, reaching the UWB radar at $t = \tau_1$. The rest of the signal energy penetrates medium 1 to reach the transition between mediums 1 and 2. Because medium 1 is lossy, signal energy gets attenuated as it propagates through the layer. At the transition between mediums 1 and 2, some of the signal is reflected back to the transition between air and medium 1, and some of the reflected signal penetrate the said transition and propagate back to the UWB radar. This second reflection signal reaches the UWB radar at $t = \tau_2$. Signal components that penetrate medium 2 are ignored because we believe that the reflections resulting from this signal is too small to be detectable by the UWB radar. Multiple reflections occur within medium 1, and the reflected signals reach the UWB radar at times $t = \tau_3, \tau_4 \ldots$

Let η_i denote the characteristic impedance of the layers; ε_{ri} denote the relative permittivity of the layers; $\tan \delta_i$ denote the loss tangent of the layers; and k_i denote the propagation constant within the layers. Let the subscript i indicates the layers of the medium , where i = 0, 1, 2 represents the characteristics for air (medium 0), medium 1 and medium 2 respectively. It can be shown that

$$\eta_i(\omega) = \eta_0 \Big/ \sqrt{\varepsilon_{ri}(\omega) \cdot \left[1 - j \tan \delta_i(\omega)\right]} \tag{6.9}$$

$$k_i(\omega) = k_0 \sqrt{\varepsilon_{ri}(\omega) \cdot \left[1 - j \tan \delta_i(\omega)\right]} \tag{6.10}$$

where η_0 and k_0 are the intrinsic impedance and propagation constant of free-space or air (medium 0).

$$\eta_0 = \sqrt{\mu_0/\varepsilon_0} \tag{6.11}$$

$$k_0 = \omega\sqrt{\mu_0\varepsilon_0} \tag{6.12}$$

μ_0 and ε_0 are free-space permeability and permittivity constants. Using the transmission-line analogy of wave propagation and the impedance concept [74], the reflections can be modeled as impedance mismatches at different lengths of ideal transmission lines, as shown in Figure 6.5.

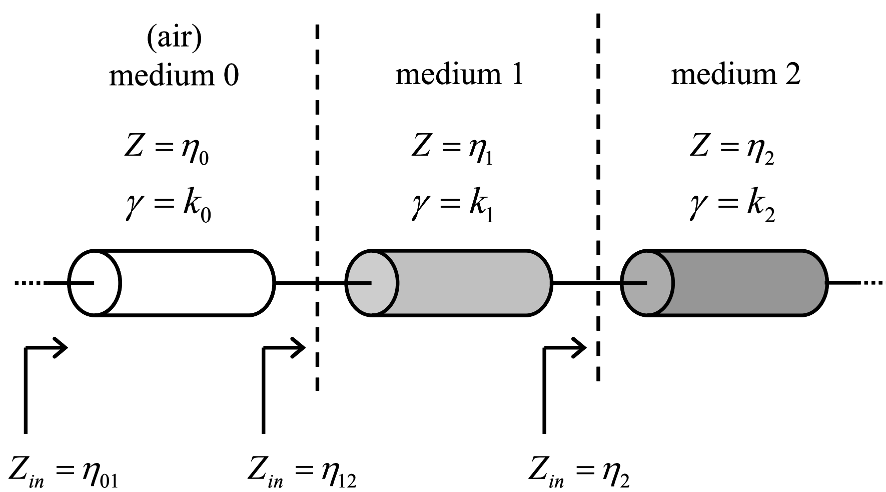

Figure 6.5: Transmission-line analogy of the wave propagation model in Figure 6.4.

Applying transmission-line theory, the input impedance at the transition between mediums 1 and 2 is η_2 because we have assumed that medium 2 is infinitely thick (no more reflections from medium 2). Hence, the input impedance at the transition between air and medium 1 is

$$\eta_{12} = \eta_1 \frac{\eta_2 + \eta_1 \tanh\left(k_1 d_{m1}\right)}{\eta_1 + \eta_2 \tanh\left(k_1 d_{m1}\right)} \tag{6.13}$$

Furthermore, the input impedance at a distance d_{m0} from the surface of medium 1 can be written as

$$\eta_{01} = \eta_0 \frac{\eta_{12} + \eta_0 \tanh\left(k_0 d_{m0}\right)}{\eta_0 + \eta_{12} \tanh\left(k_0 d_{m0}\right)} \tag{6.14}$$

The impulse response of the human body can be derived by converting η_{01} into reflection coefficient, namely,

$$f_\sigma^{th}\left(t\right) = \Im^{-1}\left[\left(\eta_{01} - \eta_0\right)/\left(\eta_{01} + \eta_0\right)\right] \tag{6.15}$$

6.4 Construction of Human Phantom and UWB Radar

As mentioned in the previous section, a possible location for probing by the UWB radar is the torso region of the human body. For illustration, the heart and stomach cross-sections of the human torso are shown in Figures 6.6 and 6.7 respectively. The cross-sections in Figures 6.6 and 6.7 show that the human torso consists of tissues like blood, bodily fluids, bone, breast fat, cartilage, fat, heart, lung, muscle, skin, stomach, spinal cord *etc*.

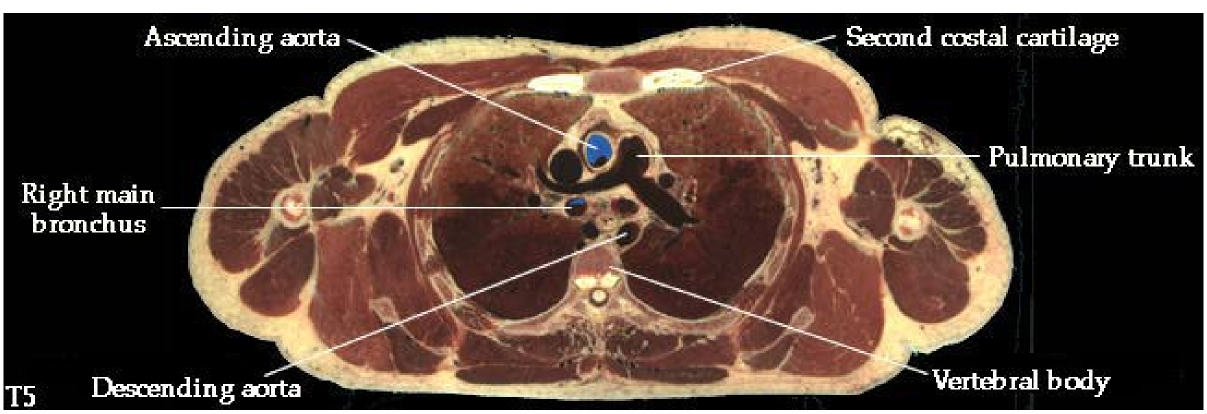

Figure 6.6: Heart cross-section of the human torso [76].

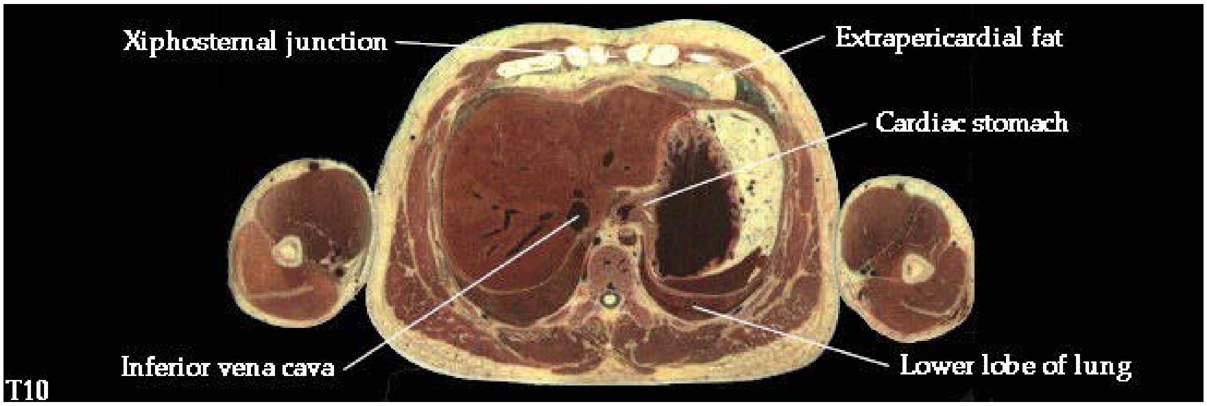

Figure 6.7: Stomach cross-section of the human torso [76].

Fortunately, the dielectric properties of these tissues have been compiled and measured by [64], and are available in open literature [75] for frequency range from 10 Hz to 100 GHz. To construct an approximate human body phantom with the correct dielectric values, we make use of available liquids. By measuring their dielectric values and then compare with the dielectric properties of the tissues, the suitability of the liquids in representing the human tissues can be judged. There are many criteria involved in selecting a suitable human phantom material. Besides malleability and closeness to human tissues in dielectric values, more mundane factors like cost, “availability, toxicity and stability” [50] need to be considered too. In the literature, many materials have been used as human tissue phantoms. In [50], soybean oil was used as breast fat simulant, an unclad FR4 glass epoxy printed circuit board as the skin layer, and water-diacetin mixure as tumor simulant. In [60], water was used as heart phantom; GSM900 brain tissue simulant [78] as lung phantom; and vegetable oil as fat phantom. Methanol and ethanol are also considered for breast tissue simulant in [79].

In this chapter, we use palm oil (cooking oil), tap water, saturated aqueous fine white sugar solution, GSM1800 brain tissue simulant [78] as tissue phantoms. The dielectric constants are measured from 200 MHz to 20 GHz using Agilent 85070D Dielectric Probe. However, for clearer presentation, only values at 6 GHz (the centre frequency of radar operation) of the phantoms and the relevant tissues are shown in Figure 6.8.

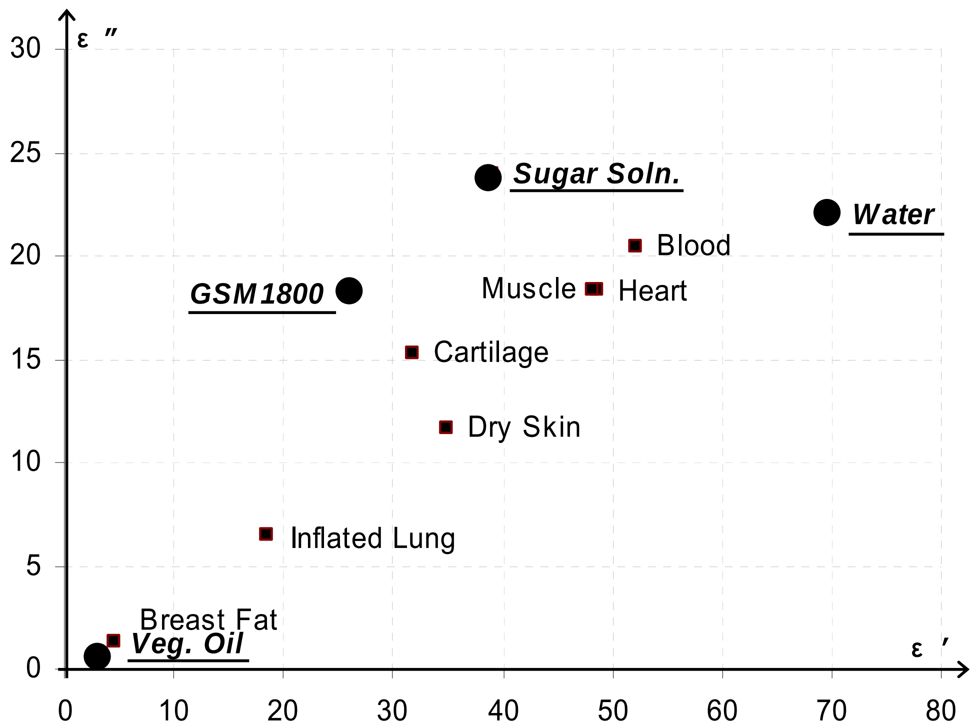

Figure 6.8: Dielectric values, at 6 GHz, of measurement phantom (underlined) are comparable to that of selected human body tissues.

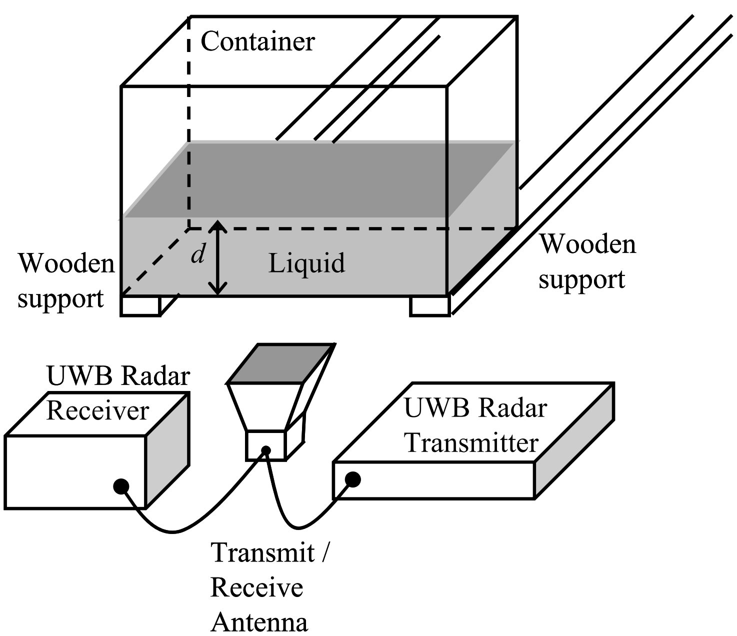

Figure 6.9: Human body phantom construction, positioning and measurement.

An approximate human phantom is constructed with a cube-shaped polythene container (dimensions: 45 cm × 30 cm × 28 cm) filled partially with the liquid phantom to simulate a layer of the tissue. The thickness of the container wall is thin (< 2 mm), and the dielectric constant of polythene is low (ε_r = 2.25; tan δ = 5.8 x 10^{-4} at 3 GHz) [80]. The thickness of the phantom layer can be controlled by the depth of the liquid. The container is suspended in air with two wood supports at the sides, as shown in Figure 6.9. The UWB Radar is placed below the container, with the transmitting / receiving antenna located below the container, pointing upwards.

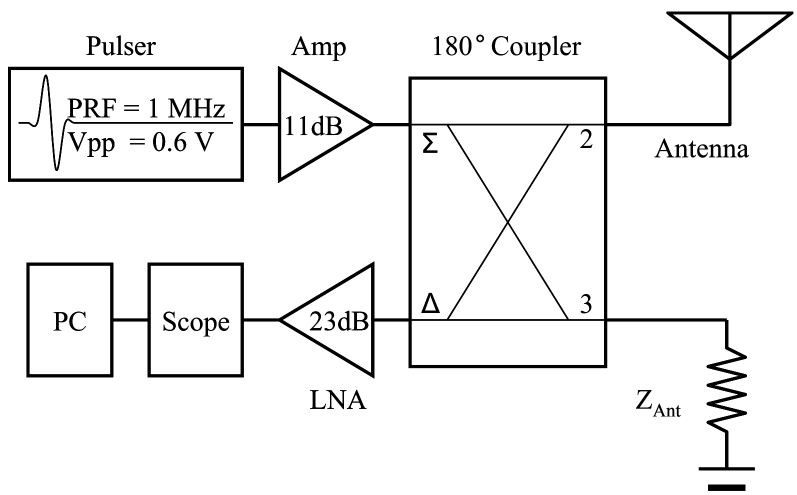

Figure 6.10: Schematic diagram of the UWB radar.

The UWB radar is constructed with component modules that are available commercially. Figure 6.10 shows the schematic diagram of the UWB radar. As mentioned in Section 6.2, the UWB radar uses the same transmitting and receiving antenna. The source signal is a pulser that generates 200 ps, 0.6 V pulses at pulse repetition frequency (PRF) of 1 MHz. The pulser output is then amplified at 11 dB. A 180° hybrid coupler is used as a duplexer between the transmitter chain and the receiver chain. The four ports of the 180° hybrid coupler are labeled as port-Σ, port-Δ, port-2 and port-3. The source signal from the transmitter chain is connected to port-Σ. The antenna is connected to port-2, while an equivalent antenna-load is to port-3 to suppress the signal reflections due to input impedance mismatch of the antenna. Port-Δ is connected to the receiver chain, which consists of a 23 dB LNA connected to an oscilloscope. The received signal is recorded by the oscilloscope. By connecting the oscilloscope with a personal computer that is running ADS Ptolemy [62], the recorded signal is transferred directly to the simulation. The simulation performs the function in Figure 6.3, and outputs the human body impulse response within seconds of the measurement.

The UWB signal emitted by the antenna has a pulse width of 230 ps, and is shown in Figure 6.11. In frequency domain, the signal spectrum is centered at 6 GHz and has a bandwidth of 8 GHz (2-10 GHz), as shown in Figure 6.12.

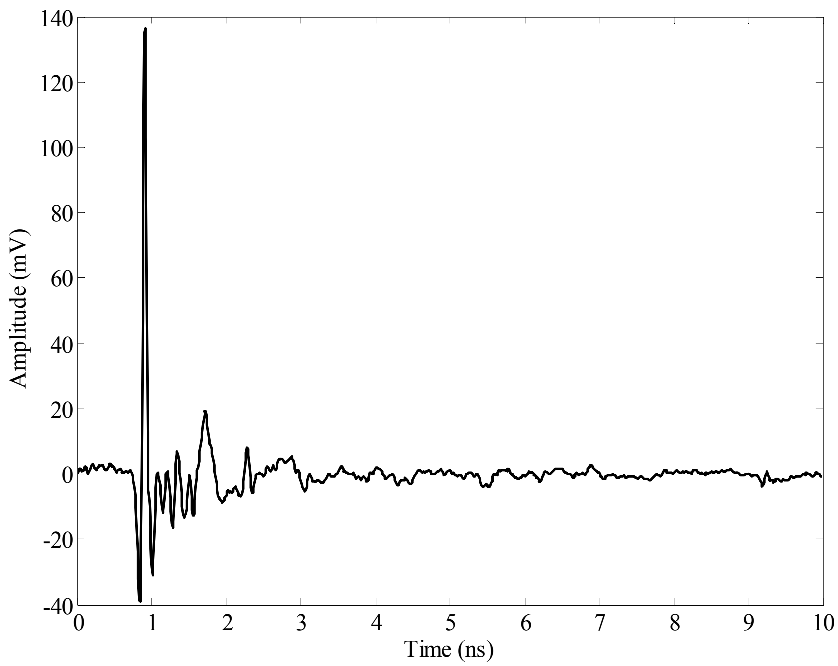

Figure 6.11: Transmitted UWB signal, measured with a ridged-horn antenna at far-field.

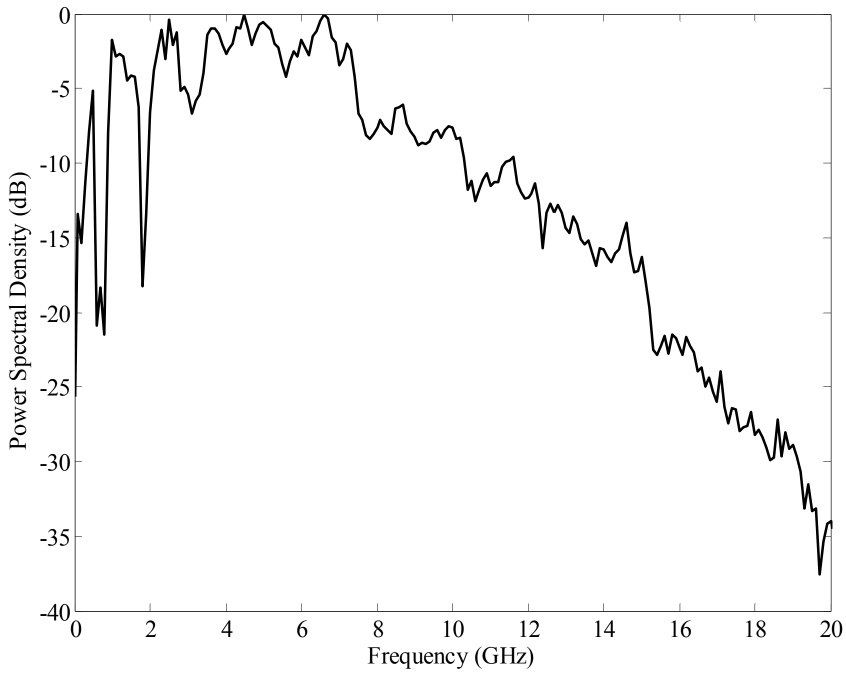

Figure 6.12: Power spectral density (normalized) of transmitted UWB signal.

6.5 Measured Result

Experiments were conducted with the measurement setup shown in Figure 6.9 using the UWB radar shown in 6.10. In these experiments, scattered signals from the human phantom are measured, and the measured signals are processed with the simulation procedure shown in Figure 6.3 to calculate the measured impulse responses. Then, the measured impulse responses are verified with theoretical impulse responses that are calculated based on the dielectric properties of the human phantom liquids and thickness of the liquid layers.

One interesting point of discussion is the effect of windowing function, $W_g(\omega)$, on the shape of the impulse response. The purpose of the windowing function is to filter out the noise component of the impulse response. If the window is defined with too wide a bandwidth (ω_c), it will admit more noise components, which causes the impulse response to be corrupted by the noise. On the other hand, if the window is defined with too narrow a bandwidth, it will attenuate the higher frequencies of the impulse response, causing the impulse response to be more dispersed, thus compromising the ability of the impulse response in determining the characteristics of the target. The above mentioned effect is shown in Fig. 6.13, where the measured signal of a 10 mm palm oil human phantom is plotted with its calculated impulse responses. The impulse responses are windowed with the windowing function, $W_g(\omega)$, with ω_c = 2π(20 GHz), 2π(15 GHz), 2π(10 GHz), 2π(7.5 GHz) and 2π(5 GHz). The impulse responses in Fig. 6.13 shows that at higher values of ω_c, the impulse response is noisy, *i.e.* ω_c = 2π(20 GHz), while at lower values of ω_c, the impulse response is highly dispersed, *i.e.* ω_c = 2π(5 GHz). Thus, for the rest of the measured impulse responses, ω_c = 2π(15 GHz) will be chosen, since at this value, we achieve a good compromise between noise level and signal dispersion.

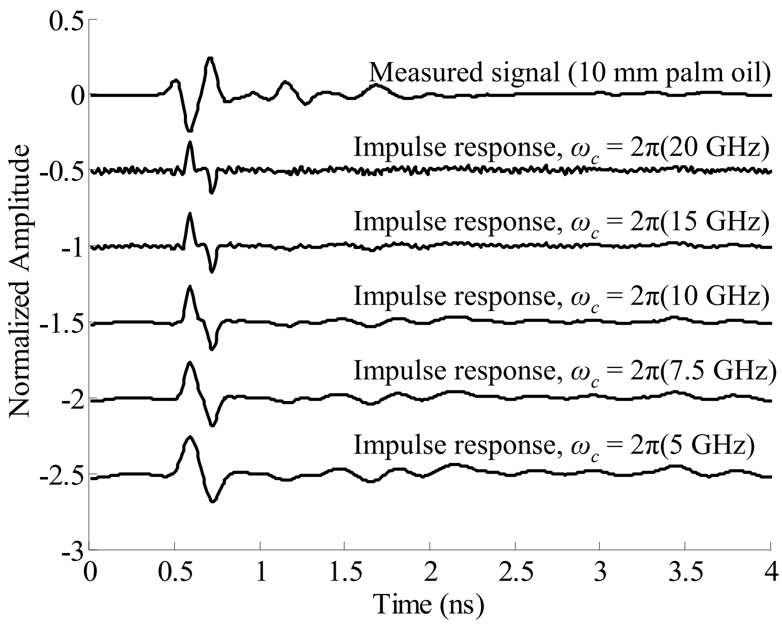

Figure 6.13: Measured signal of 10 mm palm oil human phantom, and the impulse responses with different values of ω_c.

Figures 6.14 to 6.17 show the measured received signals and impulse responses of the human phantom liquids for palm oil (Figure 6.13), GSM-1800 brain tissue stimulant (Figure 6.14), saturated sugar solution (Figure 6.15) and tap water (Figure 6.16).

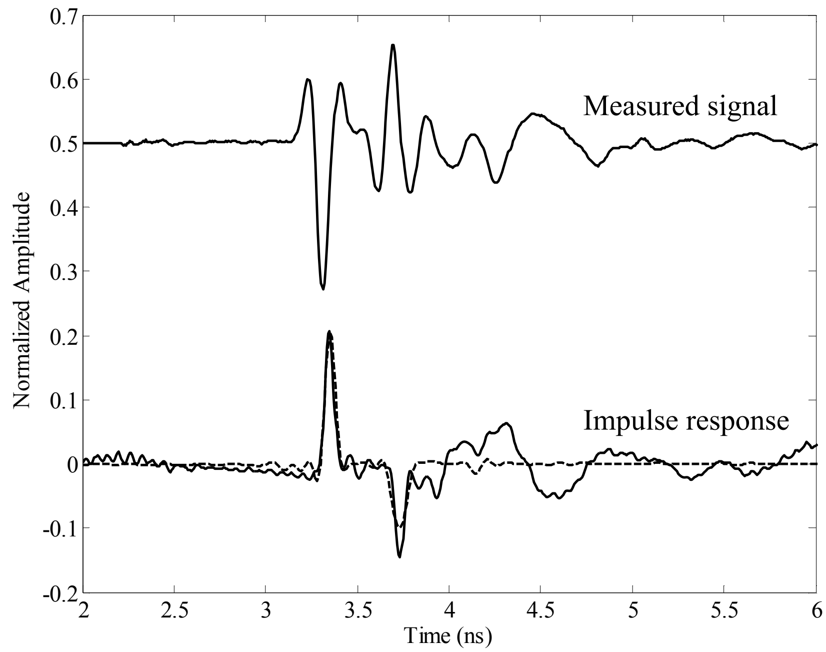

Figure 6.14: Measured signal (line), measured impulse response (line) and theoretical impulse response (dashed line) of 32 mm palm oil (cooking oil).

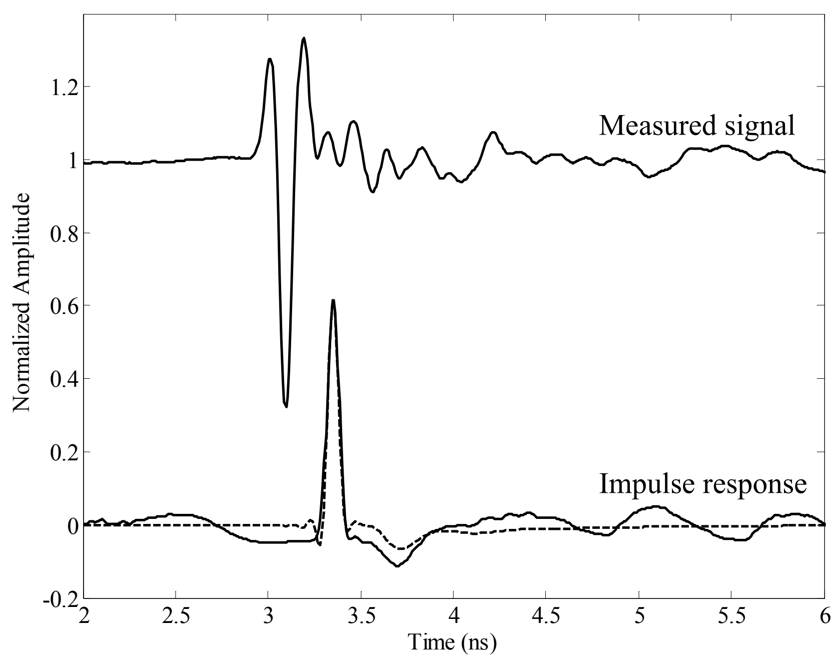

Figure 6.15: Measured signal (line), measured impulse response (line) and theoretical impulse response (dashed line) of 9 mm GSM 1800 brain tissue simulant.

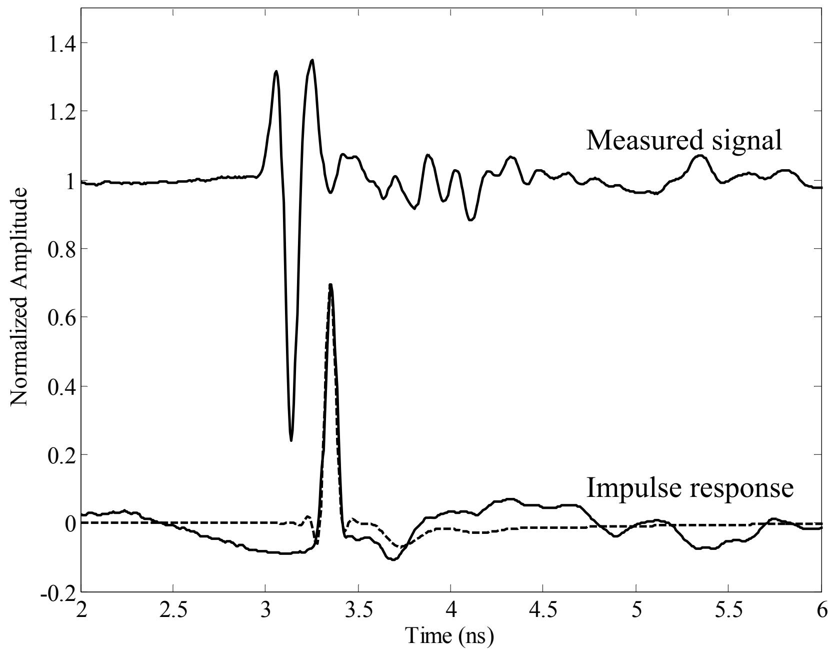

Figure 6.16: Measured signal (line), measured impulse response (line) and theoretical impulse response (dashed line) of 8 mm saturated sugar solution.

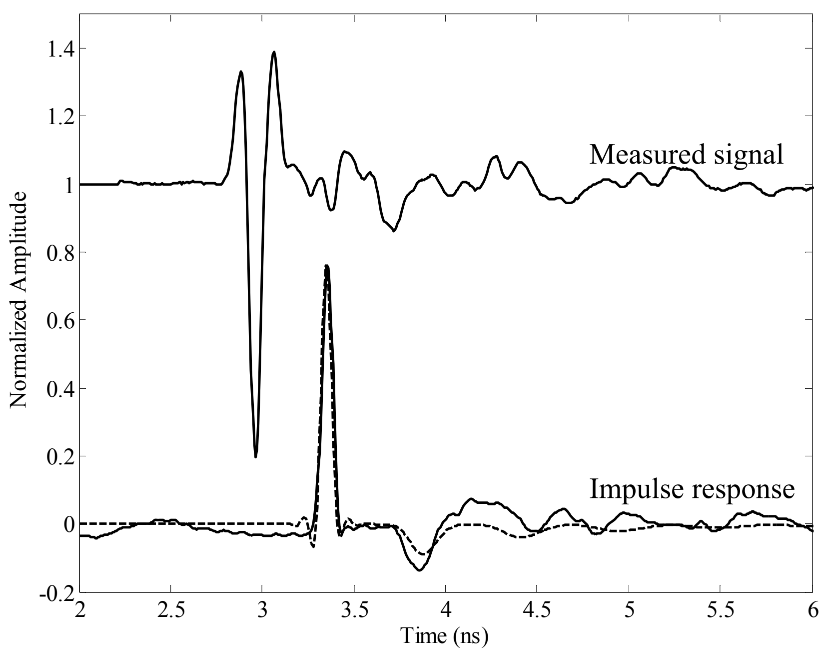

Figure 6.17: Measured signal (line), measured impulse response (line) and theoretical impulse response (dashed line) of 9 mm tap water.

By observing the measured received signals in Figures 6.14 to 6.17 alone, it is difficult to deduce the physical properties of the human phantoms. The difficulty arises because there is significant ringing in the received signals that are not caused by the second and subsequent reflections of the human phantom. For all the human phantoms, only in palm oil can we observe the second reflection directly from the measured signal (Figure 6.14). On the other hand, the measured impulse responses of the human phantoms manage to reduce the UWB signal into Gaussian pulses with minimal ringing at the tail-end, as shown in the measured impulse response waveforms (line) in Figures 6.14 to 6.17. The high level of ringing that exists in the received UWB signal is minimized in the measured impulse response waveforms; hence the second reflection is now visible for all human phantoms. However, there are no observable reflected signals beyond the second reflection for the measured impulse response waveforms.

The dielectric properties of the liquid can be deduced from the first reflection. As shown in Figure 6.8, the human phantom liquids, arranged in ascending order of ε' value, are palm oil, GSM1800 solution, saturated sugar solution and tap water. A similar trend is also reflected in the amplitudes of the measured impulse responses. The amplitude values are also in ascending order from palm oil (amplitude = 0.2), GSM1800 solution (amplitude = 0.59), saturated sugar solution (amplitude = 0.68) and tap water (amplitude = 0.77). High ε' and ε'' values in all human phantom liquids, except the palm oil, result in very weak and dispersed second reflections, as shown in the measured impulse response. The theoretical impulse response waveforms (dashed lines) are superimposed onto the measured impulse response waveforms (lines) in Figures 6.14 to 6.17 for the four human phantom liquids. The position, amplitude and pulse shape of the theoretical impulse responses are similar to the measured impulse responses for all the four types of human phantoms.

6.6 Chapter Summary

A method for measuring human body impulse response with UWB radar is proposed. Furthermore, a monostatic UWB radar is designed and a liquid based human phantom is constructed. Using the UWB radar to measure the human phantom, the method is verified with measured impulse response.

CHAPTER 7

CONCLUSION

7.1 Conclusion

In this thesis, we researched on a number of issues regarding the modeling and design of ultra-wideband (UWB) components and systems. Firstly, in order to predict the pulse distortion of the UWB signals by antenna, we proposed that both transmitting and receiving antennas are modeled as impulse responses. Following from the work in [17]−[19], we derived the impulse response of the antenna from the antenna's aperture field distribution. To verify this derivation, we obtained a commercially available ridged-horn antenna, and defined the aperture field distribution function of this ridged-horn. From the ridged-horn's aperture field distribution function, we derived the impulse response the ridged-horn in both transmitting and receiving modes. The derived impulse responses were verified with measurements.

The impulse response of the antenna was then applied to an array of ridged-horn antennas used in the time-difference-of-arrival (TDOA) method to find the target's angle. The time-of-arrival accuracy of the individual receivers of the TDOA were derived while taking into account of the effect of signal distortion of the receiving antennas. From the derived time-of-arrival, we then derive the probability density function of the angle-of-arrival of the TDOA method. To verify the derivations, a TDOA receiver array is constructed, and the root-mean-square errors of the angle-of-arrival were measured for various angles. The measurements of root-mean-square error, conducted in three signal-to-noise ratio (SNR) conditions were shown to be similar to the derived angle-of-arrival accuracy, thus verifying the derivations.

Next, the impulse response of the antenna was applied to the UWB monopulse receiver consisting of a square-feed array of four ridged-horns. Furthermore, a monopulse receiver consisting of bank of cross-correlation circuits was proposed to convert the monopulse sum and difference signals into voltages. These voltages were used in an amplitude-comparison monopulse processor to calculate the monopulse ratio, which is a received signal independent ratio used to discriminate the angle-of-arrival of scattered signals. To verify the derivations, experiments were conducted to measure the monopulse sum and difference signals, and the monopulse ratio. The measurements were done with a prototype monopulse receiver comprising of two ridged-horn antennas placed on a turn-table. Furthermore, the angle-of-arrival accuracy based on monopulse receiver, were derived and verified with further measurements.

In a UWB transceiver, the source signal was generated by a class of circuit generally classified as pulse-forming networks (PFN). In the thesis, a pulse forming network (PFN) that is amenable to integrated circuit was designed, fabricated and measured. The PFN was designed based on a frequency-selective, negative-feedback circuit which uses only simple components like transistors, resistors and capacitors. Measured output pulses from the PFN showed that the circuit manages to produce pulses of consistent pulse widths (170 ps to 180 ps) for a large variation of input signal rise-times (45 ps to 300 ps), as intended by the design. By generating Manchester coded data at 500 Mbps, the effective isotropic radiation power (EIRP) of a transmitter, which uses the PFN, complied with the FCC EIRP limit without the need of an additional amplifier at the front-end. The power supply to the PFN is 3.3V, 20 mA during operations.

An interesting application of the UWB radar is in human body imaging. To perform human body imaging, we proposed a method of measurement using the impulse response to model the scattering of the UWB signal by the human body target. Finding the human body impulse response involves a series of measurements and some signal processing. To conduct the experiment, we constructed a human phantom, developed a monostatic UWB radar and developed the signal processing algorithm in ADS Ptolemy. The measured impulse response of human phantom showed that the measurement method is a good way of measuring the physical and dielectric characteristics of the human body.

7.2 Future Work

In Chapters 3 and 4, an array of antennas is used to determine the angle-of-arrival of an incident signal. A good complement to this work is the analysis of the mutual coupling between the antennas and its effect on the accuracy performance of the receivers. This analysis will extend our understanding of mutual coupling of antenna from frequency domain based narrowband signals to time domain based UWB signals. To achieve better resolution and tracking capability, more antennas will be needed in the UWB radio system. When this is the case, the effect of antenna mutual coupling can result in significant deterioration to the system performance. Thus, modeling of the mutual coupling becomes an important issue so that better array designs can be realized to minimize mutual coupling between the antennas.

In Chapter 3, we have identified the antenna noise as a major source of noise in the UWB receiver, and derived a system performance parameter – angle accuracy, based on the relative power levels of the antenna noise. This analysis, however, is an over idealization of the UWB receiver, because firstly, there are other active and passive components in the receiver chain, and secondly, a realistic cross-correlation receiver circuit cannot achieve perfect multiplication and integration of the received signal. In a narrowband receiver, signal deteriorations through the receiver components are modeled as return loss, insertion loss, noise figure, 1-dB compression point (P1dB), conversion loss *etc.* which fails to describe time-domain signal distortions that are of interest in UWB signals. Hence, a more generic model for the UWB receiver components is needed. Successful modeling of the components in the UWB receiver chain enables a better understanding of the UWB signal deterioration in the receiver, and a framework to design and optimize UWB receivers.

In a UWB radar transceiver, it is not possible to predict the pulse shape that is incident to the receiver, because the radar target scatters the incident signal in a manner that is based on the shape and its dielectric properties. Hence, a complete analysis of a UWB tracking receiver needs to consider this effect. A study could be made to modify the existing receivers or propose new receivers which could achieve a better tracking capability than the cross-correlation receiver which is proposed in this thesis. This analysis could possibly lead to a target-specific tracking radar which could possibly identify and track a specific target better in the midst of clutter.

In Chapter 6, the basis of a human body measurement method has been established. Theoretically, the measurement method is capable of measuring multiple layers of lossy dielectric medium (*i.e.* human tissues) and probing the human body's internal organs. Further improvements can be done to increase the complexity of the human phantom to be a more realistic approximation of the human body, to enhance the design of the UWB radar transceiver with the suggestions above, and to incorporate range and angular imaging capabilities in the radar.

BIBLIOGRAPHY

[1] J. D. Taylor, Ed., *Introduction to Ultra-wideband Radar System*, CRC Press, 1995.

[2] *First Report and Order Regarding the Revision of Part 15 of the Commission's Rules Regarding Ultra-Wideband Transmission Systems*, Federal Communications Commission, ET Docket 98-153, Apr. 2002.

[3] J. W. McCorkle and J. E. Thompson, "System and Method for Generating Ultra Wideband Pulses", *PCT Patent No. WO 02/31986A2*, Apr. 2002.

[4] Wisair, "The DV9100 UWB Development Kit, Wisair Multi Band OFDM Development Platform", 2004.

[5] R. J. Fontana, "Recent System Applications of Short-Pulse Ultra-Wideband (UWB) Technology", *IEEE Trans. MTT*, vol. 52, no. 9, pp. 2087-2104, Sep 2004.

[6] A. Batra *et. al*. "Multi-band OFDM physical layer proposal for IEEE 802.15 task group 3a," IEEE 802.15-04/0493r1, Sept. 2004.

[7] M. B. Shoemake, "Multi-band OFDM update and overview," IEEE 802.15-04/0518, Sept. 2004.

[8] R. Fisher *et. al*., "DS-UWB physical layer submission to 802.15 task group 3a," IEEE 802.15-04/137r3, May 2004.

[9] R. Fisher *et. al*., "DS-UWB proposal update," IEEE 802.15-04/140r3, May 2004.

[10] P. M. Woodward, *Probability and Information Theory, with Applications to Radar*, Massachusetts: Artech House, 1980.

[11] P. R. Foster, "Antennas and UWB Signals", *Introduction to Ultra-Wideband Radar Systems*, edited by J. D. Taylor, CRC, New York, 1994, pp.147-216.

[12] S. N. Samaddar and E. L. Mokole, "Some Properties of Antennas as Associated with Ultra-wideband Radiation", *Ultra-Wideband, Short-Pulse Electromagnetics 3*, Kluwer, New York, 1998, pp. 147-164.

[13] G. P. Pochanin, "Large Current Radiator for the Short Electromagnetic Pulses Radiation", Ultra-Wideband, *Short-Pulse Electromagnetics 4, Kluwer*, New York, 1999, pp. 149-155.

[14] C. A. Balanis, *Antenna Theory Analysis and Design*, 2nd ed., John Wiley, New York, 1997.

[15] G. S. Smith, "Teaching antenna radiation from a time-domain perspective," *Am. J. Phys.*, vol. 69, pp. 829-844, 2001.

[16] S. P. Skulkin, “Transient Fields of Rectangular Aperture Antennas”, *Ultra-Wideband, Short-Pulse Electromagnetics 3*, Kluwer, New York, 1998, pp. 57-63.

[17] H. D. Griffiths and A. L. Cullen, “Sidelobe Response of Antennas to Short Pulse Signals”, *IEEE Radar Conference*, 2003, pp. 85-90.

[18] H. D. Griffiths and A. L. Cullen, “Sidelobe response of antennas to short pulses part I: Theory”, *IEE Proc. Microwaves, Antennas and Propagation*, vol. 149, no. 4, pp. 189-193, Aug. 2002.

[19] R. Benjamin, “The sidelobe response of antennas to short pulses part II: Manifestations and applications”, *IEE Proc. Microwaves, Antennas and Propagation*, vol. 149, no. 4, pp. 194-199 Aug. 2002.

[20] H. G. Schantz, “Dispersion and UWB Antennas”, *2004 Joint UWBST & IWUWBS*, 18-24 May 2004.

[21] M. Kanda, “Time-Domain Sensors and Radiators”, *Time-Domain Measurements in Electromagnetics*, edited by E. K. Miller, Van Nostrand Reinhold, New York, 1986, pp. 122-174.

[22] J. R. Andrews, “UWB Signal Sources, Antennas and Propagation”, *Picosecond Pulse Labs Application Note* AN-14a, Aug. 2003.

[23] K. Rambabu, A. E.-C. Tan, K. K.-M. Chan and M. Y.-W. Chia, “Does Antenna Gain Affect UWB Pulse Shape in Transmission and Reception?” submitted to *IEEE Trans. AP*, Mar. 2007.

[24] R. J. Fontana and S. J. Gunderson, “Ultra-wideband precision asset location system”, *2002 Conference on Ultra Wideband Systems and Technologies*.

[25] K. Yu and I. Oppermann, “Performance of UWB positioning estimation based on time-of-arrival measurements”, *IWUWBS 2004*, 18-21 May 2004.

[26] R. J.-M. Cramer, R. A. Scholtz and M. Z. Win, “Evaluation of Ultra-Wide-Band Propagation Channel”, *IEEE Trans. AP*, vol. 50, no. 5, May 2002.

[27] L. Stoica, A. Rabbachin and I. Oppermann, “A low-complexity noncoherent IR-UWB transceiver architecture with TOA estimation”, *IEEE Trans. MTT*, vol. 54, no. 4, April 2006, pp. 1637-1646.

[28] C. Zhang, M. Kuhn, B. Merkl, A. E. Fathy and M. Mahfouz, “Accurate UWB Indoor Localization System Utilizing Time Difference of Arrival Approach”, *2006 IEEE Radio and Wireless Symposium*, 17-19 Jan. 2006, pp. 515-518.

[29] IEEE Standard 686-2007, *Radar Definitions*, Institute of Electrical and Electronics Engineers, 2007.

[30] M.I. Skolnik (Ed.), *Radar Handbook*, McGraw-Hill, 1970, Chapter 21.

[31] A. I. Leonov, “History of Monopulse Radar in the USSR”, *IEEE AES Systems Mag*., May 1998, pp. 7-13.

[32] H. F. Harmuth, “Antennas for Nonsinusoidal Waves: Part: III – Arrays”, *IEEE Trans. EMC*, vol. EMC-25, no. 3, Aug. 1983, pp. 346-357.

[33] M. G. M. Hussain, “Line-Array Beam-Forming and Monopulse Techniques Based on Slope Patterns of Nonsinusoidal Waveforms”, *IEEE Trans. EMC*, vol. EMC-29, no. 3, Aug. 1985, pp. 143-151.

[34] M. G. M. Hussain, “A Self-Steering Arrays for Nonsinusoidal Waves Based on Array Impulse Response Measurement”, *IEEE Trans. EMC.*, vol. 30, no. 2, May 1988, pp. 154-160.

[35] M. G. M. Hussain, “Performance Analysis and Advancement of Self-Steering Arrays for Nonsinusoidal Waves – I & II”, *IEEE Trans. EMC.*, vol. 30, no. 2, May 1988, pp. 161-174.

[36] M. G. M. Hussain, “Principles of Space-Time Array Processing for Ultrawide-Band Impulse Radar and Radio Communications”, *IEEE Trans. Veh. Tech.*, vol. 51, no. 3, May 2002, pp. 393-403.

[37] T. E. McEwan, G. E. Dallum, “Soliton Quenching NLTL Impulse Circuit with a Pulse Forming Network at the Output”, *US Patent* 5,804,921, Sep. 1998.

[38] J. A. Andrews, “Picosecond Pulse Generators for UWB Radars”, *Picosecond Pulse Labs Application Note* AN-9, May 2000.

[39] J. S. Lee, N. Nguyen, and T. Scullion, “New Unipolar Subnanosecond Monocycle Pulse Generator and Transformer for Time-Domain Microwave Applications”, *IEEE Trans. MTT*, vol. 49, no. 6, pp. 1126-1129, June 2001.

[40] J. Han, C. Nguyen, “A New Ultra-Wideband, Ultra-Short Monocycle Pulse Generator with Reduced Ringing”, *IEEE Microwave and Wireless Components Letters*, vol. 12, no. 6, pp. 206-208, Jun. 2002.

[41] J. A. Andrews, “Fast-Pulse Generator Survey”, *Time-Domain Measurements in Electro-magnetics*, edited by E. K. Miller, Van Nostrand Reinhold, New York, 1986, pp. 122-174.

[42] Yeap, W. Y., “Ultra Wideband Signal Generation”, *Microwave Journal*, Sep. 2005, pp. 172.

[43] J. W. McCorkle and J. E. Thompson, “System and Method for Generating Ultra Wideband Pulses”, *PCT Patent No. WO 02/31986A2*, Apr. 2002.

[44] D. D. Wentzloff and A. P. Chandrakasan, “Gaussian Pulse Generators for Subbanded Ultra-Wideband Transmitters”, *IEEE Trans. MTT*, vol. 54, no. 4, April 2006.

[45] S. Bagga, A. V. Vorobyov, S. A. P. Haddad, A. G. Yarovoy and W. A. Serdijn, J. R. Long, “Codesign of an Impulse Generator and Miniaturized Antennas for IR-UWB”, *IEEE Trans. MTT*, vol. 54, no. 4, April 2006.

[46] M.I. Skolnik (Ed.), *Radar Handbook*, McGraw-Hill, 1970.

[47] E. M. Staderini, “UWB Radars in Medicine”, *IEEE AESS Systems Mag.*, vol. 17, pp. 13-18, Jan 2002.

[48] P. M. Meaney, K. D. Paulsen, and J. T. Chang, “Near-Field Microwave Imaging of Biologically-Based Materials Using a Monopole Transceiver System.” *IEEE Trans. MTT*, vol. 46, no. 1, pp. 31-45, Jan. 1998.

[49] E. C. Fear, P. M. Meaney and M. A. Stuchly, “Microwaves for breast cancer detection?” *IEEE Potentials* 2003.

[50] E. J. Bond, X. Li, S. C. Hagness and B. D. V. Veen, “Microwave Imaging via Space-Time Beamforming: Experimental Investigation of Tumor Detection in Multilayer Breast Phantoms”, *IEEE Trans. MTT*, vol. 52, no. 8, pp. 1856-1865, Aug. 2004.

[51] T. E. McEwan, “Body Monitoring and Imaging Apparatus and Method”, *US Patent* 5,766,208, Jun. 1998.

[52] M. Y. W. Chia, S. W. Leong, C. K. Sim, and K. M. Chan, “Through-wall UWB radar operating within FCC’s mask for sensing heart beat and breathing rate,” *35th Eur. Microw. Conf.*, Oct. 2005, pp. 1991–1994.

[53] C. Brass, “Terahertz imaging comes into focus”, *The Futures Foundation*, May 2007.

[54] “Terahertz imaging may reduce breast cancer surgeries”, *Medical News Today*, Apr. 2006.

[55] K. Rambabu, A. E.-C. Tan, K. K.-M. Chan and M. Y.-W. Chia, “Estimation of Antenna Effect on UWB Pulse Shape in Transmission and Reception”, submitted to *IEEE Trans. MTT*, Nov. 2006.

[56] K. Rambabu, A. E.-C. Tan, K. K.-M. Chan and M. Y.-W. Chia and S.-W. Leong, “Study of Antenna Effect on UWB Pulse Shape in Transmission and Reception”, *ISAP 2006*, Singapore, Nov. 2006.

[57] A. E.-C. Tan, M. Y.-W. Chia and K. Rambabu, “Effect of Antenna Noise on Angle Estimation in Ultra-Wideband Receivers”, submitted to *IEEE Trans. AP*, Dec. 2006.

[58] A. E.-C. Tan, M. Y.-W. Chia and K. Rambabu, “Design of Ultra-Wideband Monopulse Receiver”, *IEEE Trans. MTT*, vol. 54, no. 11, Nov. 2006, pp. 3821-3827.

[59] A. E.-C. Tan, M. Y.-W. Chia and S.-W. Leong, “Sub-nanosecond Pulse-Forming Network on SiGe BiCMOS for UWB Communications”, *IEEE Trans. MTT*, vol. 54, no. 3, Mar. 2006, pp. 1019-1024.

[60] A. E.-C. Tan and M. Y.-W. Chia, “Measuring Human Body Impulse Response Using UWB Radar”, *IEE Electron. Lett.*, vol. 41, no. 21, Oct. 2005, pp. 1193-1194.

[61] A. E.-C. Tan, and M. Y.-W. Chia, “Method of Generating UWB Pulses”, *World Intellectual Property Organization*, Pub. No. WO 2005/067160 A1, Jul. 2005.

[62] A. E.-C. Tan, and M. Y.-W. Chia, "UWB Radar Transceiver and Measurement for Medical Imaging", *IEEE BioCAS*, Singapore, Dec. 2004.

[63] A. E.-C. Tan and M. Y.-W. Chia, "Measuring Human Body's Impulse Response", *UK-Singapore Bioelectronics Workshop*, Jan 2006.

[64] K. L. Walton and V. C. Sundberg, "Broadband Ridged Horn Design", *Microwave Journal*, March. 1964, pp. 96-101.

[65] S. B. Cohn, "Properties of Ridge Wave Guide", *Proc. IRE*, vol. 35, Aug. 1947, pp. 783-788.

[66] H. J. Blinchikoff and A. I. Zverev, *Filtering in the Time and Frequency Domains*, Krieger Publishing Co., Florida, 1987, pp. 17-18.

[67] I. Guvenc, Z. Sahinoglu and P. V. Orlik, "TOA estimation for IR-UWB Systems with different transceiver types", *IEEE Trans. MTT*, vol. 54, no. 4, April 2006, pp. 1876-1886.

[68] A. C. Johnson and N. T. Thomopoulos, "Characteristics and tables of the doubly-truncated normal distribution", *Proc. POM High Tech*, 2002, pp. 18.

[69] J. G. Proakis, *Digital Communications 4th Ed.*, Singapore: McGraw-Hill, 2001, chap. 2, pp. 27-30.

[70] Sherman S. M., *Monopulse Principles and Techniques*, Artech House, 1984.

[71] Sedra and Smith, *Microelectronic Circuits 4th Ed.*, Oxford University Press, 1998.

[72] E. K. Miller, Ed., *Time-Domain Measurements in Electromagnetics*, Van Nostrand Reinhold, 1986, ch. 3.

[73] *Advanced System Technologies*, ADS Ptolemy simulation, Dec. 2002.

[74] Simon, R., Whinnery, J. R. and van Duzer, T., *Fields and Waves in Communication Electronics*, John Wiley, 3rd ed., 1994, ch. 6.

[75] C. Gabriel, S. Gabriel, E. Corthout, "The Dielectric Properties of Biological Tissues, Parts I – III", Phys. Med. Biol., vol. 41, pp. 2231-2293, 1996.

[76] Institute for Applied Physics, Italian National Research Council, "Dielectric Properties of Body Tissues": http://niremf.ifac.cnr.it/tissprop/

[77] United States National Library of Medicine, The Visible Human Project: http://www.nlm.nih.gov/research/visible/visible_human.html

[78] DASY4 Dosimetric Assessment System Manual, Schmid and Partner Engineering AG, March 2003.

[79] D. M. Hagl et. al. “Sensing Volume of Open-Ended Coaxial Probes for Dielectric Characterization of Breast Tissue at Microwave Frequencies”, IEEE Trans. MTT. vol. 51, no. 4, pp. 1194-1206, Apr. 2003.

[80] A. R. v. Hippel, *Dielectric Material and Applications*, MIT Press, 1954, appendix V.